AD

NDL-TR-54

NEUTRON DETECTION AND SPECTROSCOPY
WITH SEMICONDUCTOR DETECTORS

M. R. Zatzick

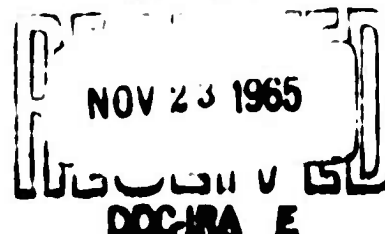E. L. Zimmerman

SOLID STATE RADIATIONS, Inc

NOVEMBER 1965

Code 1

DDC

NOV 23 1965

PREPARED FOR

DDC-IRA E

US ARMY
NUCLEAR DEFENSE LABORATORY
EDGEWOOD ARSENAL, MARYLAND

DDC Availability Notice

Qualified requesters may obtain copies of this report from the Defense Documentation Center (DDC), Cameron Station, Alexandria, Virginia 22314.

Disposition Instructions

Destroy this report when it is no longer needed. Do not return it to the originator.

Disclaimer

The findings in this report are not to be construed as an official Department of the Army position, unless so designated by other authorized documents.

BLANK PAGE

NDL-TR-54

NEUTRON DETECTION AND SPECTROSCOPY WITH SEMICONDUCTOR DETECTORS

Revised April 1965

by

M. R. Zatzick
E. L. Zimmerman

Contract DA18-108-405-Cml-1012

Prepared by

Solid State Radiations, Inc.

for

US ARMY
NUCLEAR DEFENSE LABORATORY
Edgewood Arsenal, Maryland

ABSTRACT

Results are presented of a study of methods for utilizing diffused junction, semiconductor detectors in neutron detection and spectroscopy. The study resulted in the development of various neutron-sensitive coated detectors and the Li^6 epithermal neutron spectrometer system, which consists of a Li^6-sandwich detector and a complete, integrated electronic system.

The techniques investigated for applying neutron-sensitive materials to detector surfaces included solution evaporation, vacuum evaporation, and electrodeposition. Solution evaporation is preferable when a thick coating of B^{10} or U^{235} is desired for maximum sensitivity. Vacuum evaporation is preferable when very thin uniform films of Li^6 and Li^6F are required on the detector surface. The highest sensitivity to thermal neutrons is obtained with a thick coating of B^{10}, because of its high cross section and large number of atoms per unit weight as compared to U^{235}. Thin dead layers are essential to good counting efficiency, e.g., a 0.5 μ dead layer will reduce the counting efficiency of a B^{10}-coated detector by as much as 36 percent. A thermal neutron source was used to observe the response of each coating material deposited on the detectors as a function of dead layer and radiator thickness. Theoretical relationships depending on range-energy relationships were derived; these results adequately predict the response of coated detectors as a function of converter material thickness, detector dead layer, and discriminator settings.

The detector developed under this program for the epithermal neutron spectrometer system consists of a layer of Li^6F sandwiched between two silicon detectors in a hermetically sealed package. The electronic system is fully transistorized except for two subminiature vacuum tubes used to attain very low noise in the charge preamplifier. The system is capable of counting at rates up to 10^5 counts/s for a coincidence-gate resolving time of approximately 0.1 μs. The observed shape of the sum peak produced by thermal neutrons is in substantial agreement with that predicted theoretically. A typical value of 200 keV full width at half maximum (FWHM) was observed for the thermal sum peak with a coincidence resolving time of $\approx$ 0.1 μs.

The observed spectrum of the 2.5 MeV neutrons from the D+d reactions showed a broad distribution extending up to 4 MeV. This was consistent with the anticipated neutron spectrum emitted from the self-replenishing deuterium target. Because of a number of uncertainties in the Li^6 spectrometer adjustment, this result should be considered preliminary. An effort to observe 14-MeV neutrons was unsuccessful because of the high background counting rate from competing reactions. At its present stage of development, the Li^6 spectrometer is useful for measuring neutron energies up to $\approx$ 6 MeV. Above this energy the pulses from the $Si^{28}(n,p)Al^{28}$ reaction predominate and obscure the signals from the $Li^6(n,\alpha)T$ reaction of interest.

FOREWORD

This revision of the final report, written by personnel of Solid State Radiations, Inc., Los Angeles, California, contains results of research conducted by them for the U.S. Army Nuclear Defense Laboratory under Contract DA18-108-405-Cml-1012. The work was sponsored by the Defense Atomic Support Agency under their nuclear weapon-effects research subtasks, 06.001 and 06.039.

A Preprint of this report was published and distributed by the U.S. Army Nuclear Defense Laboratory in December 1963 as an expedient means of providing information to the scientific community. The Preprint, which is superseded by this revision, should be destroyed in conformance with paragraph 11.c.(1) of AR 70-31.

BLANK PAGE

CONTENTS

LIST OF FIGURES

LIST OF FIGURES

NEUTRON DETECTION AND SPECTROSCOPY WITH SEMICONDUCTOR DETECTORS

1. INTRODUCTION

During the past few years, the semiconductor detector has gained general acceptance in the field of charged particle spectroscopy[1,2]. Many features make it very attractive, e.g., small size and weight, ruggedness, linear response, fast time response, high stopping power relative to gases and low electron-hole pair ionization energy. The current project was undertaken to extend the use of semiconductor detectors to include the observation and energy measurements of neutrons. The initial approaches to the problem included the direct application of neutron-sensitive materials to the detector surface, the use of the Li^6-sandwich spectrometer, and of a system of stacked detectors using absorbers as a means of determining low-energy neutron distributions. The effort was reasonably satisfactory in that it resulted in the development of a number of detectors useful as thermal-neutron or threshold-detection devices. The approach that showed the greatest possibilities was the Li^6-sandwich spectrometer[3], with which it was anticipated that good energy resolution could be obtained for neutrons over a relatively wide energy range. This feature seemed to overshadow the advantages of either the threshold-detecting devices or a system of stacked devices; as a consequence, the bulk of the effort in the project was directed toward the development of the Li^6-sandwich detector and the associated electronic system.

In general, the detection of neutrons requires observation of secondary charged particles produced in a neutron reaction. The particular reaction and the method for utilizing it depends on the intended application of the device and the nuclear properties of the material, e.g., the cross section and possible threshold for the reaction. Any high-resolution device must depend on a reaction in which the energy of the charged particle emitted is a single-value function of the incident neutron energy. Such a relationship exists in reactions with Li^6 or He^3, in which the total energy of the two particles formed in a reaction will equal the reaction energy or the Q of the reaction plus the incident neutron energy. The use of materials of this type is advantageous, since the total energy of the emitted particles is independent of the direction of the incident neutron. The energy of proton recoils from hydrogenous materials depends on their direction with respect to the incident neutron. However, with proper collimation, proton recoils will yield useful energy information.

By contrast, materials depending on a threshold reaction are essentially "go, no go" devices, wherein no correlation exists between the incident neutron energy and the resulting charged particle energies. This is particularly true in fission materials such as U^{238}, Th^{232}, and Np^{237}. The attainment of good energy resolution and usefulness in an isotropic flux were considerations which made the Li^6-sandwich approach seem much more fruitful than any of the others.

The present report is a summary of the work done on this project. A substantial part of this work was presented in earlier interim reports but is repeated here for the sake of completeness. In particular, the section on the electronic system for the Li^6 spectrometer is repeated verbatim. A discussion of the evaluation of the system, which was completed after the last interim report, is included here as new material. Other material presented here for the first time covers the work on a study of the effects of dead layers and radiator thickness on the efficiency of simple coated detectors.

The second section of the report discusses some general considerations of the detector itself and ways of using it for neutron detection. In particular, this included a discussion of appropriate techniques for detector fabrication and for applying various neutron-sensitive coatings. Theoretical methods for calculating energy distributions for coated detectors and for the Li^6-sandwich detector are developed in the third section. The electronic system for the Li^6 spectrometer is included as the fourth section. The fifth section contains a discussion of the evaluation of the spectrometer and experimental results from observations of the various coated detectors. A final section is concerned primarily with an evaluation of the present state of the art and includes a number of suggestions as to how the devices could be improved.

2. METHODS OF UTILIZING SEMICONDUCTOR DETECTORS FOR NEUTRON OBSERVATIONS

2.1 Semiconductor Radiation Detector

Some general comments on the operation and fabrication of semiconductor detectors are presented in order to indicate their potential and limitations as neutron detectors.

The semiconductor radiation detector is basically an inverse biased p-n junction. The slowing down of charged particles passing through the depletion region in the vicinity of the p-n junction produces hole-electron pairs which are swept out by the electric field to give rise to an electrical signal.

The p-n junction is formed by a shallow diffusion of phosphorous into a surface of high-resistivity, p-type silicon. The depth of the depletion region (in meters) is given [4] by $X = (\kappa \epsilon_0 V/2\pi qN)^{1/2}$; where $\kappa = 12$, the relative dielectric constant for silicon, $\epsilon_0 = 8.85 \times 10^{-12}$ F/m, V = potential difference (in volts) across the region, q = electronic charge (in coulombs), and N = concentration of ionized donors or acceptor atoms per unit volume (in cubic meters) in the barrier layer. Although a depletion region exists on both sides of the junction, the region on the n side will be trivial due to the relatively high doping of phosphorous and corresponding large N on this side. The above expressions may be written in the convenient, approximate form [1]: $d \approx (1/3)(\rho V)^{1/2}$, where d is numerically equal to the depletion depth in microns, ρ is the resistivity in ohm-centimeters, which is proportional to 1/N, and V is the applied bias potential in volts.

The factor 1/3 is dimensional and has the units of $(\epsilon\mu)^{1/2}$, where $\epsilon = K\epsilon_0$ given above, and μ is the value of the majority carrier mobility, 500 cm^2/Vs for holes and 1500 cm^2/Vs for electrons. The practical maximum depletion depth attainable with very high quality silicon, i.e., material in which the resistivity ρ is in the order of a few thousand ohm-centimeters, is approximately 300 μ. This is the approximate range in silicon of 25-MeV alpha particles, 9.5-MeV tritons, or 6-MeV protons.

To maintain charge neutrality across the junction, a space-charge layer will be formed on either side of the depletion region. Electrically, this will be similar to a parallel plate capacitor having a value of capacitance directly proportional to the area and the dielectric constant and inversely proportional to the spacing or the depletion depth. A particular p-n junction will therefore exhibit a capacitance proportional to $V^{-1/2}$. This detector capacitance is significant in the consideration of time dependence of the device and in the design of an appropriate input coupling to an electronic amplifier. A charged particle moving through the depletion region will lose energy with the formation of hole-electron pairs at the rate of one hole-electron pair per 3.5 eV energy loss. These pairs will be swept out by the existing electric field across the region and will produce a charge increase on the detector capacitance proportional to the energy loss of the charged particle in the depletion region. If the charged particle is completely stopped in the depletion region, this charge will be proportional to the initial charged particle energy less any loss suffered in traversing the n-region or dead layer.

The collection time of this charge will depend on the applied bias voltage and the characteristics of the particular device, but will typically be in the order of a few nanoseconds. To avoid loss of charge due to recombination, the silicon carrier lifetime must be long compared to this collection time.

Pulses produced by incident gamma rays will be small because of the low specific ionization of the secondary photoelectric, Compton, or pair-produced electrons. Therefore, pulses originating from gamma rays may be easily eliminated by electronic discrimination.

The basic steps in manufacturing the detector are as follows: a wafer of p-type silicon is cut and polished to the desired size; phosphorous is diffused into the surface by exposing the silicon wafer to a phosphorous vapor for a few minutes at ≈ 1000°C, thereby forming an n-p junction near the surface of the silicon; the back and edges of the wafer are etched to remove this n-type surface except on the front side of the unit; the device is completed by applying some material to protect the exposed junction, attaching electrical leads, and mounting the device in a usable case.

Ideally, the detector should have a diffusion depth, or dead layer, approaching zero thickness to minimize the loss of energy

of incident-charged particles in passing through this region. In practice, the n-type surface must be thick enough to permit electrical lead attachments and provide a relatively low electrical sheet resistivity necessary to obtain a uniform electric field in the device. Surface leakage over the edges of the junction should be minimized to keep the electrical noise low. This requires keeping the junction extremely clean, or free of contamination.

At the present state of the art, the problem of surface leakage has been circumvented to a great extent by employment of the guard-ring principle. A circular groove is etched into the sensitive surface of the detector; thereby, a central sensitive region within the circle, and a region completely surrounding this central region are formed. The central region is connected to the bias supply through a load resistor over which the pulse potential is developed, while the outside region or guard ring is connected directly to the bias supply. With this arrangement, both regions will be at approximately the same potential; however, surface-leakage current will be bypassed directly to the supply rather than passed through the load resistor to contribute to the signal. While the guard-ring detector does offer the advantage of reducing the effect of leakage, its primary limitation is that the area of the sensitive region is only approximately half the total area of the silicon wafer used.

2.2 Neutron Interactions in Silicon

Utilization of the semiconductor radiation detector for observing neutrons will generally depend on observing a secondary charged particle produced by a neutron reaction in material external to the silicon itself. Direct interactions between neutrons and silicon will give rise to effects which must be evaluated to understand the operation of a particular neutron-detecting device. The direct interaction between neutrons in silicon that must be considered are thermal-neutron capture and fast neutron (n, p) and (n, α) reactions.

The thermal-neutron absorption cross section in silicon is ≈ 0.10 barn   The major fraction of thermal absorptions occurs in the lower mass isotope 28, resulting in the formation of Si^{29}, which is stable. Similarly, neutron absorption in Si^{29} produces the stable isotope Si^{30}. The gamma rays emitted in each case will contribute only to low-energy noise in the detector. The small fraction of neutrons captured in Si^{30} results in the formation of Si^{31}, which decays with a 2.6-hour half-life to stable P^{31} by beta emission. This reaction contributes only to low-energy noise in the detector. High-energy neutrons may interact directly with silicon, producing either protons or alpha particles. In the process, a neutron is absorbed, forming an excited nucleus which may give up its excess energy by evaporating either a neutron, proton, or alpha particle[5]. The probability of producing a particular particle is a function of the available energy in excess of the binding energy of the particle and the density of energy levels in the residual nucleus. By use of available cross section data for the (n, p) and (n, α) reactions in

10

various materials[6], nuclear level density parameters have been de-
rived. From these results the cross section for the (n,p) and (n,α)
reactions in silicon have been calculated[7]. From the experimental
data, the cross section for the (n,p) reaction increases sharply
from zero at the 3.86 MeV threshold* to 0.25 b at 12 MeV. The theo-
retical (n,p) cross section reaches a maximum of 0.30 b at 12 MeV
and falls off to 80 mb at 20 MeV. The calculated cross section
for the (n,α) reaction increases from zero at 2.66 MeV to the maximum
value 60 mb at 14.1 MeV.

This boiling-off process results in the emission of charged
particles with random energies following a somewhat complex distribu-
tion depending on the energy of the excited nucleus[8]. As an exam-
ple of the general nature of this distribution, it is noted that the
proton energy distribution resulting from interaction with 14-MeV
neutrons extends from zero to 10 MeV with a peak at approximately
2.5 MeV.

The broad and complex distribution of charged particles
produced by the (n,p) or (n,α) interaction in silicon essentially
precludes using this reaction to determine the incident neutron energy,
except possibly as a threshold indication. For incident neutrons with
energy greater than 6 MeV, the cross section for these reactions is
large enough to complicate seriously the use of the silicon semicon-
ductor detector to measure other charged particles in a fast neutron
field.

2.3 Neutron Detection

Neutron detection generally depends on observation of charged
particles produced in some neutron reaction in material placed in
proximity to the detector. Several materials are useful for this
application. In particular, B^{10}, due to its very high cross section,
is used as a radiator material for observing thermal neutrons. Li^6
may be used as a simple thermal-detection coating material; however,
because of the relationship between the incident neutron energy and
the maximum energy of the triton produced, the Li^6-coated detector
may be used to indicate the maximum neutron energy emitted from a
source. In addition, the Li^6 is most useful as a material for the
spectrometer sandwich detector, which will be discussed in detail in
a later section. The neutron reaction with He^3 is of considerable
interest, since the resulting two charged particles will share the
energy of the incident neutrons plus the reaction energy. The inci-
dent neutron energy can be inferred from the sum of energies of the
two charged particles, as is done with the Li^6 sandwich. While a
He^3-sandwich detector might offer the advantage of less energy-strag-
gling than is encountered in the Li^6 sandwich, a development effort
was not made, due to the anticipated difficulty in containing He^3 in

---

*More precisely, "threshold energy" refers to the necessary kinetic
energy of the neutron in the LAB system, i.e., $E_{th} = -(M_x+M_X/M_X) Q$,
rather than the required kinetic energy in the CM system, i.e.,
the negative Q value. This latter value is used here.

a practical working device. Various threshold-type materials, such as U^{238}, Th^{232}, and Np^{237}, are available but cover only a small range of energy. The inherent advantage of these materials is that the resulting fission-fragment energy is very large as compared to noise or any reactions caused by light-weight charged particles. This permits discrimination against the lower-energy events.

A discussion of the techniques for applying material to detectors is given in the following paragraphs. The development of the electrodeposition was not covered directly by this project; however, comments are included for completeness. The detector units were evaluated for noise and normal diode response before and after the coatings were applied. Except as noted in the following discussion, yields were satisfactory.

2.4 Coating Techniques

Basically, three techniques were used for applying neutron-sensitive coatings to detector surfaces: evaporation out of solution, vacuum evaporation, and electrodeposition. The choice of approach for any particular material depended on the nature of the material itself and the intended use of the detector.

The solution-evaporation technique is reasonably straight-forward and simple. It involves dissolving the neutron-sensitive material in a solvent, applying a quantity of the solution to the detector surface, and allowing the solvent to evaporate, thereby leaving a dry deposit of the desired material. A number of problems had to be overcome in order for this approach to be practical. For example, the residual deposit was required to have good uniformity and adherence to the detector surface. Secondly, the solvent could not react directly with the silicon surface, nor contribute to the contamination of the detector junction. These restrictions immediately eliminated use of strong acids as solvents. A mechanical problem was involved in that the solution, when deposited on the detector surface, at times formed a meniscus near the edge of the detector, with the result that the bulk of the material was deposited in a peripheral ring rather than uniformly over the surface. This problem was reduced by applying a nonwetting silicone coating around the edge of the detector surface before applying the solution. In some cases there was a tendency to form large crystals on the dry surface rather than a deposit of uniform thickness. With the formation of large crystals, part of the detector surface was actually not coated and the sensitivity was poor. Crystal formation was controlled by the choice of solution and the drying procedure.

Considerable effort was made to determine the best approach for depositing B^{10} on detector surfaces. While the B^{10} is in itself useful only as a thermal-neutron detector material, the techniques involved are essentially applicable to other materials. The first approach to applying B^{10} in a solution involved dissolving boron in nitric acid, applying the solution to the detector surface, and evaporating off the liquid. This method yielded uniform B^{10} coatings with

controllable thicknesses; however, the acid caused so much deterioration of the detector that the yield was poor or the reliability was very limited. An additional problem was encountered when the material was applied as a true solution; the active atom combined as a salt, with the result that the anion contributed substantially to the bulk of the surface and reduced the sensitivity significantly.

A variation of the solution-evaporation technique consisted of applying B^{10} in a suspension of chloroform, methanol, and isopropyl alcohol. Since the boron in this case was not actually dissolved in the suspension, the resulting surface was composed of particles having chemical composition and initial size such that very thin uniform surfaces could not be obtained by this method. Slow drying was required with this technique to prevent bubbling, which would cause nonuniformity.

The solution-evaporation technique was used with good success in depositing both U^{235} and U^{238}. The uranium solution was formed by either dissolving the metal in nitric acid or by dissolving the uranium oxide in a combination of nitric and hydrochloric acid. The resulting solution was neutralized with ammonium hydroxide and thereby yielded a precipitate. This was extracted from the solution by methanol, in which the salt was slightly soluble, and then evaporated to a powder form. A small quantity of methanol was added to this powder, which produced a slurry that was applied to the detector surface and dried to form the final coating. A slight residue from the methanol acted as a binder so that the final surface had good mechanical stability. Since uranium is a heavy atom, the fractional contribution of any material forming a salt with the uranium or any binder material does not significantly reduce the sensitivity of the device.

In general, the solution-evaporation technique was considered adequate for cases in which the surface uniformity was not critical, e.g., if the energy depended on threshold rather than the energy of the emitted particle.

2.5 Vacuum Evaporation

Vacuum evaporation is a technique useful for applying materials where a thin, uniform coating is required. In this technique the detector is mounted in a vacuum chamber near the heater containing the material to be deposited. When a good vacuum was attained, the temperature of the material was raised to a point where evaporation was fairly rapid. Particles emitted by the evaporation process followed essentially straight-line paths and stuck to any surface they encountered. A mask over the detector edges was used to define the region on which the material was deposited. This technique has been used on a routine basis for depositing very thin films of materials such as silver, aluminum, and gold. However, the technique is limited by a number of factors. The material to be deposited must have a melting point that is low in comparison with materials used for the heater element. Further, the heater must be an inert material

that does not interact with the material being evaporated. To be of practical use, the evaporated material must adhere to the silicon surface and form a reasonably rugged surface.

The vacuum-evaporation technique was used successfully to deposit uniform coatings of lithium metal and Li^6F. These materials melt at relatively low temperatures, and a 1-mil-thick tantalum heater or boat was quite adequate for this evaporation. Lithium-fluoride evaporation was accomplished by (1) placing the detector in a jig about 25 cm above the heater, (2) loading the tantalum heater with the required amount of the salt, (3) evacuating the system $\approx 10^{-6}$ mm of Hg, and (4) gradually increasing the temperature of the tantalum heater to a dull red glow or to a temperature at which the Li^6F would melt and form a molten globule. Too rapid an increase in temperature at this point would cause sputtering and a resultant loss of material, or nonuniformity in deposition. It is possible to evaporate lithium metal by this same technique. Due to the interaction of the metal with air, it was normally supplied immersed in an inert oil. The lithium metal with some oil adhering to its surface was placed in the tantalum boat and the system was evacuated. The evaporation technique was, of necessity, modified to a two-step process. First, the entire detector system was masked while the oil was evaporated off at a low temperature. Secondly, the mask was removed and the temperature was increased, as was done with the lithium salt. The metal evaporation generally required a much more careful masking of the detector junction, since extremely small quantities of lithium contamination on the junction could destroy the detector. Use of pure lithium is practical only in cases where the detector can be hermetically sealed in either a vacuum or an inert atmosphere. A few successful Li^6 metal evaporations were made, but because of the added difficulties this technique was not routine.

The vacuum-evaporation technique offers the advantages of good controllable thickness and uniform surfaces, but it is not applicable to all materials. While evaporation of uranium can be accomplished, the contamination problem makes such an approach practical only if complete equipment can be provided for this single operation. Other materials, such as B^{10}, are difficult to evaporate, due to their very high melting point. In addition, some chemical combination with the heater occurs at the required high temperature, so that the composition of the deposited surface is not certain. The compound H_3BO_3 may be evaporated at lower temperatures; however, the inactive atoms in the compound contribute to stopping the alpha particles and thereby reduce the sensitivity of the resulting surface by a factor of $\approx 1/6$.

2.6 Electroplating

An electroplating technique was developed to deposit thin, uniform layers of U^{235} and U^{238}.

An electroplating apparatus was constructed which consisted of parallel-plate electrodes in a 150-ml beaker containing

the electrolyte. This was immersed in a constant temperature bath. The electrolyte was prepared by dissolving uranium or uranium oxide in an acid solution, then adding ammonium hydroxide to adjust the pH to 4 or 5. An electrolyte was made by adding ammonium oxalate. Contamination by spread of uranium was not a problem since the material was totally contained in the electrolyte. Uniform deposits of uranium up to 1 mg/cm^2 could be applied successfully by this technique, if the pH of the solution was carefully controlled during the plating process. This was effectively accomplished by adding either ammonium oxalate or oxalic acid as required.

Efforts were made to plate uranium onto various materials including aluminum, nickel, and the detector itself. The back side and edges of the sample to be plated were masked by an acid resistant wax and immersed into the electrolyte solution. Plating to the detector surface was accomplished by evaporating a thin layer of gold onto the detector and by using this surface as the cathode in the plating cell. The most critical problem in this technique was to ensure that the masking was adequate to protect the detector junction from any contact with the electrolyte during the plating. This procedure was practical only where an extremely thin coating was required.

2.7 Materials

In general, the materials used in the construction of neutron detectors were chosen to satisfy two requirements: (1) The material should be such that its perturbing effect on the flux to be measured, due to neutron absorption or scattering, will be minimal; (2) The material should not become radioactive during the measurement. These requirements were important and generally not difficult to fulfill. The structural material was aluminum, which has low cross section, good thermal and electrical conductivity, is readily available and easily workable. Hydrogenous materials were avoided; therefore, teflon was used for small spacers and insulators in the detector assembly.

Radiation damage due to fast neutrons became significant following a total exposure of 10^{13} to 10^{14} nvt. Damage caused by either gamma or thermal neutrons was not significant until extremely high doses were sustained. Note that a comparable radiation dose generally produced observable damage in other semiconductor devices, such as transistors.

2.8 System Approaches

At the beginning of the project two techniques for neutron-energy measurement were considered. These were the Li^6-sandwich spectrometer and a stacked-detector absorber array. The bulk of the effort in the project was devoted to the development of the Li^6-sandwich detector and associated electronic system. This is discussed in detail in a later section of this report.

The stacked-detector absorber array was intended to be used as a device for determining low-energy distributions in the thermal

15

and epithermal range. A collimated beam of neutrons would be attenuated by an amount depending on the cross sections of the absorber materials between successive detectors and the energy distribution of the incident beam. A comparison of the relative response rates of detectors at various depths in the array could in principle indicate the energy distribution of neutrons in the beam.

The problem of primary concern with this type of system was the range of counting rates that would be required. In order to obtain meaningful results, it would be necessary to attenuate the beam several orders of magnitude. This would, in turn, require counting systems having the same order of magnitude of difference in their total storage capacities. Because of the limited capacity of conventional counting systems, it would be difficult to measure relative rates differing by more than approximately 4 decades with any reasonable statistics. Present data-handling techniques would, however, permit a straightforward computation of results by use of this system. Essentially no effort beyond the feasibility considerations was made on this device; however, such a system would be useful for certain applications where detailed information on low-energy neutron distributions is important.

2.9 Li^6-Sandwich Detector Construction

The construction of a sandwich detector was accomplished in three steps:

1. The fabrication of the p-n junction detectors.
2. The coating of one detector with Li^6.
3. Assembly and encapsulation of the sandwich into a hermetically sealed package.

Except for the final mounting, detectors to be used for the Li^6-sandwich assembly were fabricated by the conventional procedure. Extreme care was exercised in selecting detectors that matched one another in operating characteristics, physical size, and dead layer. While guard-ring detectors have generally been used for this application, a few conventional one-square-centimeter detectors were used for comparison, and satisfactory results were obtained.

Coating by evaporation was performed as described in a previous paragraph except that before the evaporation, the detectors were attached to the aluminum blocks which supported them in the final assembly. The thickness of the deposited salt was determined with fair precision by weighing a large piece (≈ 100 cm^2) of aluminum placed in the vicinity of the detectors during evaporation. Uniformity of the coating on the detector surfaces was observed by means of a reflected optical interference pattern. This technique was used to deposit films ranging from 50 to 300 $\mu g/cm^2$.

A sketch of the package for the Li^6-sandwich detector is shown in Figure 2.1. This unit appears to have good ruggedness and operational stability. The unit consists of two detectors supported

16

.125 Dia. Tube

.25

R

.68 Dia.

Fits std. 7 Pin Base

FINAL ASSEMBLY

Detector

Converter

Detector

Mounting Bracket

INTERNAL ASSEMBLY

Mounting Bracket

Detector

Converter

Detector

EXPLODED VIEW
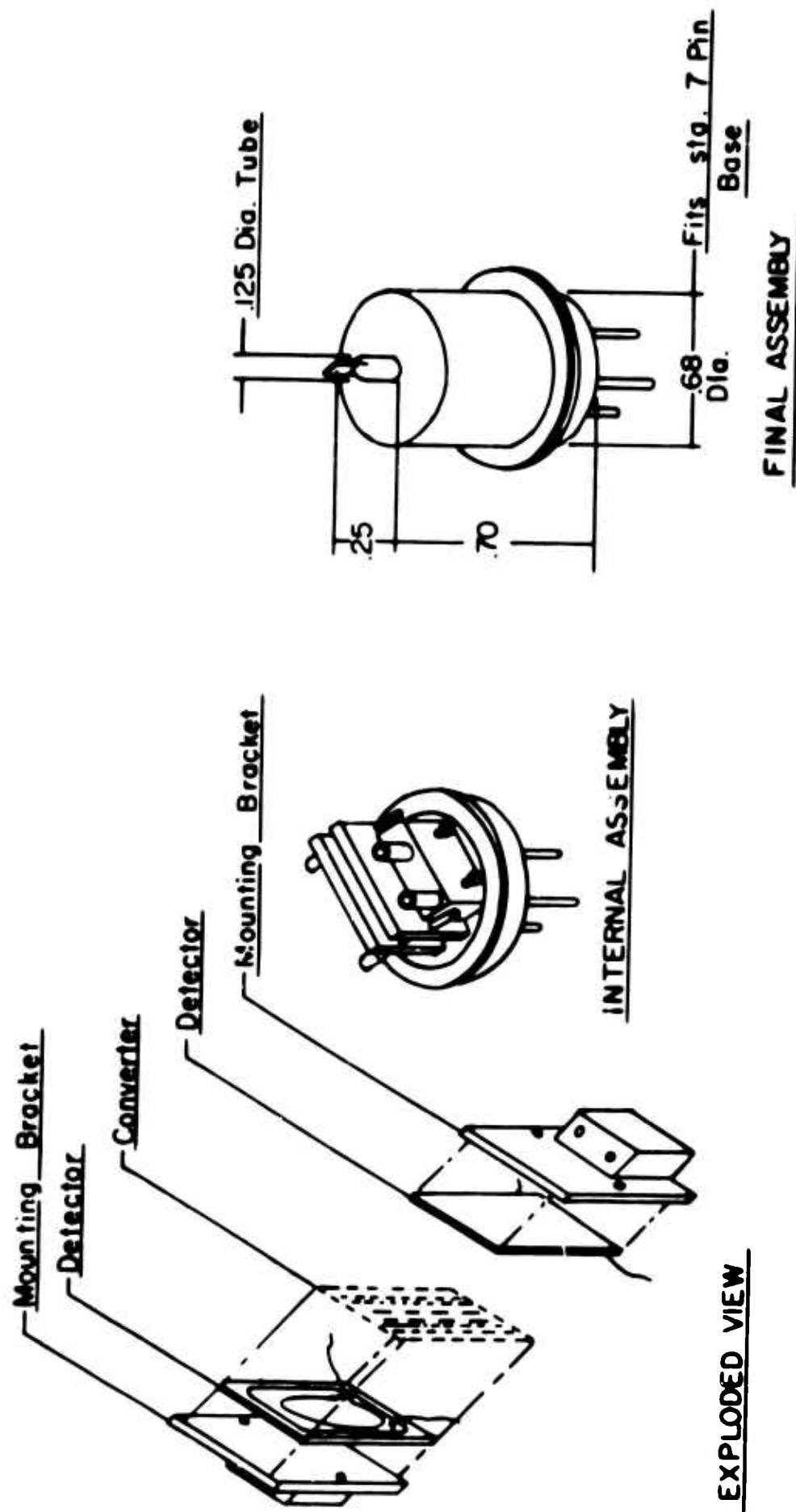
DIMENSIONS SHOWN ARE APPROXIMATE

Figure 2.1 Li^6 sandwich assembly.

17

by aluminum blocks which, in turn, are supported by base pins insulated by means of teflon sleeves. The spacing between the detectors is adjusted by means of two teflon screws through the two aluminum blocks. After the spacing adjustment, the detector support blocks are held in place by means of teflon set screws pressing against the base pins. Electrical connections are made from the crystal to the pins by means of gold wires that are spotwelded to the desired pins. After assembly of the internal parts, the outside cylindrical can is added and cold pressed to the base to form a hermetic seal. The final step in the procedure involved evacuating air from the unit and pinching off the pump-out tube. The completed unit fits a standard seven-pin tube socket and over-all dimensions are approximately 7/8 inch in diameter and 7/8 inch high, exclusive of the pins and pump-out tube.

An effort was made to avoid using any hydrogenous material or highly neutron-absorbing materials that could perturb the neutron flux or become highly radioactive during its use in a neutron field.

The procedure for assembling the Li^6 metal coated unit was essentially the same, except the entire procedure was carried out in a dry box containing an inert atmosphere. This arrangement, however, lacks an adequate means of testing the units before final encapsulation.

3.   THEORETICAL CONSIDERATIONS

The use of semiconductor detectors for neutron detection generally depends on observing a charged particle produced in some neutron-sensitive material placed in proximity to the detector. The material may contain B^{10}, Li^6, a fissionable material, or some hydrogenous material, depending on the intended use of the detector. This neutron-charged particle converter material may be applied as a thin film directly to the sensitive surface of the detector or to some base material which, in turn, may be placed in close proximity to the detector surface. The energy distribution of charged particles observed by the detector will depend on the initial energy of the charged particles and the slowing-down distance the charged particles must travel before entering the sensitive region of the detector. A theoretical analysis of the neutron-sensitive coated detector response was performed in order to help understand the relationship between such factors as radiator thickness, detector dead layer, discriminator settings, and detector efficiency. The response of the Li^6-sandwich detector has been calculated for a number of special cases of interest.

3.1   Preliminary General Forms

The range of heavy charged particles may be approximated by the empirical equation

$$R = K E^{\gamma} + a,$$

(3.1)

18

where K, γ, and a are constants chosen to give the best fit to data in the range of interest, and E is a dimensionless quantity numerically equal to the charged-particle energy in MeV.

The above expression for R adequately describes the shape of the range-energy curves over the energy region of interest for the present purposes, i.e., from near zero to a few MeV. Although the function does not fit the data for E near zero, this does not significantly affect the following derivations which depend on the shape of the function rather than its absolute value. The value of the curve-fitting constant, a, will not be significant for the present discussion.

The best fit to the data of Gobelli[9] for the range of alpha particles in silicon in microns is obtained when $\gamma = 1.45$ and $K_\alpha = 2.13$ microns, a = 2.2 microns. By use of the same type of range-energy relationships and data from Nuclear Data Tables[10], these constants for tritons are $\gamma = 1.45$ and $K_T = 10.0$ microns. Since the slowing-down rate of heavy charged particles is approximately proportional to the material density, Equation (3.1) will be applicable to other material if K and R are expressed in milligrams per square centimeter.

A charged particle produced with initial energy E_0 will have a range R_0. Then from (3.1),

$$R_0 = K E_0^\gamma + a. \tag{3.2a}$$

After traveling a distance r, the residual range $(R_0 - r)$ and energy E will also satisfy (3.1), i.e.,

$$(R_0 - r) = K E^\gamma + a. \tag{3.2b}$$

Substituting into (3.2b) the expression for R_0 in (3.2a) gives

$$r = K (E_0^\gamma - E^\gamma), \tag{3.3}$$

$$\text{or} \quad E = (E_0^\gamma - r/K)^{1/\gamma}. \tag{3.4}$$

The last expression (3.4) gives the energy of an emitted charged particle originally produced with energy E_0 after traveling a distance r in the slowing-down material.

The number of neutron reactions per unit time per unit volume in the neutron-charged particle converter, or radiator material, will be given by

$$n (E_n) = \Phi (E_n) \Sigma (E_n), \tag{3.5}$$

where $\Phi(E_n)$ is the neutron flux and $\Sigma (E_n)$ is the macroscopic cross section for the particular reaction. In general these quantities will be functions of the incident neutron energy E_n. Since the neutron attenuation in the converter material will be small, the terms in (3.5) may be considered constant over the entire converter volume.

The general approach to determining the energy distribution of charged particles observed by a detector involves first finding an expression for the energy of emitted particles that originate in a particular volume element in the radiator and then travel some distance before reaching the sensitive region of the detector. The total distribution is then formed by summing over these volume elements in the radiator. Two methods of performing this summation are presented in order to illustrate the origin of energy distributions and the effects of the parameters involved. While the two approaches give the same final results, each has some advantage of convenience for particular cases. The first method, discussed in Section 3.2, shows clearly the region from which emitted particles of a particular energy originate. The second method, which is given in Section 3.3, uses an integration in which the physical significance of each step is somewhat obscure. However, the form of the summation lends itself to a convenient graphic representation. This permits obtaining graphic solutions for some cases which cannot be handled analytically.

In the following discussion it will be assumed that ranges are expressed in density units such that it will not be necessary to distinguish between materials. Infinite slab geometry will be assumed, since the charged particle ranges are small compared to the detector surface dimensions.

3.2 Energy Distribution - Analytical Form

Consider a detector having a dead layer of thickness d and a radiator (or neutron-charged particle converter) thickness t - d such that the total thickness of the radiator and dead layer is t (Fig. 3.1). The energy distribution of charged particles entering the sensitive (i.e., depletion) region through the small surface element ds will now be calculated. The number of particles produced in a spherical shell between r and r + dr per unit time and in the volume element defined by dθ and θ measured from the normal to the surface is

$$2\pi\, nr^2 \sin\theta\, d\theta\, dr, \qquad\qquad (3.6)$$

where n is given in (3.5). Note that sources exist only in the radiator, and that n will be zero in other regions.

The solid angle at this volume element subtended by the surface element ds is

$$\frac{ds\, \cos\theta}{4\pi r^2}. \qquad\qquad (3.7)$$

By the assumption that the charged particles are produced isotropically, the number emitted per unit time through ds from this element will be
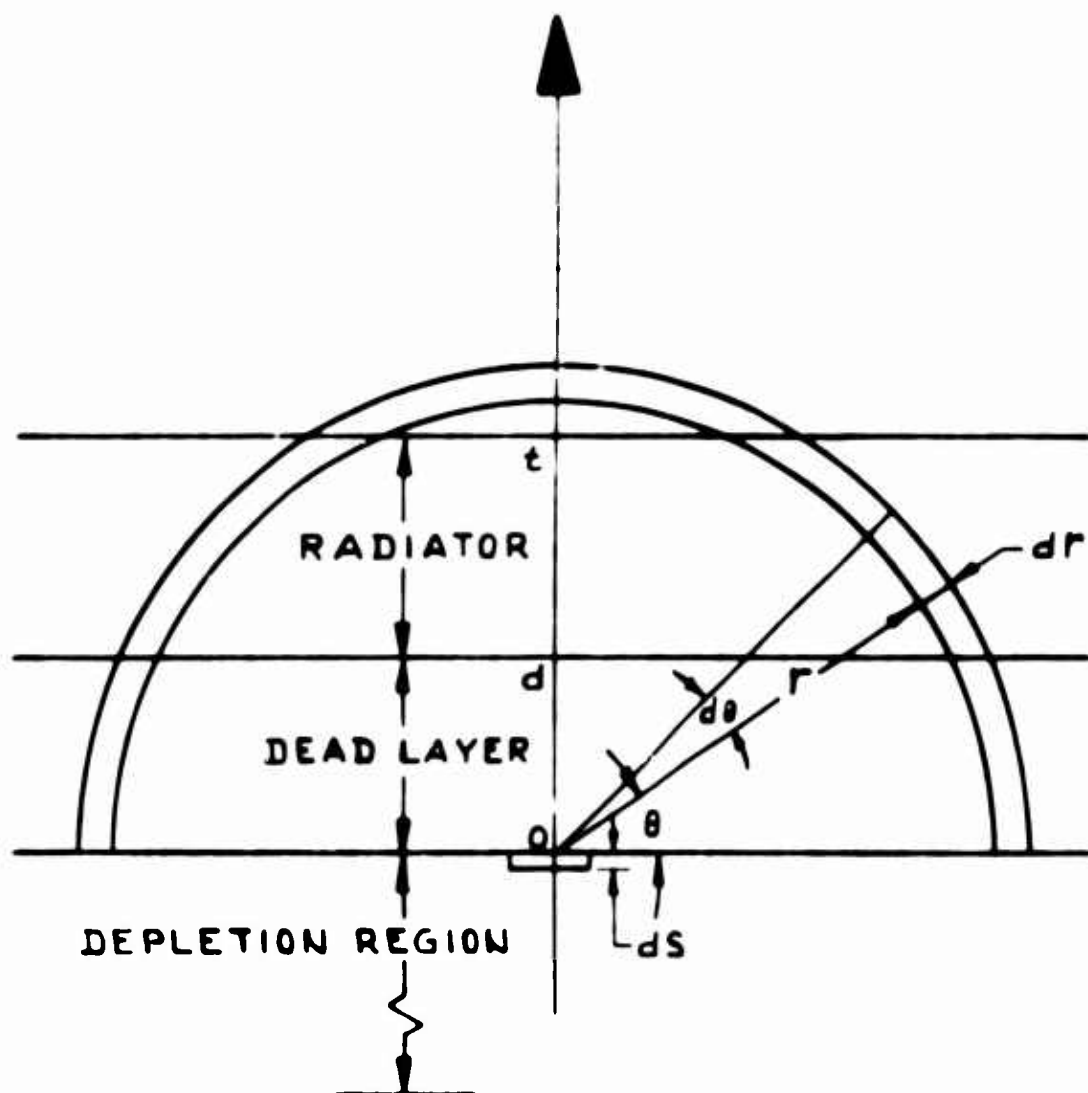
Figure 3.1 First model used to calculate
the distribution of energy deposited
within the detector.

21

$$N(r,\theta)\ dr\ d\theta\ ds = (2\pi nr^2 \sin\theta\ d\theta\ dr)\ \frac{(ds\ \cos\theta)}{4\pi r^2}$$

$$= \frac{n}{2}\ \sin\theta\ \cos\theta\ d\theta\ dr\ ds. \tag{3.8}$$

By substituting the variable

$$\mu = \cos\theta, \tag{3.9}$$

the number of particles emitted per unit area per unit time from the corresponding volume element is

$$N(r,\mu)\ dr\ d\mu = \begin{cases} 0, & \text{for } r < d, \\[2mm] \dfrac{n}{2}\ \mu\ d\mu\ dr, & \text{for } d < r < R, \\[2mm] 0, & \text{for } r > R, \end{cases} \tag{3.10}$$

where R is the maximum range of the charged particle.

The total emission rate per unit area of particles originating in the spherical shell defined by dr about r is found by integrating Equation (3.10) over the appropriate limits of μ, i.e., where $n \neq 0$.

$$N(r)\ dr = \begin{cases} 0, & \text{for } r < d, \\[3mm] \dfrac{n}{2}\displaystyle\int_{d/r}^{1} \mu\ d\mu\ dr = \dfrac{n}{4}\ \dfrac{r^2 - d^2}{r^2}\ dr, & \text{for } d < r < t, \\[5mm] \dfrac{n}{2}\displaystyle\int_{d/r}^{t/r} \mu\ d\mu\ dr = \dfrac{n}{4}\ \dfrac{t^2 - d^2}{r^2}\ dr, & \text{for } t < r < R, \\[5mm] 0, & \text{for } r > R. \end{cases} \tag{3.11}$$

The function $N(r)$ in (3.11) is the distribution or density function of charged particles as a function of r. This can be expressed as a distribution in some other variable, in particular E, providing there is a functional relationship between r and the other variable. In corresponding intervals dr and dE, there must be the same number of particles emitted, i.e.,

$$N(r)\ dr = N(E)\ dE, \tag{3.12a}$$

where $N(E)$ is the distribution function in E. The relationship between these variables from (3.3) is used, and

22

$$N(E) \ dE = - N(r) \ \frac{dr}{dE} \ dE$$

$$= N(r) \ \gamma \ K \ E^{\gamma - 1} dE. \tag{3.12b}$$

The negative sign is used in (3.12b), since the derivative is nega-
tive. When the expression for r from (3.3) is substituted into
(3.11) and Equation (3.12b) is used, the energy distribution is
found to be

$$N(E)dE = \begin{cases} 0, & \text{for } E > (E_o^\gamma - d/K)^{1/\gamma} \\[2ex] \left(\frac{n\gamma K}{4}\right) \dfrac{(E_o^\gamma - E^\gamma)^2 - d^2/K^2}{(E_o^\gamma - E^\gamma)^2} \ E^{\gamma-1} dE, & \text{for } (E_o^\gamma - d/K)^{1/\gamma} > E > (E_o^\gamma - t/K)^{1/\gamma}, \\[2ex] \left(\frac{n\gamma K}{4}\right) \dfrac{(t^2 - d^2)}{K^2 \ (E_o^\gamma - E^\gamma)^2} \ E^{\gamma-1} dE, & \text{for } (E_o^\gamma - t/K)^{1/\gamma} > E > 0, \end{cases} \tag{3.12c}$$

where E_o is the initial energy of the charged particles produced in
the radiator. Energy distributions for several values of radiator
thickness have been calculated from Equation (3.12c) for 3-MeV alpha
particles and are shown in Figure 3.2. Calculated distributions as
a function of dead layer are shown in Figure 5.1. In the limiting
case of zero dead layer and infinite radiator thickness, the total
number of charged particles emitted per unit area per unit time is
found to be

$$\int_0^{E_o} N(E)dE = \int_0^{E_o} \frac{n\gamma K}{4} \cdot E^{\gamma-1} \ dE$$

$$= \frac{nKE_o^\gamma}{4} \approx \frac{nR_o}{4} . \tag{3.12d}$$

Total counting rates above a discriminator setting are found
by integrating over the expression in Equation (3.12c) from the dis-
criminator setting to the maximum energy.

3.3 Energy Distribution - Graphic Solution

An alternative method for calculating the energy distribu-
tion involves calculation of the distribution from a source element at
a particular depth in the radiator and then summation over the thick-
ness of the radiator. Unlike the method above, this approach does not
give any picture of the region from which particles of a particular
energy originate. However, it does yield a result which lends itself
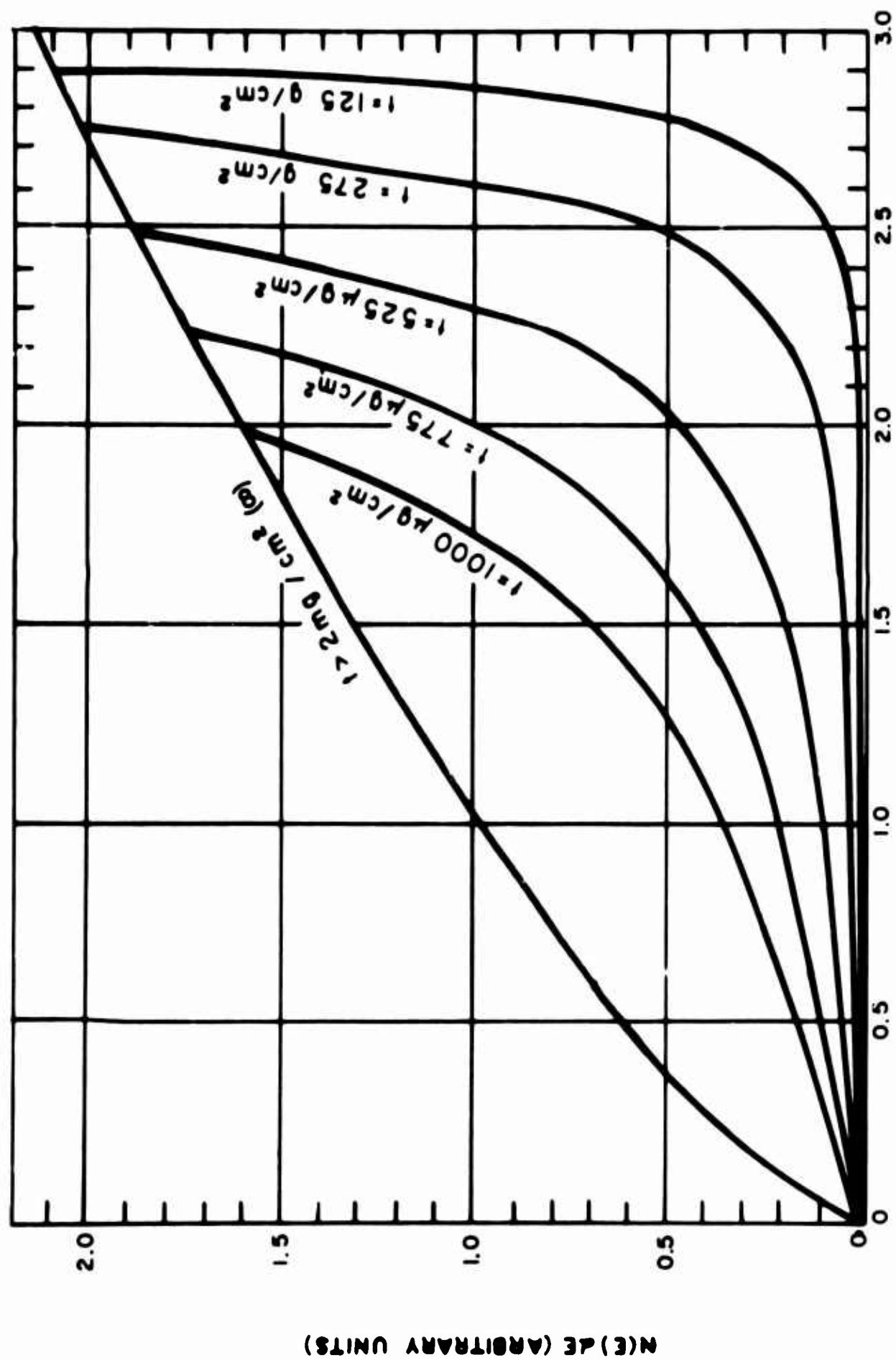to a graphic solution, which may be useful in some cases.

23

Figure 3.2 Energy distribution of emitted charged particles for various radiator
thicknesses (3 MeV) alpha particles) Zero dead-layer case.

24

The number of charged particles formed per unit area in the element of thickness dx at depth x, and emitted in cone $d\theta$ about θ (see Figure 3.3) is given by

$$N(x,\theta)dx \ d\theta = \frac{n}{2} \ \sin \theta \ d\theta \ dx, \ \text{for } d < x < t \text{ and } \frac{x}{\cos \theta} < R). \quad (3.13)$$

In terms of the variable $\mu = \cos \theta$,

$$N(x,\mu) \ dx \ d\mu = \frac{n}{2} \ dx \ d\mu. \quad (3.14)$$

From (3.4) the energy E of a particle originating at depth x in the direction defined by μ will satisfy the expression

$$x = K(E_o^{\gamma} - E^{\gamma})\mu. \quad (3.15)$$

For a particular value of E, Equation (3.15) gives a linear relationship between x and μ, which may be represented by a straight line through the origin when plotted on an $x\mu$-plane. The line corresponding to E = 0 will pass through the points (0, 0) and $(R',1)$, where $R' = KE_o^{\gamma}$ (Figure 3.4). Particles originating from a depth x and in the direction μ, as represented by a point (x,μ) on the $x\mu$-plane, will be emitted with energy E corresponding to the constant energy line through that point. Particles emitted with greater energy must originate from points above that particular constant energy line.

The number of particles emitted in a particular interval will be found by integrating Equation (3.14) over the appropriate intervals of x and μ. Since this will also give a value proportional to the area of the corresponding region in the $x\mu$-plane, this same number can be found by measuring the appropriate area or the plane by any convenient means.

The shaded area in Figure 3.4 corresponds to the region in the radiator from which particles may be emitted with energy greater than E. The corresponding number of particles from this energy interval is found by integrating over this shaded area. The values μ_d and μ_t correspond to directions from which particles are emitted with energy E from the respective depths d and t. Thus, the number of particles emitted per unit area per second, with energies between E and E_o, is given by

$$\int_E^{E_o} N(E) \ dE = \frac{n}{2} \int_{\mu_d}^{\mu_t} d\mu \int_d^{\mu K(E_o^{\gamma} - E^{\gamma})} dx + \int_{\mu_t}^{1} d\mu \int_d^{t} dx \quad (3.16)$$
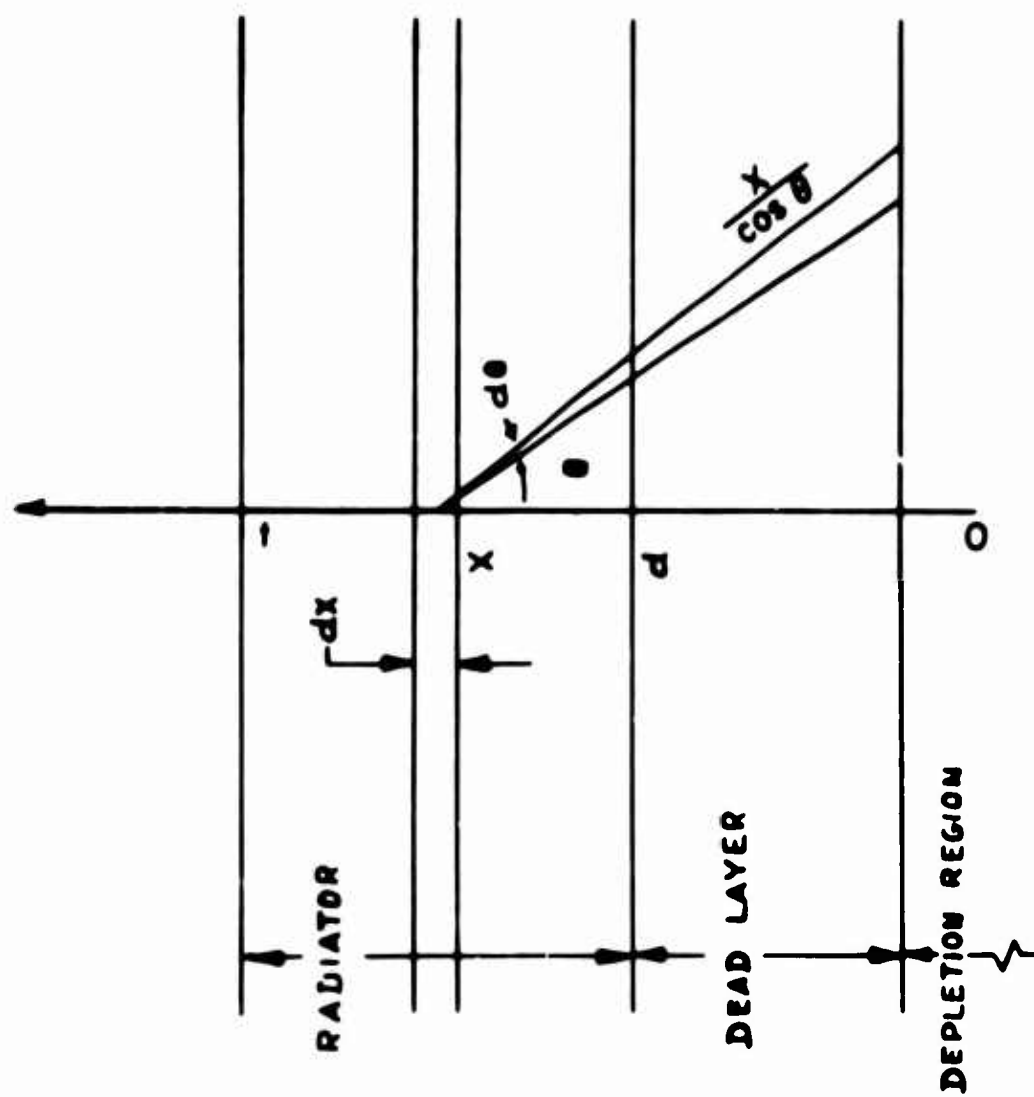
25

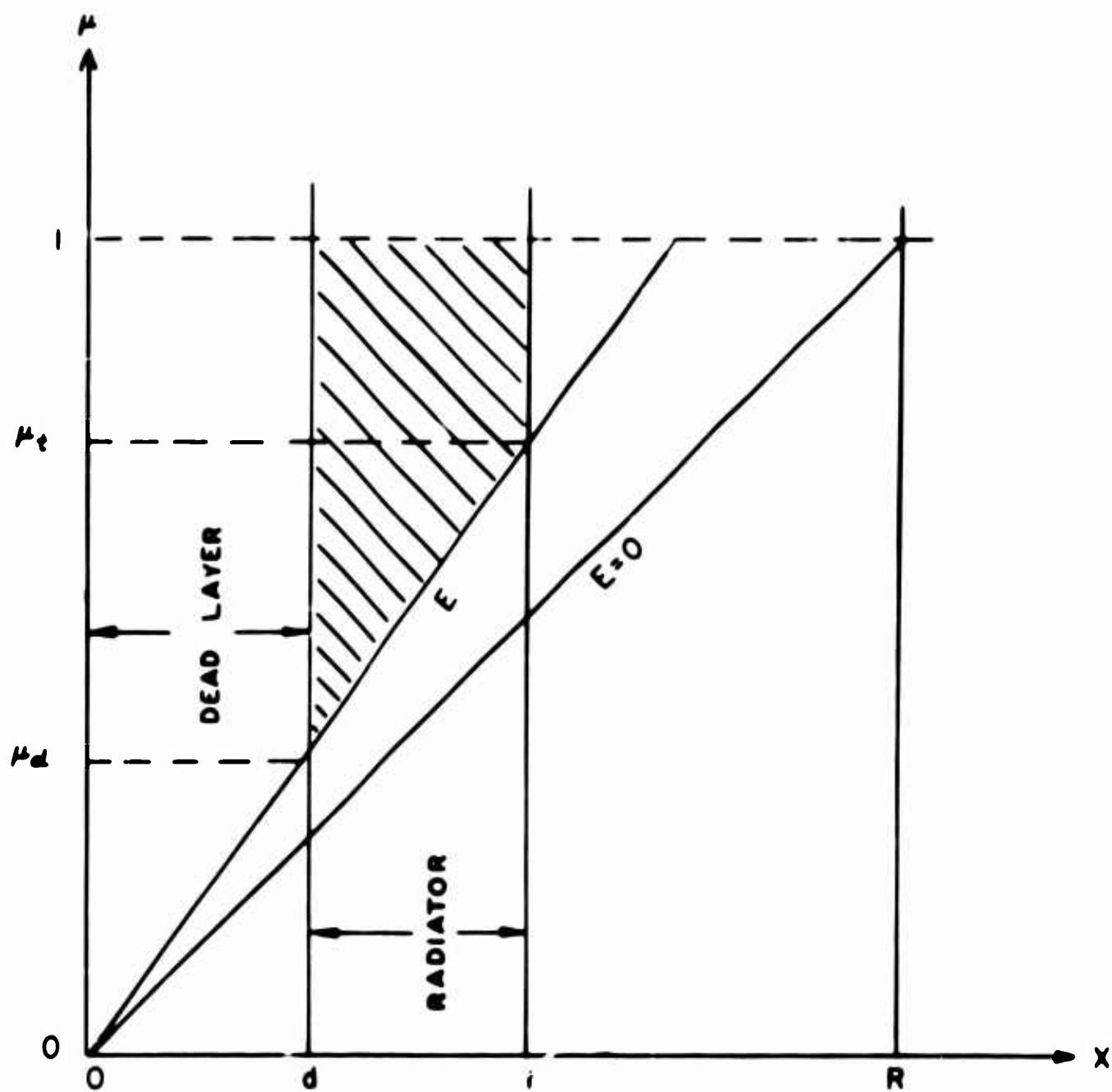Figure 3.3 Second model used to calculate the distribution of energy disposition within the detector.

Figure 3.4   Graphic solution of $x = K (E_o^\gamma - E^\gamma) \mu$.

27

$$\begin{cases} \dfrac{n}{2}\left[t - d - \dfrac{t^2 - d^2}{2K(E'_0 - E')}\right], & \text{when } 0 < E < (E'_0 - t/K)^{1/\gamma}, \\[2em] \dfrac{n}{2}\displaystyle\int_{\mu_d}^{1} d\mu \int_{d}^{4K(E'_0 - E')} dx = \dfrac{n}{4}\dfrac{[K(E'_0 - E') - d]^2}{K(E'_0 - E')}, & (3.17) \\[1em] & \text{when } (E'_0 - t/K)^{1/\gamma} < E < (E'_0 - d/K)^{1/\gamma} \\[1em] 0, \text{ when } E > (E'_0 - d/K)^{1/\gamma}. \end{cases}$$

The density functions $N(E)$ are the negative derivatives with respect to E of the expression in Equation (3.17). These are identical to the results given in Equation (3.12).

The counting rate for detectors with infinitely thick radiators is found by measuring the area in Figure 3.4 of the region above $E = 0$ and to the right of $x = d$, and multiplying by $n/2$. From (3.14), the value is

$$\int_{0}^{E_0} N(E)dE = \frac{n(R' - d)^2}{4R'} \approx \frac{n(R_0 - d)}{4R_0} \qquad (3.18)$$

For zero dead layer, this becomes

$$\int_{0}^{E_0} N(E)dE = \frac{nR'}{4} \approx \frac{nR_0}{4}, \qquad (3.19)$$

in agreement with (3.12d).

Equation (3.19) gives the maximum theoretical counting rate per unit area for a coated detector in which the charged particles are produced isotropically and at a single energy. The difference between the counting rates for the actual range R_0 and the value $R' = KE_0^\gamma$ is due to the constant, a, in Equation (3.1). Any charged particles originating in the radiator at a distance between R' and R_0 from the point of emission would have energies too low to add significantly to the counting rate. In practice, these very low-energy pulses are discriminated against electronically, along with other low-energy pulses originating from gamma-ray interactions and electronic noise. Theoretical maximum counting rates have been calculated for various radiator materials from the R' values in Equation (3.19). These are presented in Table 5.1 for comparison with experimentally observed values.

3.4   Special Cases

The foregoing discussion considered in some detail the case in which charged particles were produced isotropically and at a single energy in a radiator external to, but in direct contact with, the detector surface. The following special cases are also of interest, but they will be mentioned only briefly and not developed in detail.

3.4.1   Internal Sources

The (n,p) and $n,\alpha)$ reactions in silicon result in the production of charged particles within the detector itself, both in the sensitive depletion region and in the undepleted regions on either side of the depletion region. Charged particles produced in the depletion region may give up their total energy in that region, which would result in a pulse proportional to their full energy. Similar charged particles may give up only a fraction of their energy in this region, while charged particles originating outside the depletion region may be finally stopped in the depletion region. The net result will be an observed pulse height distribution having a maximum corresponding to the maximum energy in the charged-particle energy distribution but shifted toward the lower energy end of the distribution. The total counting rate will be equal to the total production rate in the depletion region plus the contributions from the region on either side. The latter contributions can be calculated by methods that were developed in Sections 3.2 and 3.3.

3.4.2   Separation of Detector and Radiator

A convenient technique for studying detector characteristics consists of depositing the radiator material on some base material such as aluminum foil, which can be brought into proximity with the detector surface; thus, the radiation material can be deposited directly onto the detector surface. The observed energy distribution of charged particles is similar to that derived in Sections 3.2 and 3.3, except that edge effects may be significant, and any air between the radiator and detector would effectively increase the dead layer. Actual experiments using this technique were performed, and will be discussed in Sections 5.1 and 5.2. However, the detector-radiator spacing was generally kept small and the units were operated in a vacuum container so that these effects could be ignored.

3.5   Determination of Detector Dead Layers

A method for determining detector dead-layer thickness is derived which depends on a comparison between the maximum energies of two distributions of charged particles as observed on a multichannel pulse-height analyzer. The results depend on charged-particle, range-energy data and the linearity of the pulse-height analyzer systems, but are independent of the absolute calibration.

From Equation (3.12), the maximum energy observed due to charged particles produced with energy, E_{01}, and passing through a dead layer, d is

$$\bar{E}_1 = (E_{01}{}^{\gamma 1} - d/K_1)^{1/\gamma 1} = C\bar{A}_1, \qquad (3.20)$$

where $\bar{A}_1$ is the maximum analyzer channel in which counts are observed corresponding to particle energy E_1, and C is the system calibration constant. With the same system calibration, charged particles of different initial energy, E_{02}, will have maximum observed energy

$$\bar{E}_2 = (E_{02}{}^{\gamma 2} - d/K_2)^{1/\gamma 2} = C\bar{A}_2 . \qquad (3.21)$$

Eliminating C from Equations (3.20) and (3.21), and solving for d, gives:

$$d = \frac{(K_1\bar{A}_1{}^{\gamma 1})\ (K_2 E_{02}{}^{\gamma 2})\ -\ (K_2\bar{A}_2{}^{\gamma 2})\ (K_1 E_{01}{}^{\gamma 1})}{K_1\bar{A}_1{}^{\gamma}\ -\ K_2\bar{A}_2{}^{\gamma}}$$

$$= \frac{K_2 E_{02}{}^{\gamma 2}\ -\ K_2\bar{A}_2{}^{\gamma 2}/K_1\bar{A}_1{}^{\gamma 1}\ K_1 E_{01}{}^{\gamma 1}}{1\ -\ K_2\bar{A}_2{}^{\gamma 2}\ /\ K_1\bar{A}_1{}^{\gamma 1}} . \qquad (3.22)$$

The terms in (3.22) are observed from any two charged particle sources of known energy, _e.g._, the alpha particle and triton from a simple Li^6-coated detector exposed in a thermal neutron flux, or the alpha particles from known sources such as Pb^{212} or B^{10} in a thermal neutron flux.

Observing two alpha particles of different energies has the advantage that the values of K and γ are the same for both particles, so that Equation (3.22) becomes

$$d = \frac{KE_{02}{}^{\gamma}\ -\ (\bar{A}_2/\bar{A}_1)^{\gamma}\ KE_{01}{}^{\gamma}}{1\ -(\bar{A}_2/\bar{A}_1)^{\gamma}} = \frac{R_{02}\ -\ (\bar{A}_2/\bar{A}_1)^{\gamma}\ R_{01}}{1\ -\ (\bar{A}_2/\bar{A}_1)^{\gamma}}\ -\ a \qquad (3.23)$$

where R_{01} and R_{02} are the ranges of the two alpha particles, and a is the constant given in Equation (3.1).

In the application of this method, the observed maximum channels of the two distributions are taken as the extrapolations of

the upper edges of each peak, thereby eliminating the effect of energy loss due to the straggling in the radiator layer. This method of determining detector dead layer is therefore independent of the radiator thickness.

A useful variation, which will be referred to as the "ratio" method, is derived as follows:

Equation (3.20) is written as a power series

$$\overline{E}_1 = (E_{01}^{\gamma_1} - d/K_1)^{1/\gamma_1} = E_{01} \left[(1 - d/(K_1 E_{01}^{\gamma_1})) \right]^{1/\gamma_1}$$

$$= E_{01} \left[1 - \left(\frac{1}{\gamma_1}\right)\left(\frac{d}{K_1 E_{01}^{\gamma_1}}\right) - \left(\frac{(\gamma_1 - 1)}{2\gamma_1^2}\right)\left(\frac{d}{K_1 E_{01}^{\gamma_1}}\right)^2 \cdots \right]$$

(3.24)

Higher-order terms may be neglected when the dead-layer thickness d is small compared to the range. In applying this method, a similar expression for $\overline{E}_2$ is derived, and values of $\overline{E}_1$ and $\overline{E}_2$ and the ratio $\overline{E}_1 / \overline{E}_2$ are calculated and plotted as a function of d for the particular charged particle sources used for the observation.

To find the value of d, the ratio $A_1/A_2 = CA_1/CA_2 = \overline{E}_1/\overline{E}_2$ is found from the pulse-height analyzer data and compared to the calculated curve.

Curves for residual maximum energy, as given in (3.24) for the alpha particle and triton emitted from Li^6 exposed to thermal neutrons, are shown in Figure 3.5. Curve 1 shows the residual energy of a 2.73-MeV triton as a function of dead-layer thickness of silicon. Curve 2 is the same for a 2.05-MeV alpha particle. Curve 3 is the ratio of the two residual energies as a function of dead-layer thickness.

The ratio method using a Li^6F-coated detector and the method using two alpha particles from Pb^{212} may be used together to determine the thickness of the Li^6F layer and the dead layer. The ratio method will determine the detector dead layer, d, and the two alpha methods will give the sum of Li^6F and detector dead-layer thicknesses. A simple subtraction will yield the Li^6F thickness.

3.6 Li^6 Sandwich

While the principle of operation of the Li^6-sandwich neutron spectrometer can be simply stated, the actual operation is complicated and does not lend itself easily to theoretical analysis. The charged particles involved are of different masses and charges and therefore do not follow the same range-energy relationship. They are produced at random over a range of energies and directions, depending on the incident neutron energy and direction. There are, however, two relatively simple special cases which can be treated theoretically and which give some insight into the general behavior of the device.

31
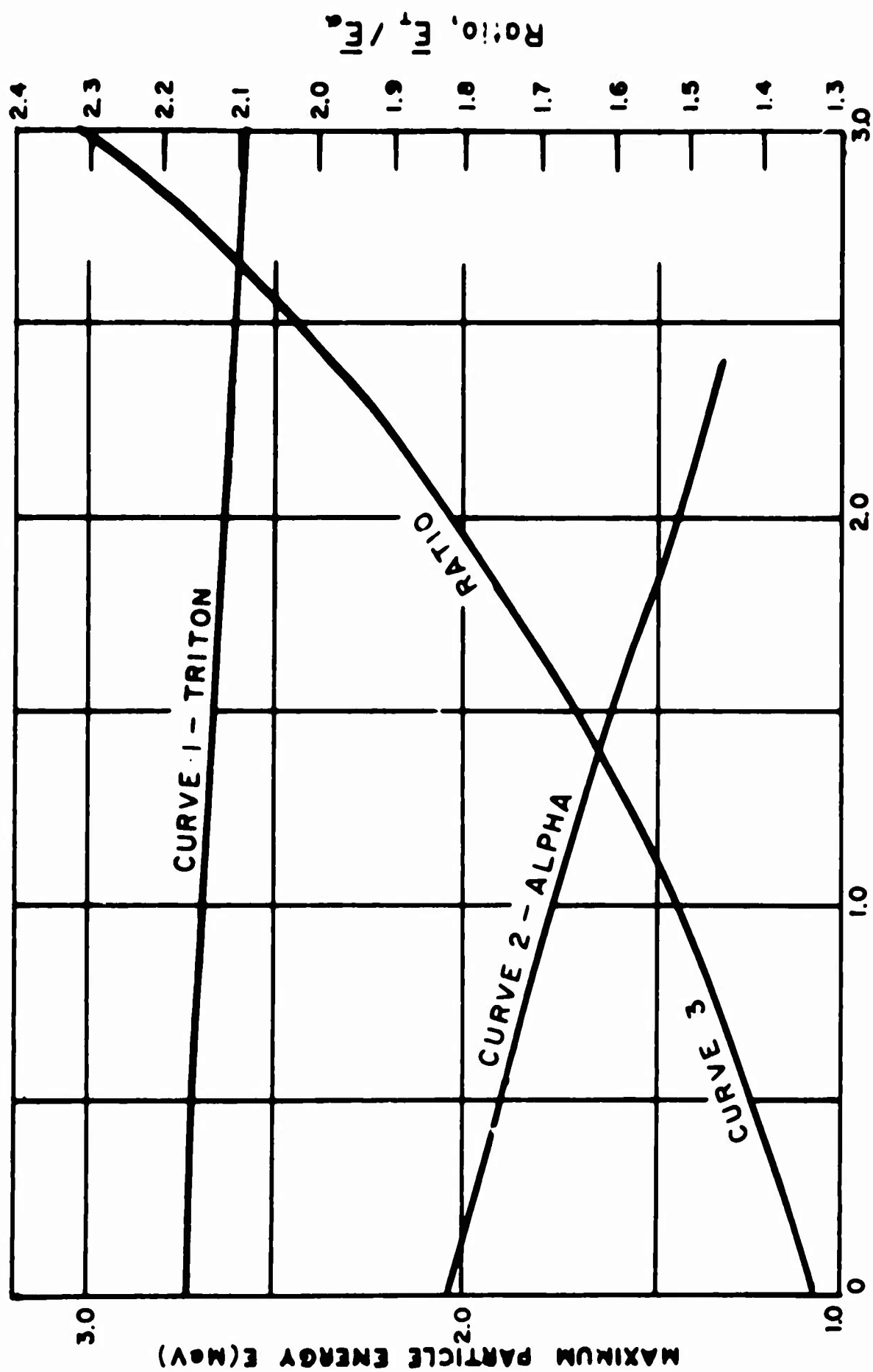
Figure 3.5 Effects of dead layer on particle energy.

32

The first is a calculation of the energy distribution of the sum peak resulting from thermal neutrons. In this case, each charged particle is produced isotropically and at a single energy. The second problem considered is that of estimating counting efficiency as a function of incident neutron energy and detector orientation.

3.6.1 Response of the Li^6 Sandwich to Thermal Neutrons

In the thermal neutron reaction $Li^6(n,\alpha)T$, the alpha particle and triton are emitted isotropically in exactly opposite directions and with fixed energies $E_{0\alpha}$ and E_{0T}. The single charged particle energy distributions observed by either of the two detectors can be calculated directly by the method derived in Section 3.3. An extension of this method can be made to determine the form of the energy distribution of the sum of the energies of the two charged particles as a function of radiator and dead-layer thicknesses.

A plot in the $x\mu$-plane is constructed (Figure 3.6) similar to that of Figure 3.4, except that a second detector dead-layer region is added to the right of the radiator region.

For the first part of the calculation, assume that the alpha particles are observed only in detector #1 and the tritons in detector #2. The second calculation will reverse the roles of the two detectors, and the final result will be the sum of the two calculations.

In the first part, the alpha particle, as seen by detector #1, will satisfy the equation

$$x = K_\alpha \ (E_{0\alpha}^{\ \gamma} - E_\alpha^{\ \gamma}) \ \mu, \qquad (3.25)$$

where the symbols have the same meaning as given in Equation 3.15. Equal energy curves will be straight lines through the point $(0,0)$. A similar relation for triton energy E_T as observed by detector #2 will be

$$(d_1 + d_2 + g - x) = K_T(E_{0T}^{\ \gamma} - E_T) \ \mu. \qquad (3.26)$$

This equation will define a set of equal E_T lines through

$$(d_1 + d_2 + g, \ 0).$$

The method of identifying a point on Figure 3.6 with a particular reaction and the observed sum of particle energies is indicated by the following example. An event occurring at depth x_1, as measured from the depletion surface of detector #1, may emit an alpha particle, in the direction given by μ, into detector #1 with observed energy $E_\alpha = 0.7$ MeV. At the same time, a triton will be emitted in exactly the opposite direction from a depth $d_1+d_2+g - x_1$, and in a direction given by the same μ, and with energy $E_T = 1.2$ MeV, as seen from detector #2. The sum of the two observed events will thus be $E_s = E_\alpha + E_T = 1.9$ MeV.
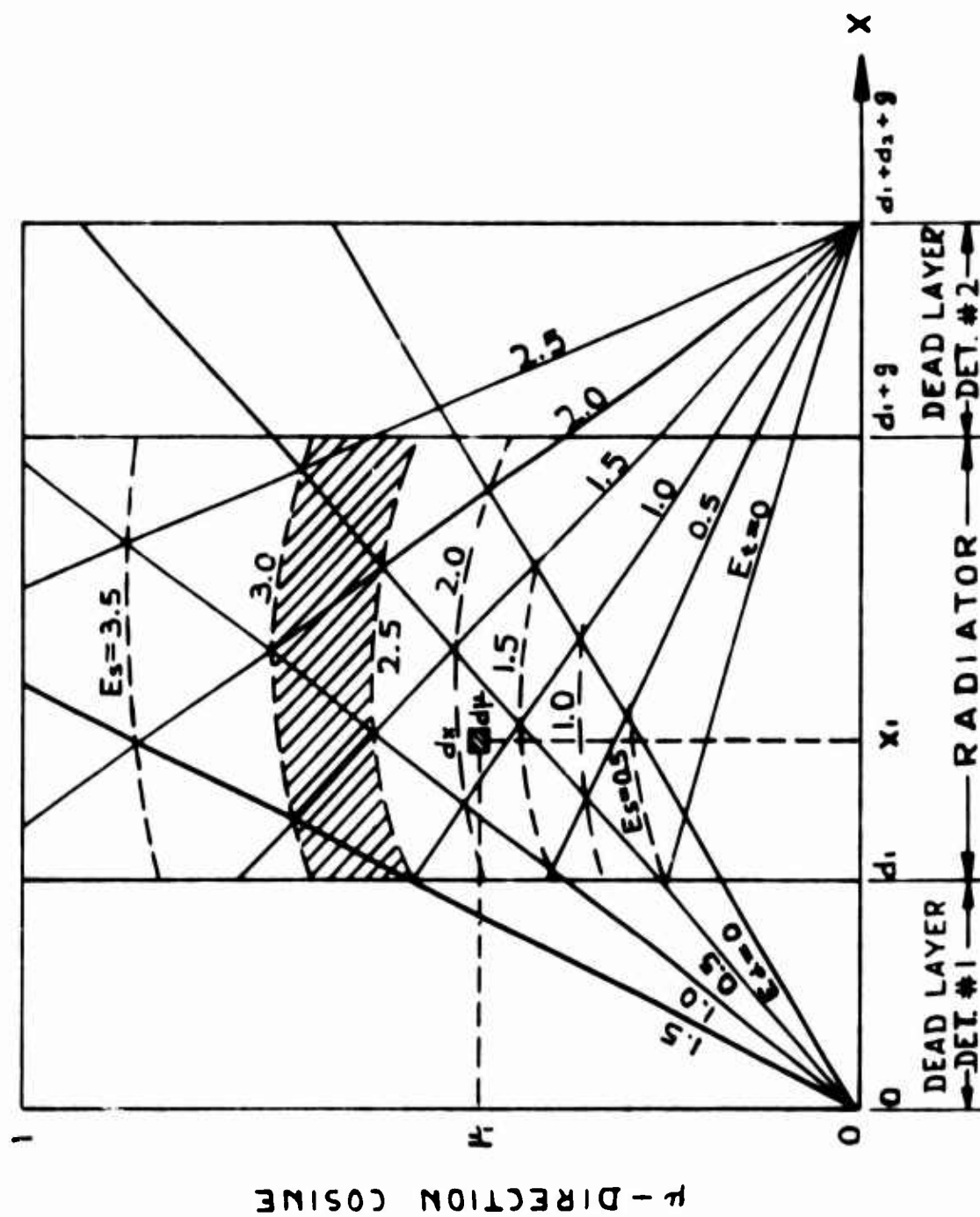
33

Figure 3.6 Graphic Determination of Li^6 Sum Distribution (all energies in MeV)

34

Since the total number of particles observed in a particular energy interval is proportional to the corresponding area on the xμ-plot, the number of events giving sum pulses between any two values of energy will be proportional to the area between the corresponding equal sum energy plots, shown as broken curves, on the xμ-plot. For example, the number of events having observed total energies between 2.5 MeV and 3.0 MeV will be proportional to the shaded area in Figure 3.6. A direct integration between sum curves is difficult; however, the problem may be solved graphically by determining the appropriate area with a planimeter.

This method has been used to calculate the thermal neutron response for dead-layer thicknesses of zero, 0.5 micron, and 1.0 micron, the results of which are shown in Figure 3.7. The increase in dead-layer thickness from zero to 1.0 micron causes a broadening of the sum peak, amounting to a 90 percent increase in the FWHM, a 10 percent loss in peak energy, and a reduction in peak height of greater than 50 percent. A worse deterioration of peak shape occurs when the dead-layer thicknesses of the two detectors are unequal. This is illustrated in Figure 3.8, which shows the double-peaked distribution calculated for the case in which the two detector dead-layer thicknesses were 0.5 micron and 1.14 microns respectively.

These examples point out the critical need for using detectors with very thin and equal dead layers, as well as the desirability of using a thin radiator.

The foregoing method is not applicable in general to fast neutron incidence, since in this case, the resulting charged particles are not monoenergetic and are produced nonisotropically, due to the forward component of momentum in the reactions. However, in the case of fast neutron incidence, some peak broadening would be expected, due to the energy spread of charged particles from the reactions. Furthermore, some shift in the sum peak energy, as a function of detector orientation with respect to the incident fast neutrons, would be expected, due to the forward component of momentum in the reactions.

3.6.2 Effect of Detector Orientation

The thermal neutron reaction with Li^6 results in the isotropic production of charged particles, such that the orientation of the detector is not significant. However, as will be shown, an appreciable difference in counting efficiency as a function of orientation can be anticipated for fast neutron reactions, due to the resultant forward momentum of the charged particles.

If the incident neutron, whose path is parallel to the plane of the detector, reacts with Li^6, the resulting charged particles will each enter a separate detector independent of any forward momentum component, except for the case in which the charged particles are emitted in directions exactly parallel to the detector plane.
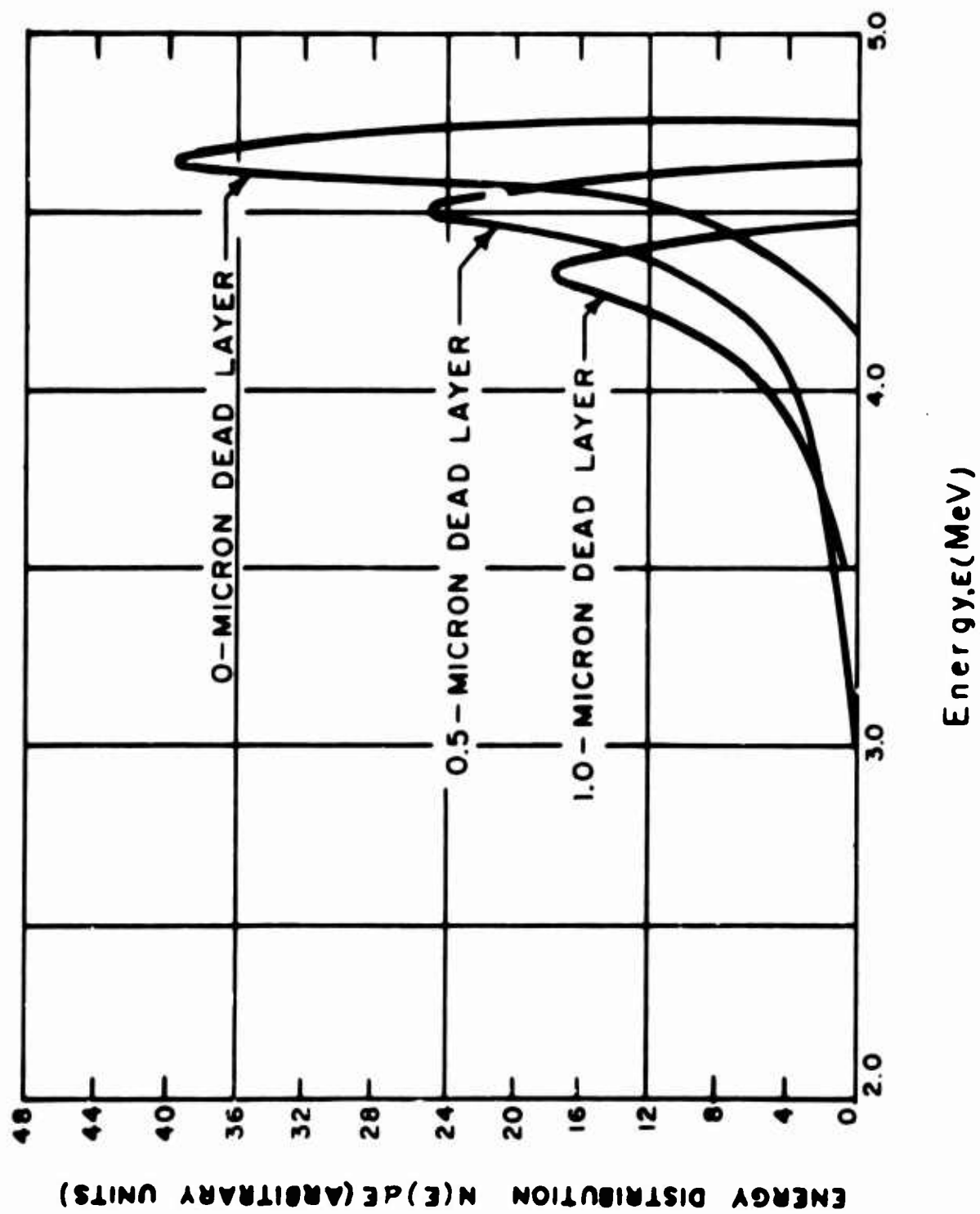
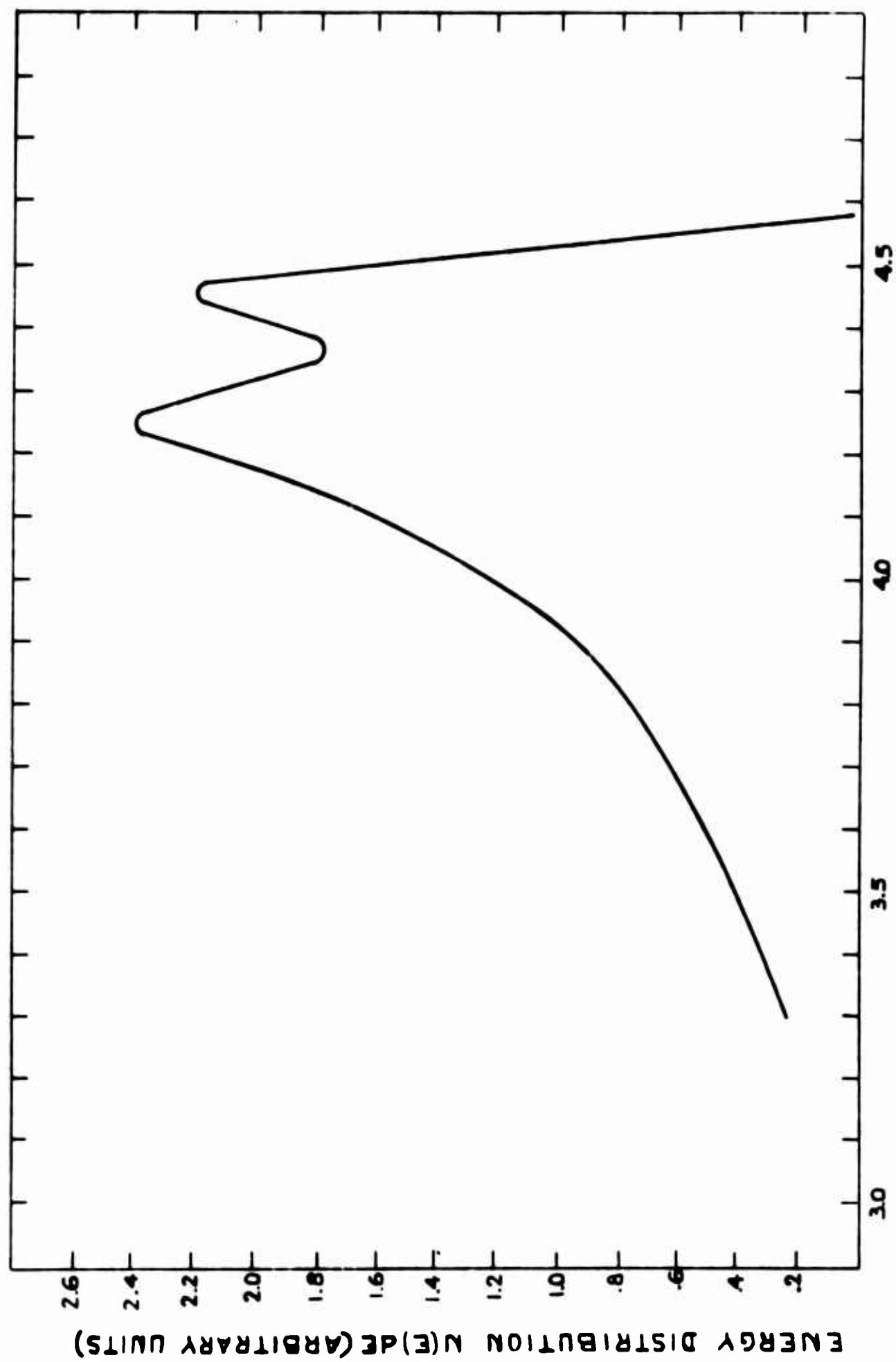Figure 3.7 Li^6 Theoretical sum spectra for thermal neutrons.

Figure 3.8 Li[6] - theoretical sum spectra for unequal dead layers

37

Zero dead layers and radiator thickness are assumed in this case and in the following discussion, so that no slowing down losses will occur. In the case where the incident neutron is normal to the detector surface, it is possible that both charged particles produced in a reaction will have resultant forward velocity components and thus enter the same detector. This event will not be detected and will therefore represent a loss in detection efficiency. In the normal incidence case, the condition under which both charged particles enter the same detector may be described as one in which the angles between each of the paths of the charged particles and the incident neutrons are simultaneously less than $\pi/2$. The fractional loss of counting efficiency will therefore be the probability of this condition being satisfied. Counting efficiency as used here is the ratio of the number of detector sum pulses to the number of $Li^6(n,\alpha)T$ reactions in the system

Figure 3.9 is a velocity vector diagram for the $Li^6(n,\alpha)T$ reactions, in which the primed quantities are those observed in the center-of-mass system and the unprimed terms correspond to the laboratory system of coordinates. Conservation of momentum requires $\underline{V}'_\alpha$ and $\underline{V}'_T$ to be opposite directions. The corresponding velocities in the laboratory system are found by adding the system velocity $\underline{V}_g$ to each of these velocity vectors. The following relationships are noted from the vector diagram:

$$V'_\alpha \sin \theta' = V_\alpha \sin \theta, \qquad (3.27a)$$

$$V'_T \sin \varphi' = V_T \sin \varphi, \qquad (3.27b)$$

$$V'_\alpha \cos \theta' + V_g = V_\alpha \cos \theta, \qquad (3.27c)$$

$$V'_T \cos \varphi' + V_g = V'_T \cos \varphi, \qquad (3.27d)$$

$$\cos \theta' = -\cos \varphi', \qquad (3.27e)$$

$$\sin \theta' = \sin \varphi'. \qquad (3.27f)$$

A typical relationship between θ, φ, and θ' is shown in Figure 3.10. Counting losses occur when θ and φ are simultaneously less than $\pi/2$ or when $\theta'_1 < \theta' < \theta'_2$, where θ_1 and θ_2 are the values of θ' for which φ and θ are equal to $\pi/2$, respectively. Setting $\varphi = \pi/2$ in (3.27d), and using (3.27e) gives

$$\mu'_1 = \cos \theta'_1 = V_g/V'_T \qquad (3.27g)$$

Setting $\theta = \pi/2$ in (3.27c) gives

$$\mu'_2 = \cos \theta'_2 = -V_g/V'_\alpha, \qquad (3.27h)$$
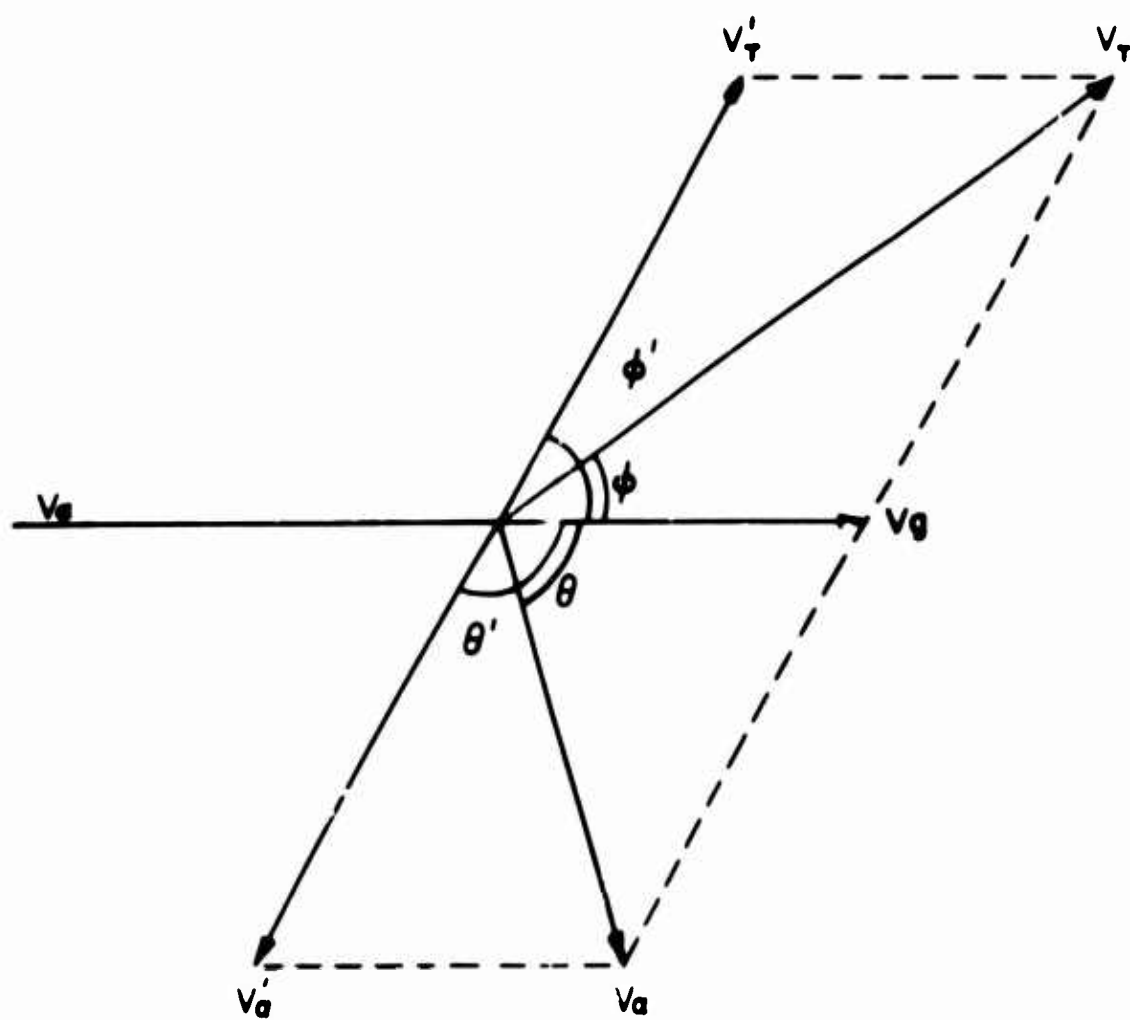
where $\mu = \cos \theta$.

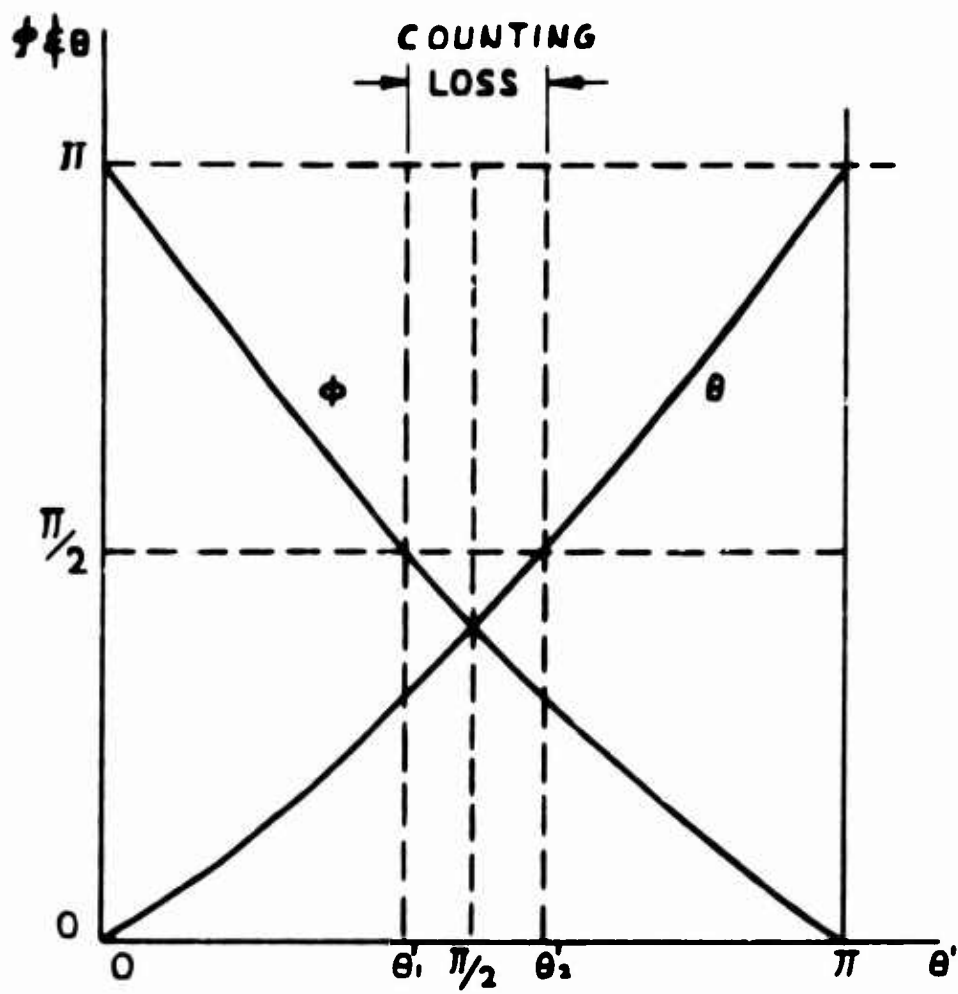Figure 3.9   Velocity vector diagram for the $Li^6(n,\alpha)T$ reaction in the plane of the reaction.

Figure 3.10   Relationship between ϕ, θ, and θ'.

If the reactions are assumed to be isotropic in the center-of-mass system, the probability that an alpha particle will be emitted at some direction μ' in the interval $d\mu'$ is given by (see Equation 3.14)

$$N(\mu') \, d\mu' = \frac{n}{2} \, d\mu'. \tag{3.28}$$

The fractional loss F_L is found by integrating (3.28) over the interval $\theta_1 < \theta_1 < \theta_2$, thus:

$$F_L = \frac{\dfrac{n}{2} \displaystyle\int_{-V_g/V_\alpha'}^{V_g/V_T'} d\mu'}{\dfrac{n}{2} \displaystyle\int_{-1}^{1} d\mu'} = 1/2(V_g/V_T' - V_g/V_\alpha'). \tag{3.29}$$

The velocity of the center of mass in the laboratory system is given by

$$V_g = \frac{M_n}{M_n + M_g} \, V_{n'}, \qquad \cdot \tag{3.30}$$

where V_n = incident neutron velocity, and M_n and M_g are the masses of the neutron and Li^6 atom, respectively. Conservation of momentum in the center-of-mass system requires

$$M_\alpha V_\alpha' = M_T V_T', \tag{3.31}$$

where M_α and M_T are respectively the masses of the alpha particle and triton. Conservation of energy requires

$$(1/2) M_g V_g^2 + (1/2) M_n (V_0 - V_g)^2 + Q = (1/2) M_\alpha V_\alpha'^2 + (1/2) M_T V_T'^2. \tag{3.32}$$

where Q is the reaction energy.

An expression for V_α' is found by substituting V_T' from (3.31) and V_g from (3.30) into (3.22). This expression and the expression for V_T' from (3.31) are substituted into (3.29) to give the final result

$$F_L = (1/2) \sqrt{\frac{M_n (M_\alpha + M_T) E_n}{M_\alpha M_T \left(\dfrac{M_\alpha + M_T - M_n}{M_\alpha + M_T}\right) E_n + Q,}} \tag{3.33a}$$

41

where $E_n = (1/2)M_n V_n^2$ is the energy of the incident neutron. Substituting the numerical values of the masses in (3.33a) gives

$$F_L = (1/2)\frac{7E_n}{12(6/7\ E_n + Q)}\ .\qquad\qquad (3.33b)$$

Representative values of F_L and corresponding counting efficiencies are tabulated below for several values of neutron energy.

Incident Neutron Energy E_n - MeV	Fraction Loss F_L	Efficiency pct
0	.00	100
1	.16	84
2	.21	79
3	.25	75
4	.28	72
10	.33	67
14	.35	65
∞	.41	59

The above values are for the case of normal fast-neutron incidence and are based on the assumption of no loss due to slowing down of charged particles in either the radiator or dead layers. The results show that the counting efficiency of the Li^6-sandwich detector is strongly dependent on orientation.

4. ELECTRONIC REQUIREMENTS FOR NEUTRON MEASUREMENTS

Neutron measurements are intended to measure static, or rapidly varying total flux or energy spectrum. The electronic systems required to perform these functions are composed of a semiconductor detector, amplifier, and readout system. In counting applications, the circuit speed is of primary importance, either for high count rates or for rapidly varying flux measurements. In neutron transient experiments of current interest, the entire observation may extend over 100 μs. In order to observe any time resolution of such an event, the speed requirement of the system is such that all system elements must be designed to the limit of the present technology. For neutron-energy spectrum measurements, the system resolution must be good. This requires a low-noise system which is inherently slower than may be desirable. Requirements of a particular measurement may dictate a compromise between low noise and fast response, or some special circuit techniques such as coincidence-gating for particle discrimination. A system designed specifically for low noise and good resolution is discussed in detail in the section on the Li^6-spectrometer electronic system. Special considerations for fast-counting circuitry are discussed in the following paragraphs.

4.1 Requirements for Fast Counting

There are numerous areas in which high-speed counting is

desirable; for example, during normal start-up, operation, and shut-down of a nuclear reactor, the neutron flux will typically vary over a range of 10 orders of magnitude. With presently available instrumentation, it is common to use three complete sets of instruments to cover this range. In addition to the triplication of instrumentation, the reactor control and safety systems become complicated since they must respond to several, rather than a single, flux-monitoring systems. Due to the fast response of the semiconductor detector, a system incorporating it could be made to operate over a wide range of counting rates, and thereby substantially simplify the over-all reactor instrumentation, which would result in greater reliability and a lower installation cost. A number of laboratories are presently using pulsed neutron sources to study neutron radiation effects. If the duration of the neutron burst is shortened, a very high peak flux may be attained without imposing serious health hazards and excessively activating the equipment. In order to measure adequately the time dependence of such a neutron burst, extremely high-speed counting techniques are necessary.

Counting of discrete nuclear events at high average repetition rates results in information loss due to the random arrival of particles. At the present state of development, the upper limit on counting rates is in the order of 100 Mc/s. To count at this rate with not more than 30 percent loss, using nonparalyzable triggers, a system cycle time (dead time) of 4 ns is required. To maintain satisfactory speed requirements for fast counting, advanced electronic components and techniques must be used. The most promising approach appears to be the use of high-speed trigger circuits whose output is a pulse that is satisfactory for counting at the above rates. The outputs of several types of trigger circuits tested are acceptable for this purpose. These include the high-speed transistor, the tunnel diode, and the avalanche transistor trigger circuit. Also, a trigger circuit based on the secondary emission pentode appears feasible.

Circuit speed requirements are severe for counting at this rate. The output of a typical semiconductor detector is a fast-rising, exponentially decaying pulse which must be modified for fast-counting applications. The most desirable shape is a rectangular pulse. Such a pulse can supply maximum energy per unit time to the load. It will also have a smaller probability of piling up at high average repetition rates. However, the total pulse width should be less than the cycle time of the trigger circuit it drives, to prevent false triggering. To preserve the rectangular shape of the short pulse, the amplifiers must be able to pass a very wide band of frequencies. A system designed for high speed will perform satisfactorily at any lower average counting rate if the pulse shape is maintained.

The output signals from the semiconductor detectors are not, in general, large enough to fire these trigger circuits. Consequently, use of the trigger circuit requires at least some gain between the detector and the trigger unit. For the transistor and avalanche

triggers, the voltage gain required is 10 to 50. In addition, the
tunnel diode requires a current gain of the same magnitude. The
inherent low impedance and small output of the tunnel diode make it
most difficult to use in practical circuits.

Fortunately, the design of high-speed amplifiers having
the required gain is feasible. For example, the Philco 2N769 tran-
sistor having a maximum frequency (f_t) of 900 Mc/s can be used in a
five-stage common emitter-common collector amplifier having an over-
all gain of 32, a passband of approximately 170 Mc/s and a rise time
of approximately 1.7 ns.

The above passband is based on circuit impedances which,
when combined with the parasitic capacitance of the transistors, re-
sult in RC time constants of less th... ns. However, the semicon-
ductor detector impedances are relatively high and the system pass-
band is consequently reduced. By selection of transistor operating
points and design for maximum system speed, it is possible to dr...
sensitive (approximately 10 mV) high-speed triggers (pulse width less
than 10 ns) with the semiconductor detector pulses associated with
charged nuclear particles having a wide range of energies. Indeed,
the only limitation on sensitivity is the system noise.

Optimum operating points for several transistors useful in
the above applications are as follows:

Type	Collector Current I_c - ma	Collector Potential V_c - volts
2N769	5	5
2N700	2	5
2N735	10	15
2N976	7	5

Another element required in measuring systems is the logic
circuit. Logic elements in the nanosecond region require gain to
compensate for parasitic losses. A typical AND gate uses emitter fol-
lowers with a common emitter load. Such a circuit appears to have
rise times dependent only on parasitic elements which can be made rea-
sonably small. The OR gate uses the same circuit configuration and
yields similar performance. Circuits of this type have been tested
with favorable results when the circuit impedances were compatible
with the parasitic elements. Because of the power dissipation of the
above circuits and the critical dependence of speed on the circuitry
geometry, the layout and packaging for these circuits is somewhat dif-
ficult. Speed requirements dictate very dense packing of the components,
especially those directly in the signal path.

At the present time, the speed of counting systems utilizing
the solid-state detectors is limited by the available scaling circuits.
Such circuits are available and are capable of operating at 100 Mc/s.
Preamplifiers operable up to 160 Mc/s have been developed at Solid

State Radiations, Inc. Discriminators operable at 800 Mc/s are available, but their response time is ultimately limited by the need for amplifying the output pulse. In conclusion, one can say that complete systems are operable up to 100 Mc/s. These may be made faster when adequate scaling circuits are available.

4.2 Li^6 Spectrometer - Electronic System

This section contains some comments on the basic operation of the epithermal neutron spectrometer, a discussion of the general requirements of the electronic system, and a comparison of a number of possible systems that have been considered. This is followed by a discussion of the design considerations used in developing the present electronic system and a description of the individual circuits which were involved. The section is concluded by a discussion of operations and calibration procedures.

The basic detector consists of a thin film of Li^6 or Li^6F sandwiched between two semiconductor detectors. Neutrons incident on the Li^6 give rise to the reaction $Li^6(n,\alpha)T$, from which the two resulting particles carry a total energy equal to the sum of the incident neutron energy plus the energy of the reaction. Since the two particles are emitted in roughly opposite directions, generally they will be captured by the two detectors. Each detector will produce a pulse proportional to the energy deposited by the particular incident particle. The sum of the simultaneous pulses from the two detectors will therefore be proportional to the incident neutron energy plus a constant.

The first requirement of the electronic system is that it must add these pulses and amplify the sums to levels which can be observed by a multichannel analyzer. It is desirable to provide enough flexibility in gain and output pulse shape that the system can be used in conjunction with any of the several multichannel analyzers in common use. In addition, the system has to be linear, with low noise and good stability, to indicate the neutron-energy spectrum with good resolution. The system should be capable of operation up to a counting rate of 10^5 counts/s, to fully utilize the capability of most multichannel analyzers.

The pulses from the two detectors resulting from a particular $Li^6(n,\alpha)T$ event occur simultaneously. It is therefore possible to eliminate single pulses from either detector due to noise or single particle reactions by observing only those pulses which occur in coincidence. Accordingly, the second requirement of the electronic system is to gate the signal such that only those pulses which occur in coincidence will be analyzed. The coincidence resolving time should be as short as possible for the system to best accomplish this function.

Electronically, the semiconductor detector may be considered a capacitor onto which a charge is deposited proportional to the energy of the nuclear particle detected. The system response should be independent of variations in detector capacitance or cable capacitance. Therefore, the manner in which the charge is removed from this detector capacitor will critically affect the operation of the system. The system must provide a low-noise sum output whose magnitude is proportional to the energy deposited in the two detectors at any given time, and, in addition, fast-response signals to operate a coincidence gate.

Typically, the physical layout of a neutron facility in which the spectrometer may be used will require remote operation, due to the necessary personnel shielding. Generally, the sensing unit must be small and free of hydrogenous materials or strong neutron absorbers so as to minimize perturbation of the neutron flux being observed. and to minimize activation of the spectrometer elements. It is also desirable to minimize the over-all physical size and power requirement of the system, inasmuch as it can be accomplished without compromise.

4.3 Comparison of Possible Electronic Systems

Basically, two completely different electronic systems were studied in detail. The first consisted of two preamplifiers, one for each detector in the sandwich. Each preamplifier was connected to a mesa or positive side of one detector, essentially as was done when a single detector was used as a charged-particle spectrometer. Each preamplifier provided signals to the summing circuit, as well as to the coincidence and gating circuits. A schematic of this system is shown in Figure 4.1. In the second system, Figure 4.2, the two detector mesas were connected together and a single low-noise preamplifier was used for the sum signal. The fast-coincidence signals were obtained by using low-impedance, common-base amplifiers in series with each detector.

Several variations of the two basic systems were evaluated, with the result that a particular variation of the second system was chosen as the one that would best fulfill the over-all requirements for the spectrometer. Some of the considerations used to evaluate various system components and the arguments for the ultimate choice of the final system are discussed in the following paragraphs.

A configuration which was chosen for evaluation on the basis of its low input capacitance and minimal space and power requirements consisted of dual transistorized preamps located close to the detector. This arrangement was basically unsatisfactory. The best, high-input, impedance transistor-amplifiers had noise-to-signal ratios from 5 to 6 times greater than a comparable vacuum-tube design. This presented a major problem. Also, the requirement of fast response inevitably increased the system noise. The preamplifier in close proximity to the detector may have become radioactive and caused some perturbation in the neutron flux. After continued operation,
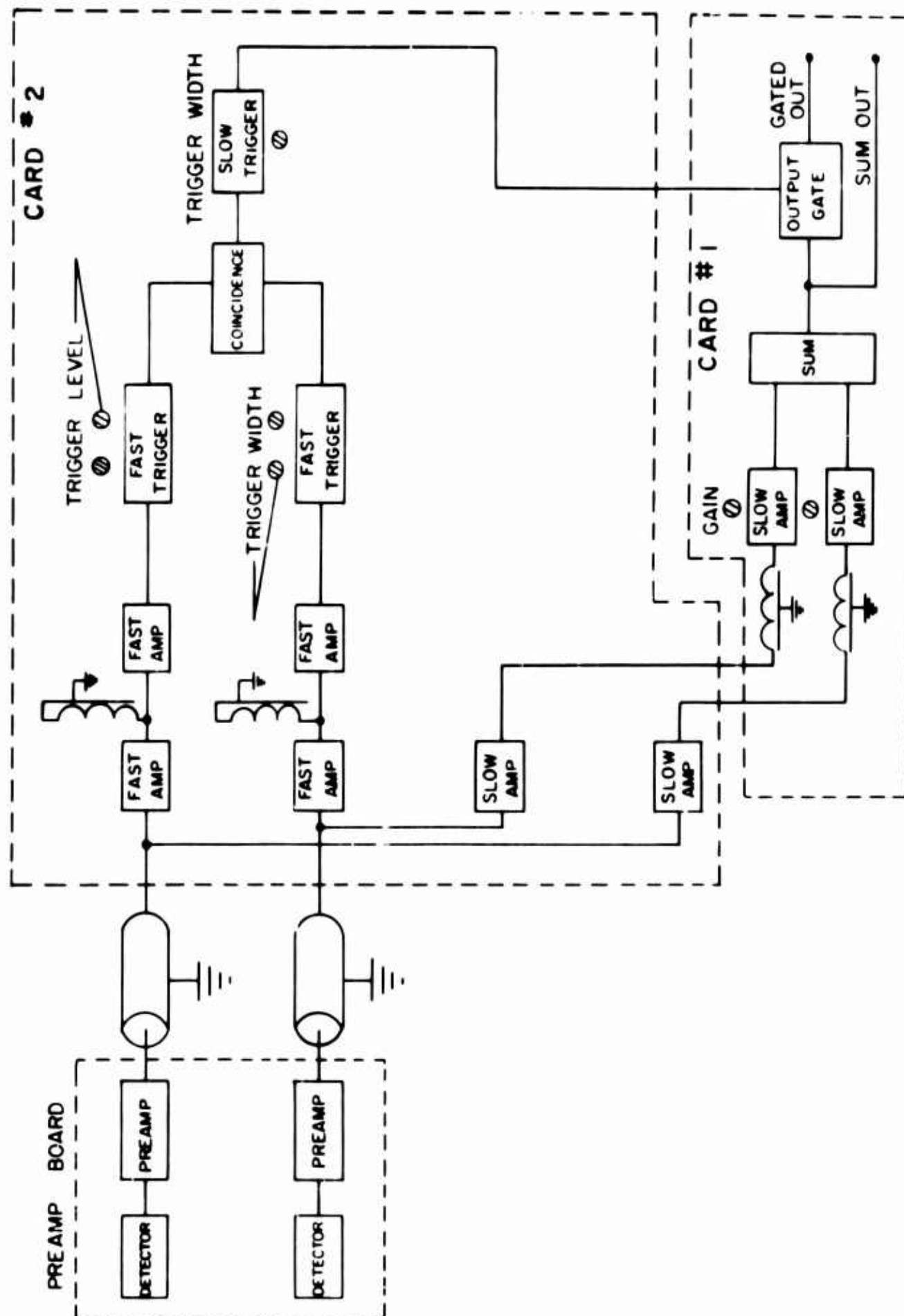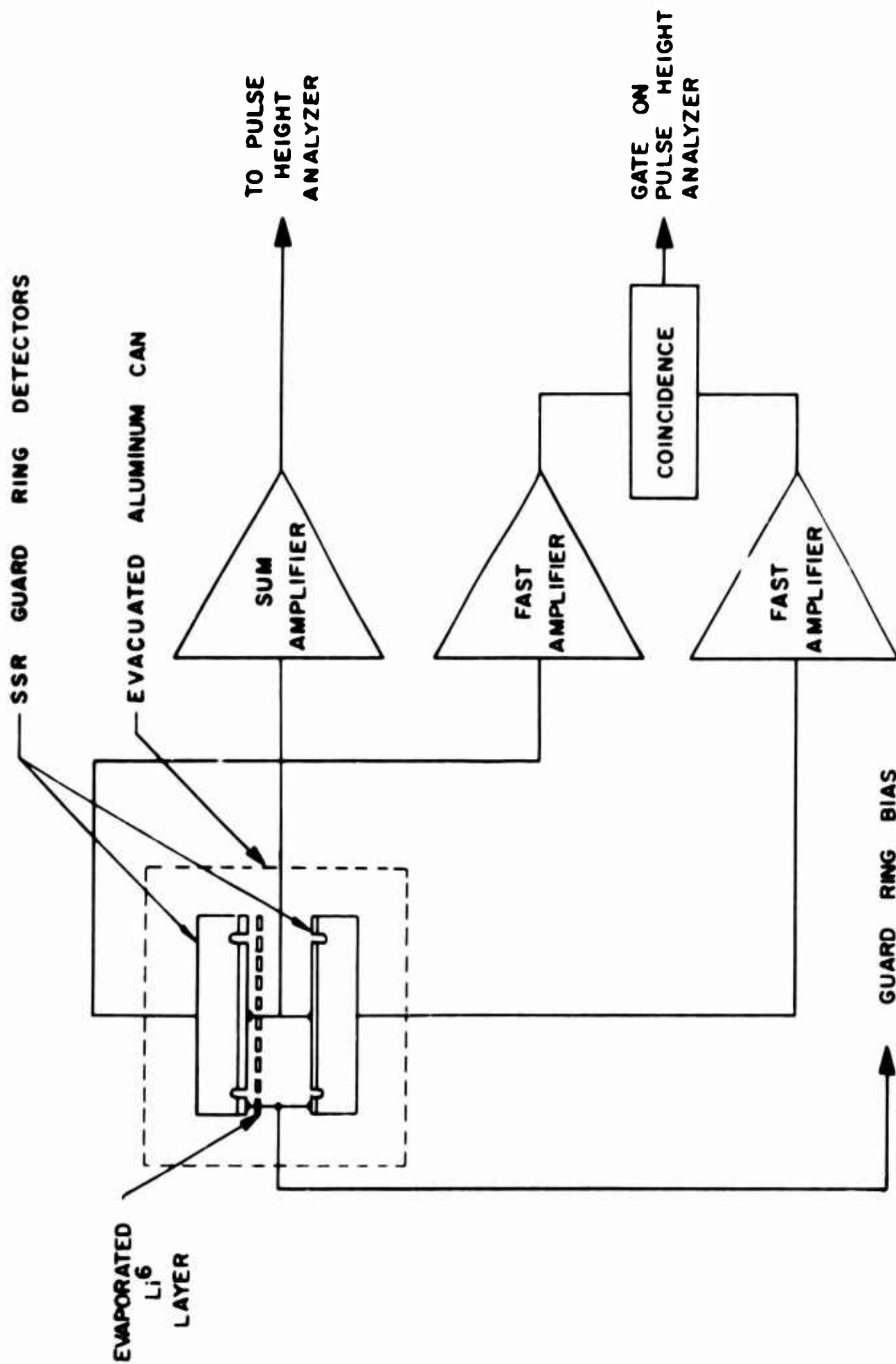
Figure 4.1 Neutron spectrometer system.

47

Figure 4.2 Neutron spectrometer system.

some degradation of a transistor-amplifier would be caused by the radiation fields close to the detector. While the detector would suffer similar radiation damage after exposure to fast neutron doses, 10^{12} or $10^{13}/cm^2$, it could be replaced more readily than the entire preamplifier assembly.

A second possible method of obtaining the necessary signals was to use a vacuum-tube, low-noise, charge amplifier for each detector. Even with only a few feet of input cable to the detector, the noise of this system was lower than that observed with fast-response transistor preamplifiers in close proximity to the detector.

Some of the problems encountered in this second system are listed below:

1. Power - The two vacuum-tube charge amplifiers required B+ voltages of around 250 V at 50 mA and 6.3 V at 1 to 2 A for the filament supply.

2. Space - The power supply and charge preamps required a rack mount, which resulted in reduced portability.

3. Adjustment - The use of two amplifiers to obtain a sum signal required a precise balancing of gain to obtain a good spectrum.

4. Response Time - With low input capacitance, the rise time of the low-noise, vacuum-tube, charge amplifier could be made as fast as 150 ns. However, the addition of the input cable to the detector increased the input capacitance and reduced the bandwidth to the point that the coincidence response time was marginal.

5. Noise - If it is assumed that separate preamplifiers are cable-connected to each of the detectors, the signal-to-noise ratio at the sum output will be

$$\frac{\text{Signal \#1} + \text{Signal \#2}}{\sqrt{(\text{Noise \#1})^2 + (\text{Noise \#2})^2}} = \frac{2}{\sqrt{2}} \cdot \frac{\text{Signal \#1}}{\text{Noise \#1}} = \frac{2}{\sqrt{2}} \frac{S}{N}, \qquad (4.1)$$

where $\frac{S}{N} = \frac{\text{Signal \#1}}{\text{Noise \#1}} = \frac{\text{Signal \#2}}{\text{Noise \#2}}$ is the signal-to-noise ratio of a

single preamplifier-detector arrangement.

This result was obtained because the signals are added algebraically, while the noise is random and follows an RMS addition. This is an improvement over the signal-to-noise ratio of a single amplifier-detector section, but is $\frac{1}{\sqrt{2}}$ times less than that which could be obtained

if the charge of both detectors could be summed at a single amplifier input. In this case,

$$\frac{\text{Signal (Det \#1)} + \text{Signal (Det \#2)}}{\text{Noise (Amp)}} = \frac{2S}{N} , \qquad (4.2)$$

where Signal #1 = Signal #2 = S.

To obtain this result, the detector noise was assumed to be negligible in comparison with other noise sources.

On the basis of this comparison, the system which was chosen for further development consisted of a common input from both detectors to a single-charge amplifier used to provide the sum signal (Figure 4.2). The fast-rising coincidence signals were then obtained by use of low-impedance, common-base amplifiers in series with each detector.

The advantage of this configuration over the dual-charge amplifier system previously mentioned are as follows:

1. Independence of the low-noise charge-sum signal and the fast-rising coincidence signals.

2. Increase in signal to noise due to the use of a single low-noise charge-amplifier to collect the charge from both detectors.

3. Elimination of the charge-amplifier summing circuit.

4. Elimination of need for precise balancing of the two charge-amplifier gains.

The major disadvantage of this circuit was the possibility that one detector could become loaded from the other and thereby lose signal at the charge-amplifier input. An analysis of this circuit showed the loading to be negligible when the capacitance of the charge-amplifier was very large compared to the capacitance of the detectors. The procedure for this analysis is shown in Appendix A.

The major objections to the conventional vacuum-tube charge-amplifier, i.e., space and power requirements, were essentially eliminated by the development of a hybrid charge-amplifier that used two subminiature vacuum tubes and four transistors. With this arrangement it was possible to incorporate the advantages of the low-noise cascode input stage, as well as a low-noise vacuum-tube, first-gain stage, while transistors were used for the less critical circuit functions such as later gain stages and impedance matching. Since the low-noise requirements for the coincidence function were not as stringent, it was possible to use more conventional transistor circuitry for this purpose. The hybrid preamplifier and transistorized coincidence preamplifiers were incorporated into a system that satisfied various other requirements such as physical layout and available output signals.

4.4 Design Considerations

This section discusses the general function of the system and includes some of the detailed considerations used in the design of individual circuit components. The functional arrangement of components is shown in Figure 4.3.

4.4.1 System Operation

System operation begins when a neutron interacts with the Li^6 converter. The resultant alpha and triton particles are absorbed in individual detectors and produce a charge proportional to their initial energies. This charge is summed at the common mesa connection and collected by the charge-amplifier. However, the current $(-dq/dt)$ from each detector is seen by the corresponding coincidence amplifier inputs, and a signal proportional to the particle energy is produced at the output.

The resultant charge sum and coincidence signals were cable-connected from the preamplifier unit to a remotely located control unit. In the control unit, the charge-sum signal underwent additional gain and pulse shaping. Coincidence signals went into discriminators, the outputs of which were diode-clipped to a fixed level, summed, and used to drive the coincidence trigger. Amplitude discrimination should cover a range up to 2 MeV, i.e., the energy of the alpha particles produced by thermal neutrons. The output of the coincidence trigger was used to gate the charge-sum pulse into the multichannel analyzer. Direct operation into a variety of transistorized multichannel analyzers could be obtained by providing a variable sensitivity, plus or minus sum output which was shaped with 1 μs RC-integration and differentiation. For operation into vacuum-tube analyzers, an unshaped negative output with variable sensitivity was provided. This output was applied to a post amplifier to obtain the necessary gain and pulse shape.

4.4.2 Charge-Sum Preamplifier (Hybrid)

A schematic for this vacuum-tube transistor-preamplifier is shown in Figure 4.4. The purpose of this design is to obtain the low-noise characteristic of vacuum-tube circuits while maintaining the compactness and low-power requirements of transistorized circuitry.

The preamplifier required a 45-volt B+ power of less than 0.5 watts, as compared with the typical requirement of 90 watts for conventional hard-tube amplifiers. The subminiature filaments were heated by the same 25-volt supply used for the coincidence preamplifier.

The preamplifier consisted of two basic feedback amplifiers. The input stage provided the charge-sensitive feature, while the second stage was a low-noise voltage feedback stage with an emitter-follower output for cable driving. A test pulse may be introduced through a 2.2 pf series capacitor. The equivalent input charge of the test pulse is $Q_o = (V_{pulse})(C_{test})$.

51
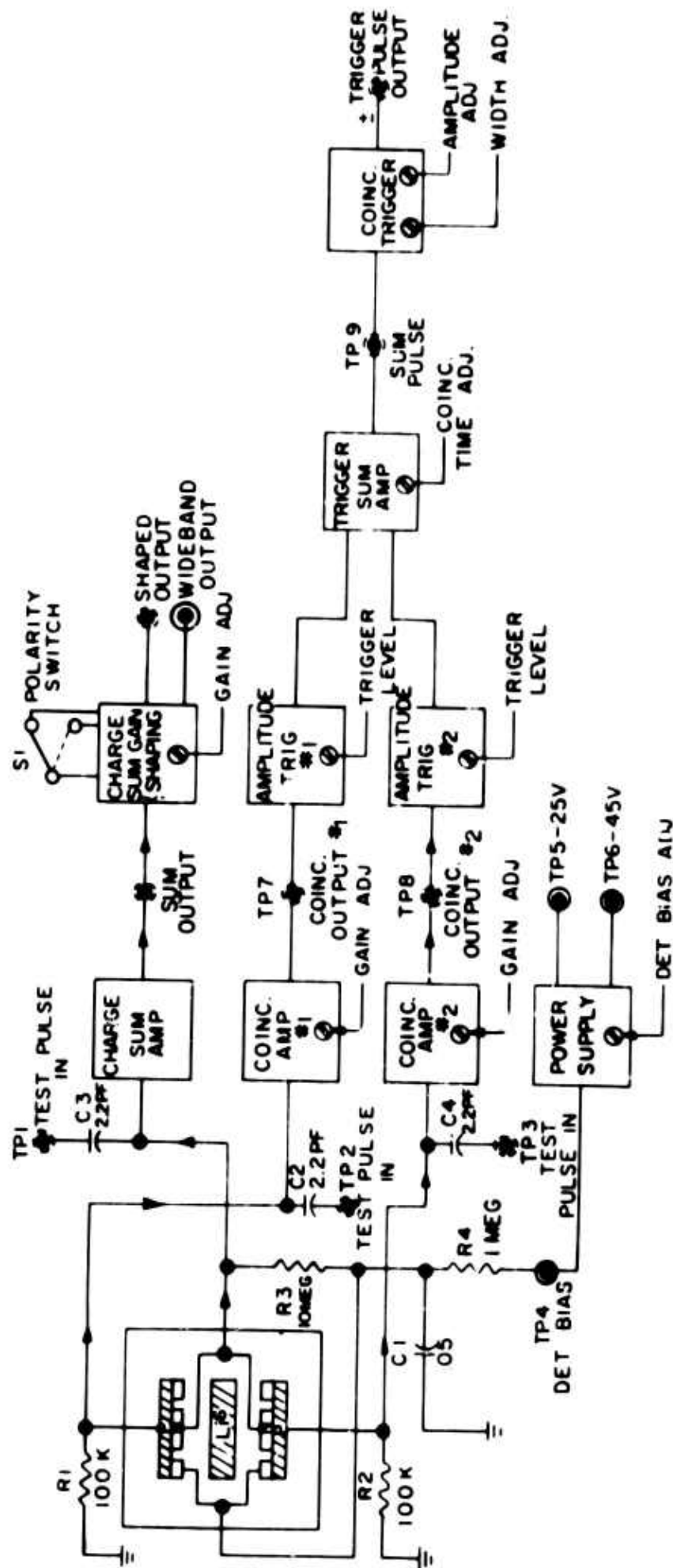
Figure 4.3 System block diagram.
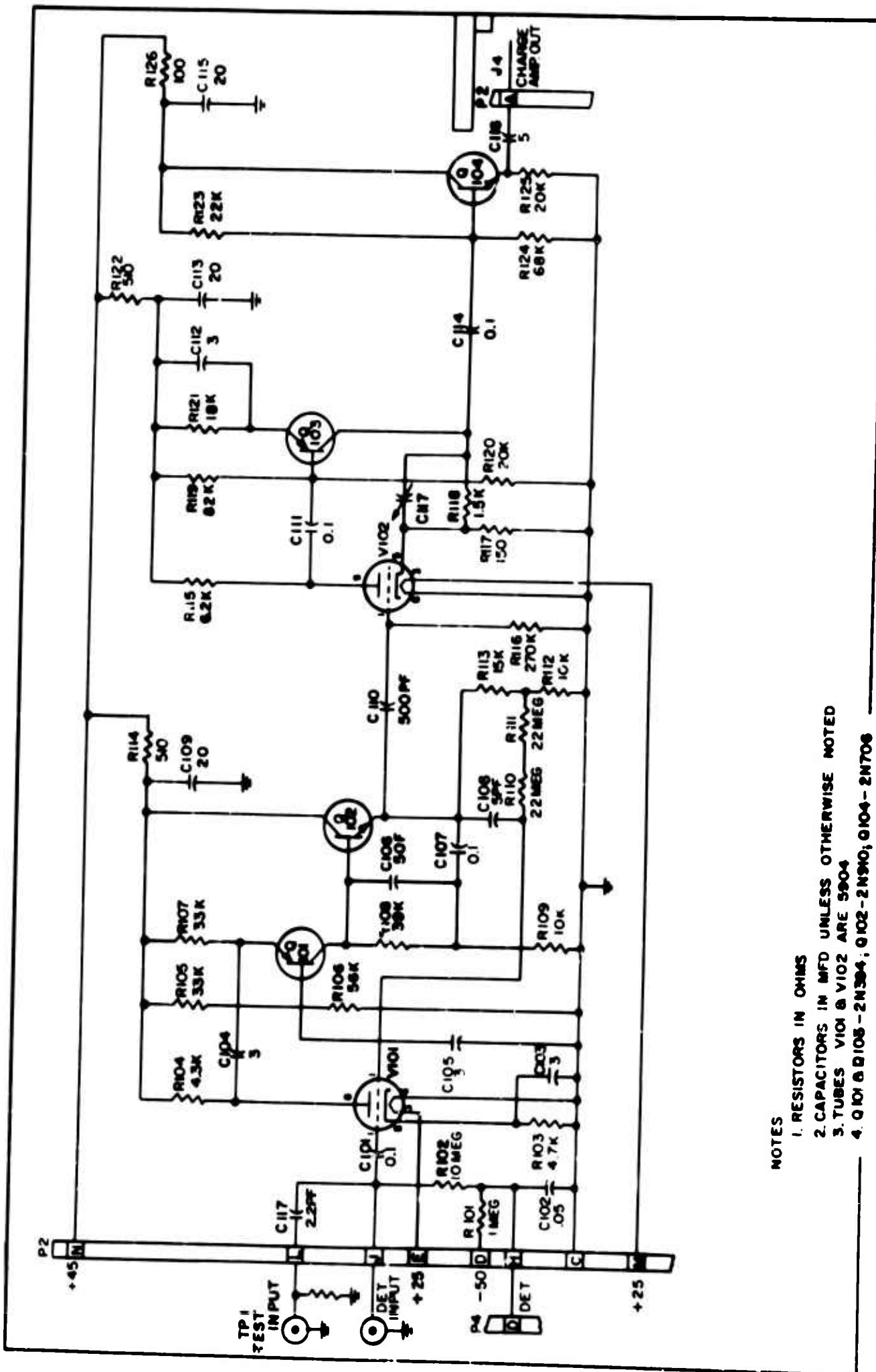
52

Figure 4.4 Hybrid charge amplifier.

53

4.4.3 Input-Tube Considerations

The primary consideration for a low-noise preamplifier is the operating condition of the first tube. The primary noise sources are shot noise and grid current noise. Flicker noise and thermal noise of the input resistors were reduced to insignificant values by use of large resistors and RC time constants shorter than 3 μs. The thermal noise of the plate-load resistor was small as compared with the shot noise, as long as there was a significant voltage gain from the grid to the plate-load resistor. This was always the case with the cascode input. A secondary noise source, which can be neglected, is the induced grid noise.

The equations for shot noise, grid current noise, and total noise in terms of the equivalent mean-squared-charge at the input grid are

$$Q^2_{shot} = \frac{12.5C^2}{G_m\tau} \times 10^{-21}, \tag{4.3}$$

$$Q^2_{(I_g+I_d)} = 4(I_g+I_d)\,\tau \times 10^{-2} \tag{4.4}$$

$$Q_{Noise\ (total)} = \sqrt{Q^2_{(Shot)} + Q^2_{(I_g+I_d)}}, \tag{4.5}$$

where τ = Time constant,

   C = Total cold input capacitance as seen by the grid,

   I_g = Grid leakage current,

   I_d = Detector leakage current,

   G_m = Mutual conductance.

The minimum noise occurs when G_m is large, (I_g+I_d) is small, and τ is adjusted to make the two noise contributions equal. Optimizing these terms for lowest noise results in large values of τ, and the count rate is considerably reduced.

It has been found, by compromising with the ratio

$$\frac{I_g+I_d}{G_m}$$

and τ, that satisfactory signal-to-noise ratios have been obtained with τ = 1 μs. The corresponding operating conditions on the input tube (Sylvania 5904) are G_m = 5,000 μmhos, I_g = 20 X 10^{-4} amperes.

A plot of noise versus time constants (τ) for several values of C is shown in Figure 4.5. The noise is measured as the FWHM of a pulse generator peak on a multichannel analyzer. The relation between FWHM noise and rms noise is 2.414 (rms) = FWHM. This plot shows a minimum at τ = 1 μs for zero detector capacitance. As the equivalent capacitance is increased, the minimum shifts to longer time constants. However, the addition of detector leakage current would tend to keep the minimum of 1 μs. Figure 4.6 shows the same data plotted versus C, with τ held constant.

4.4.4 Charge Loop

The purpose of a charge-amplifier is to provide an output signal that is proportional to the charge input, and that is independent of the input capacitance. This was accomplished by means of a loop consisting of a high-gain amplifier with capacitance feedback. The analysis of such a loop is shown in Appendix B.

The preamplifier charge loop was contained in the input tube V101 and the two transistors Q101 and Q102 (see Figure 4.4). Transistor Q101 was connected in a common base configuration and acted as the top of the input cascode. The emitter-follower, Q102, served as an output stage and drove the capacitor feedback loop containing C108, R110, and R111. This transistor also drove a feedback loop through C107 to bootstrap the load resistor R108. Due to this bootstrapping, the resistor had an apparent value of $R_{app} = \dfrac{R108}{1-A(Q102)}$, which is equal to 390K, where the emitter follower has a gain A = 0.9. The purpose of this configuration was to obtain a high open-loop gain with a minimum phase shift. The calculation of the open-loop gain is given in Appendix B.

The observed charge stability of this circuit, Figure 4.7, was measured to be a 7 percent loss in gain, with a variation in input capacitance of 100 pF. The dc stability of Q101 and Q102 was assured by using stability factors S of less than 2, where $S = 1 + (R_{base}/R_{emitter})$.

4.4.5 Voltage Loop

Due to the low output voltage of the charge loop, it was necessary to use a low-noise input for the first gain stage. The preamplifier voltage loop used a (Sylvania) 5904 vacuum tube (V102) for this purpose. Transistor Q103 completes the voltage loop and Q104 provides an emitter follower output for driving the cable. The 5 μf capacitor (C116) was used to maintain the low-frequency response with a 91-ohm cable. The open-loop gain of V101 and Q103 is the product of the individual gains.

Thus

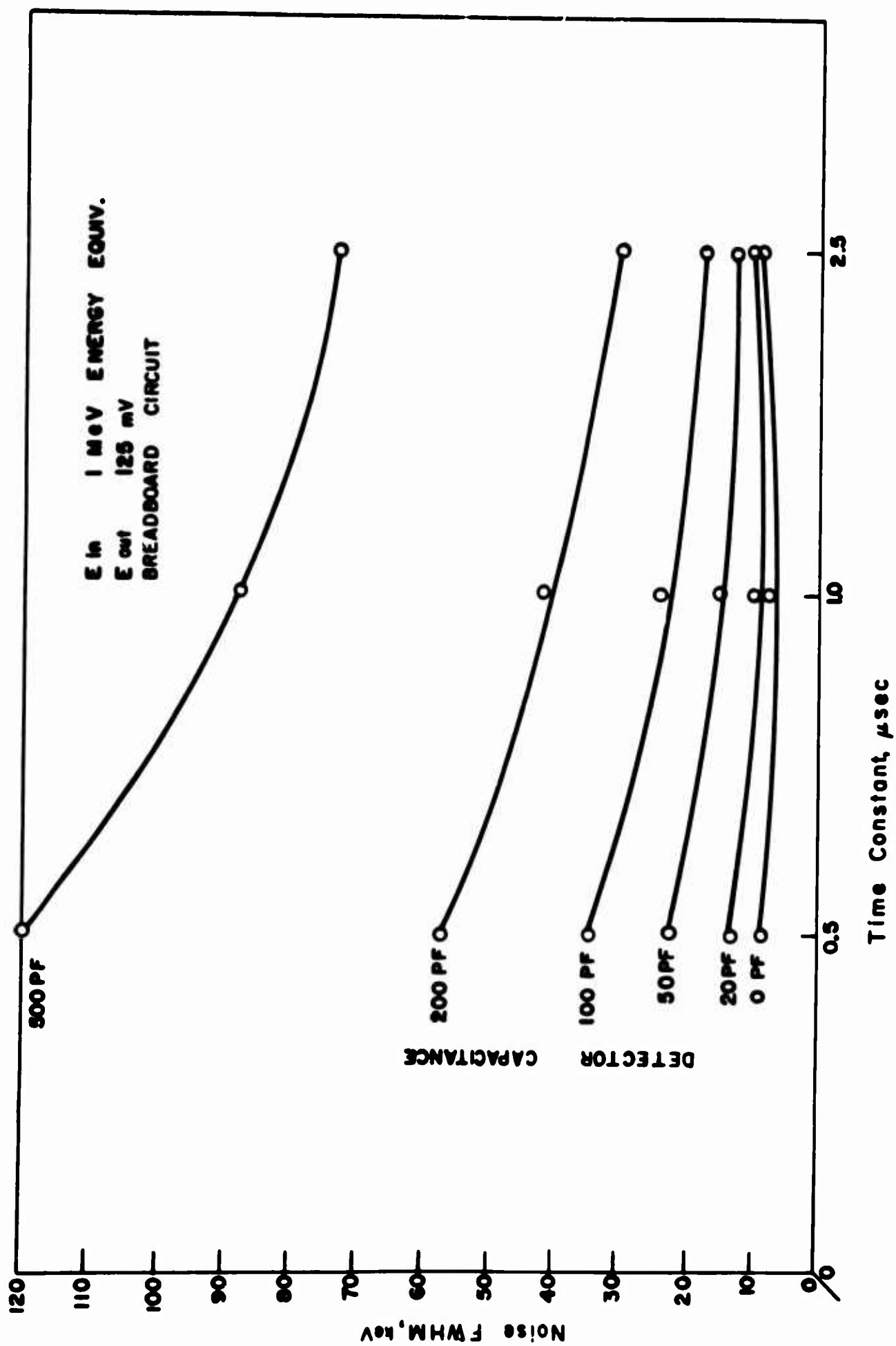$$A_{V102} = \frac{UR_L}{R_L + R_P} \tag{4.6}$$

Figure 4.5 Noise-versus-time constant with capacitance amplifier noise as a function of time constant and input capacitance.
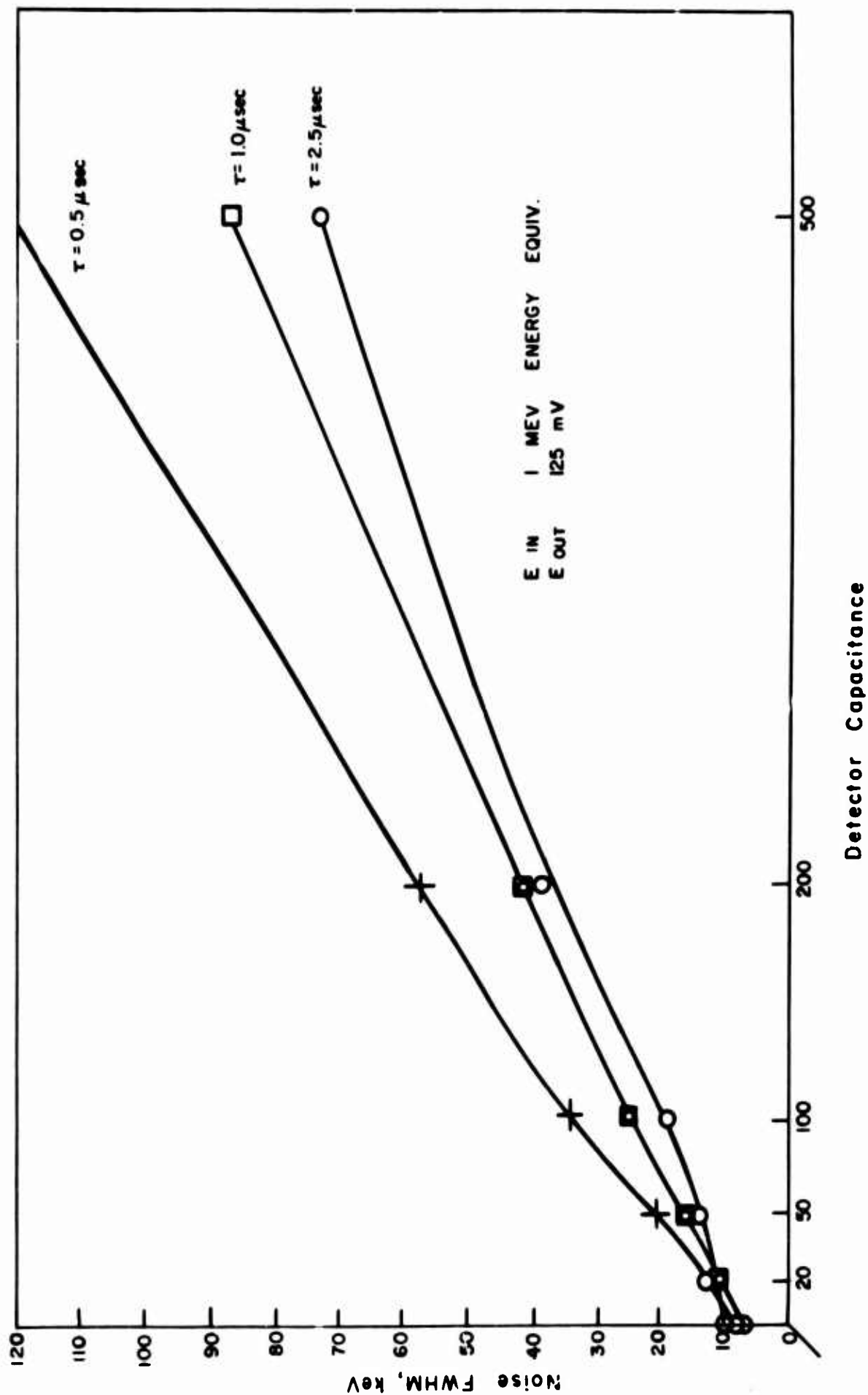
Figure 4.6 Amplifier noise versus detector capacitance and amplifier time constant.
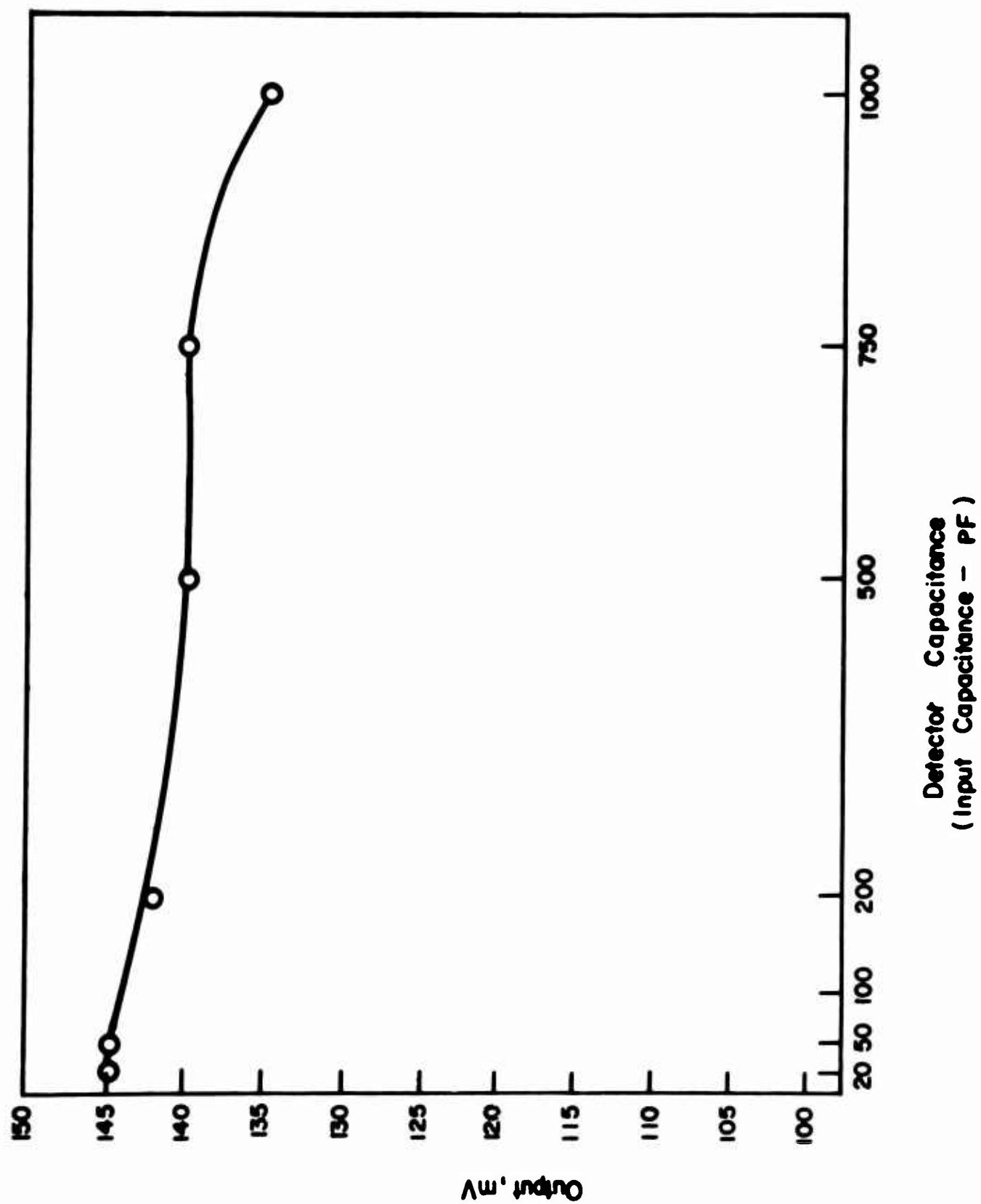
57

Figure 4.7   Charge stability of hybrid preamplifier.

where U = gain of the tube V102 = 20,

K_P = plate resistance $\approx$ 4KΛ,

R_L = parallel impedance of R115 plus the input impedance of Q103, <u>i.e.</u>, $(r_b + \beta_{rc})$ = 1K Λ.

Therefore, the gain of this section is

$$A_{V102} = \frac{(20)(1)}{(5)} = 4. \tag{4.6a}$$

Similarly, the gain of Q103 is

$$A_{Q103} = \frac{R118 + R117}{r_e} = \, \thicksim 130. \tag{4.6b}$$

Therefore, the total gain is

$$\left[A_{(V103)}\right]\left[A_{(Q103)}\right] \; = \approx 500. \tag{4.6c}$$

With feedback, the closed-loop gain is set by R118/R117 = 10, which makes the loop very stable to component variations. The dc stability factors,

$$\frac{\Delta \, I_c}{\Delta \, I_{co}} \; ,$$

for Q103 and Q104 are less than two.

4.4.6 <u>Charge-Sum Gain and Pulse Shaping</u>

This circuit is shown in Figure 4.8. Transistor Q301 is used to provide additional gain for the charge-sum signal. The sensitivity of this signal is changed by control of the 10 to 1 attenuator (R323 and R306) at the Q301 input. The emitter follower Q302 drives the unclipped output and the RC pulse-shaping network (C307, R313, R314, and C309). In this network, (C307)(R313) = (R314)(C309) = 1 μs. To prevent loading, the resistance of R313 is less than R314 and the capacitance C307 is greater than C309. Transistor Q303 is an inverter to provide plus or minus outputs. The emitter follower Q304 provides a low-impedance output to drive the multichannel analyzer.

4.4.7 <u>Coincidence Preamplifier</u>

The coincidence preamplifiers use a common-base input stage, four common emitter gain stages, and an emitter follower output stage. The identical preamplifiers for channels 1 and 2 are constructed on a printed circuit card. The circuit schematic is shown in Figure 4.9.
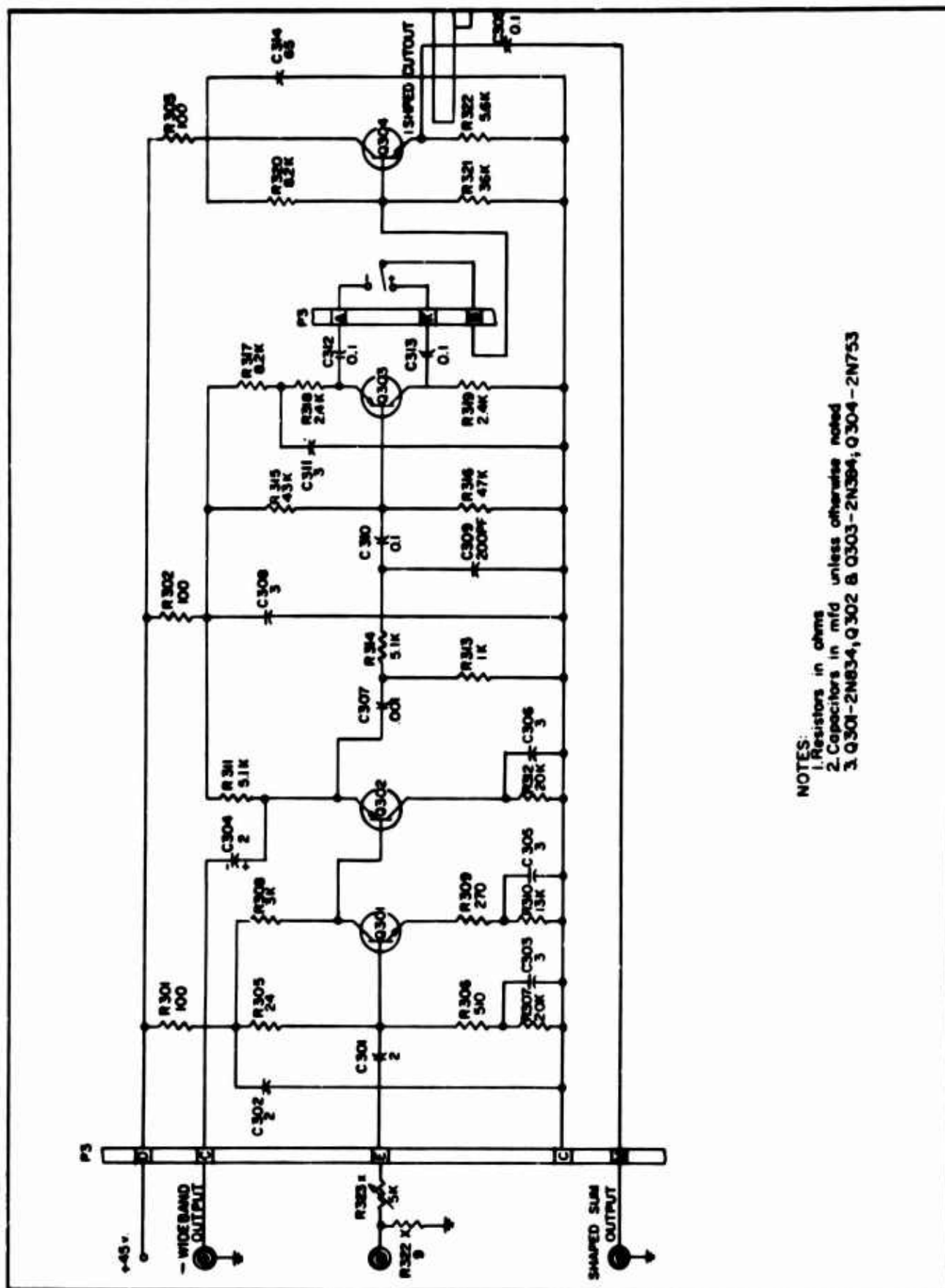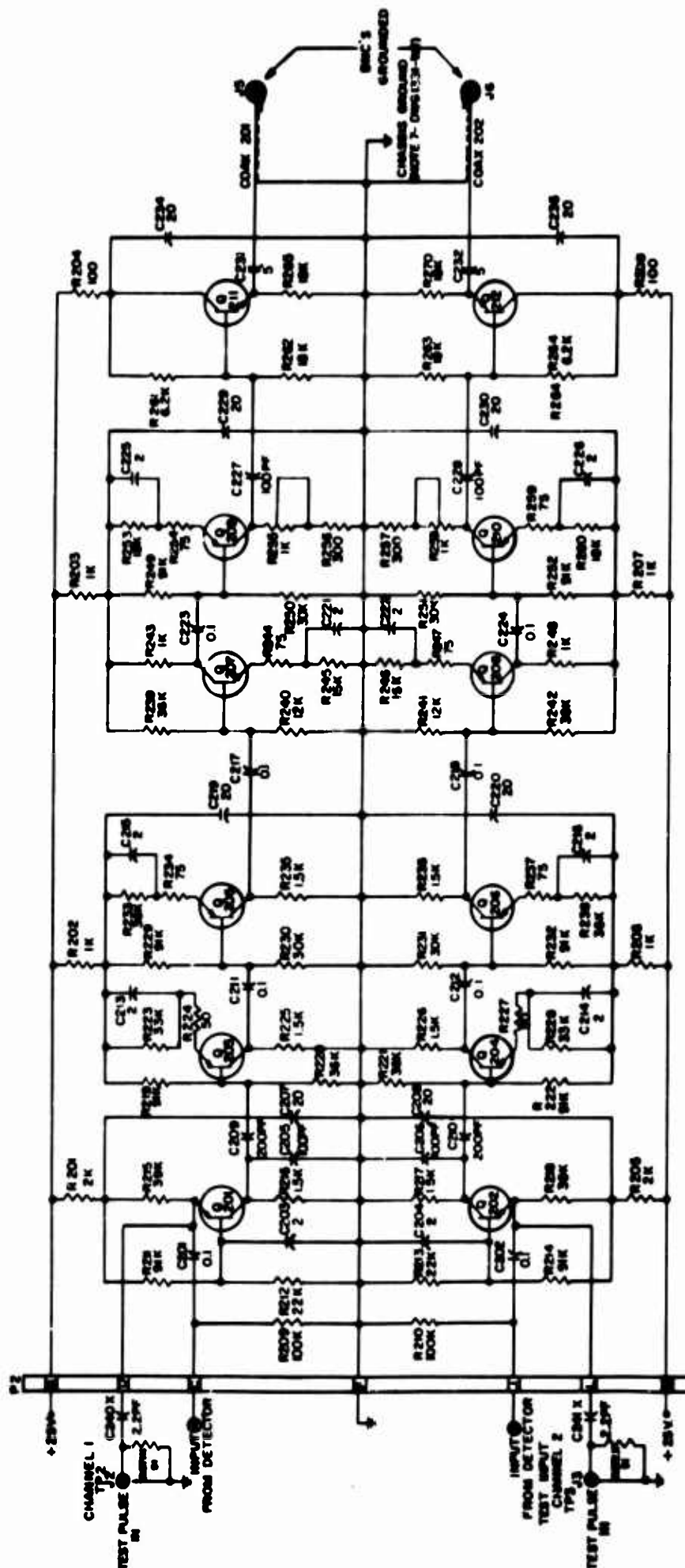
59

Figure 4.8 Charge sum gain and pulse shaping.

Figure 4.10 Amplitude trigger and trigger summing circuit.

61

The input stage is biased so the input impedance is approximately 50 Λ. This is done to provide a termination for the detector cable and to keep the series impedance small, as compared with the detector series resistance. The preamplifier rise time and fall time are controlled by the detector time constants and the time constant of the collector load of the input. In the discussion of the detector-preamplifier input (Appendix A) it is shown that the current pulse through the common base input is $Q_0/RC\ e^{-t/RC}$. Transferring this input to the equivalent RC load impedance of the input transistor by the common-base current gain (α) results in a voltage at the collector of

$$e_o = \frac{Q}{C_L} \left(\frac{R_L C_L}{R_L C_L - R_D C_D} \right) \left(e^{-t/R_L C_L} - e^{-t/R_D C_D} \right). \qquad (4.7)$$

This result is developed in Appendix C. The expression shows that the output rise time and fall time are controlled by the detector and input stage-time constants, and the output magnitude is a function of the charge (Q) deposited on the detector. If $R_L C_L = 2R_D C_D$, the output is approximately 0.25 mV/MeV. For the circuit values, this signal rises in about 100 ns and decays in about 250 ns. The 100-ns rise time and 0.25 mV/MeV set the gain and bandwidth requirements for the common emitter-gain stages. The gain must be sufficient to drive the amplitude trigger, and the bandwidth of the amplifier must be large enough to maintain the input rise time. Expressions for gain and bandwidth are also given in Appendix C. Due to the system requirement for a wide range of energy discrimination, the amplifier gain is made adjustable by F255 to reduce the threshold variations on the amplitude trigger. The operating point stability of the amplifier is ensured by dc stability factors

$$\left(S = \frac{\Delta\ I_c}{\Delta\ I_{co}} \right) \qquad (4.8)$$

of less than 2.5.

4.4.8 Amplitude Trigger and Trigger Sum Circuit

This circuit is shown in Figure 4.10. In this circuit stages Q401, Q403, and the diode CR402 provide one trigger and Q402, Q404, and the diode CR403 provide the other. The stages Q405 and Q406 provide the sum element and Q407 is a sum gain stage. The sum output is coupled to the coincidence gate by the emitter-follower Q408.

Since both trigger circuits are identical, only the amplitude trigger containing Q402, Q404, and CR403 is discussed. This trigger stage, Q402, is biased on and Q404 is reverse biased in the quiescent state. When a positive input signal is applied to Q402, the current is reduced and the voltage at its collector goes toward ground. The negative voltage change is coupled to the base of Q404 and causes the current to increase. If this negative swing is
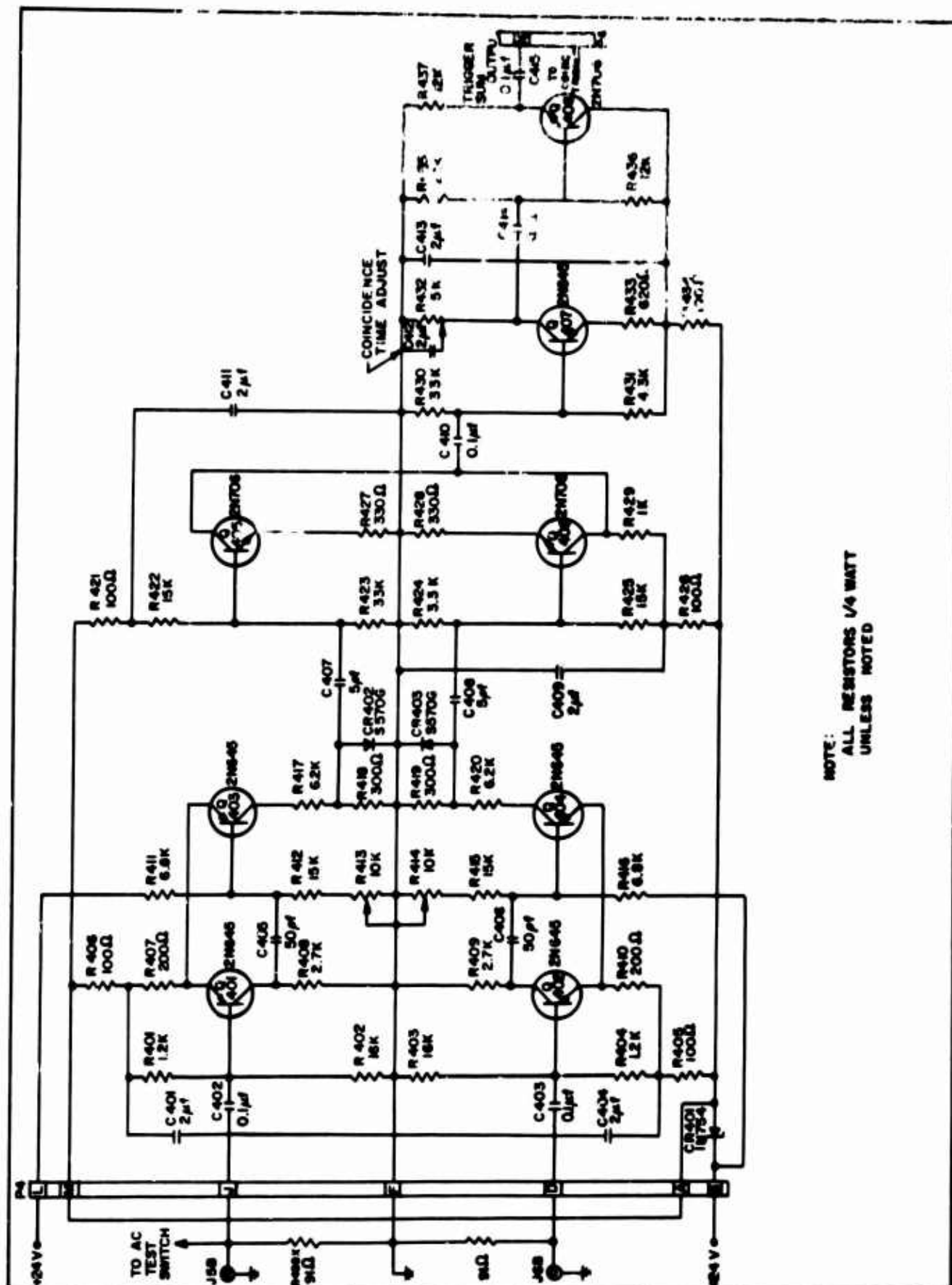
62

Figure 4.9 Coincidence preamplifier

63

larger than the reverse bias of Q404, an increase in current occurs.
This increased current flows through the common emitter-resistor
R410, and the emitter-to-ground voltage of Q402 is reduced. This
reduces the current through Q402 further, and the loop is regenera-
tive until Q404 is saturated. At this time, essentially all the
supply voltage is across CR403 and R420. The coupling capacitor
C406 then charges to the new base voltage of Q404 with a time con-
stant determined primarily by R409 and C406. This charging current
flows through the emitter-resistor R410 and holds Q402 off until the
current decays to the point where the emitter voltage of Q402 ap-
proaches its base voltage. When Q402 is forward-biased, current
flows through its collector resistor, and a positive voltage change
is produced. This voltage change is coupled to Q404, which initiates
cutoff. The cycle is completed when Q402 is on and Q404 is off.

Amplitude discrimination is controlled by adjustment
of the reverse bias voltage on Q404. This adjustment is made by
using the 10 Kₙ potentiometer R414 to control the base voltage operat-
ing point.

The trigger output is taken across the silicon
diode, CR 403. The magnitude of this signal is set by the forward-
biased voltage level of the silicon diode and is independent of the
input signal magnitude. The rise time of this diode voltage is
very fast, since it is a small portion of the total collector swing.

4.4.9 Coincidence-Sum Amplifier

The trigger outputs are differentiated by C408 and
R424 to obtain fast-rising, narrow pulses. These outputs are then
used to drive the common emitter stages Q405 and Q406. The use of a
single collector resistor for both stages provides an output signal
which is proportional to the sum of the trigger outputs. This sum
is amplified by the common emitter stage Q407, and the 5 K poten-
tiometer R432 is used to control the sum amplitude which determines
the coincidence time.

The operation of the coincidence circuit is illus-
trated in Figures 4.11 and 4.12. In the first figure, the two trig-
ger pulses arrive in exact coincidence and the peak value of their
sum exceeds the coincidence threshold. The coincidence trigger is
fired, which results in the output gate pulse. By contrast, in Figure
4.12 the two trigger pulses, of the same shape and amplitude as in
the previous case, arrive at slightly different times. The sum is a
broad pulse having a peak value less than the coincidence threshold,
after which no further action takes place. The gain of the coinci-
dence amplifier is adjusted so that the coincidence-sum value of
both discriminator outputs just exceeds the threshold level required
to fire the coincidence trigger. This condition represents the
minimum allowable time separation between the alpha-particle and tri-
ton pulses. The threshold level is then decreased by an amount neces-
sary to account for the time jitter of the system, i.e., the width of
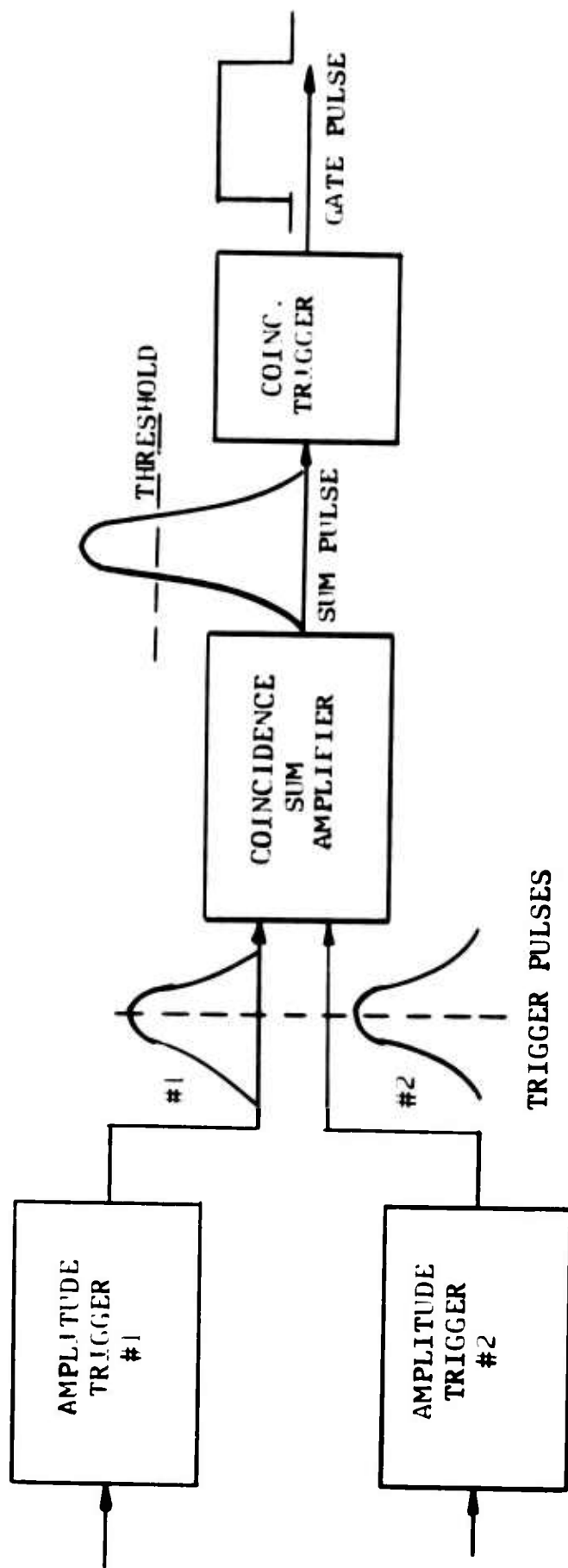the coincidence gate pulse.

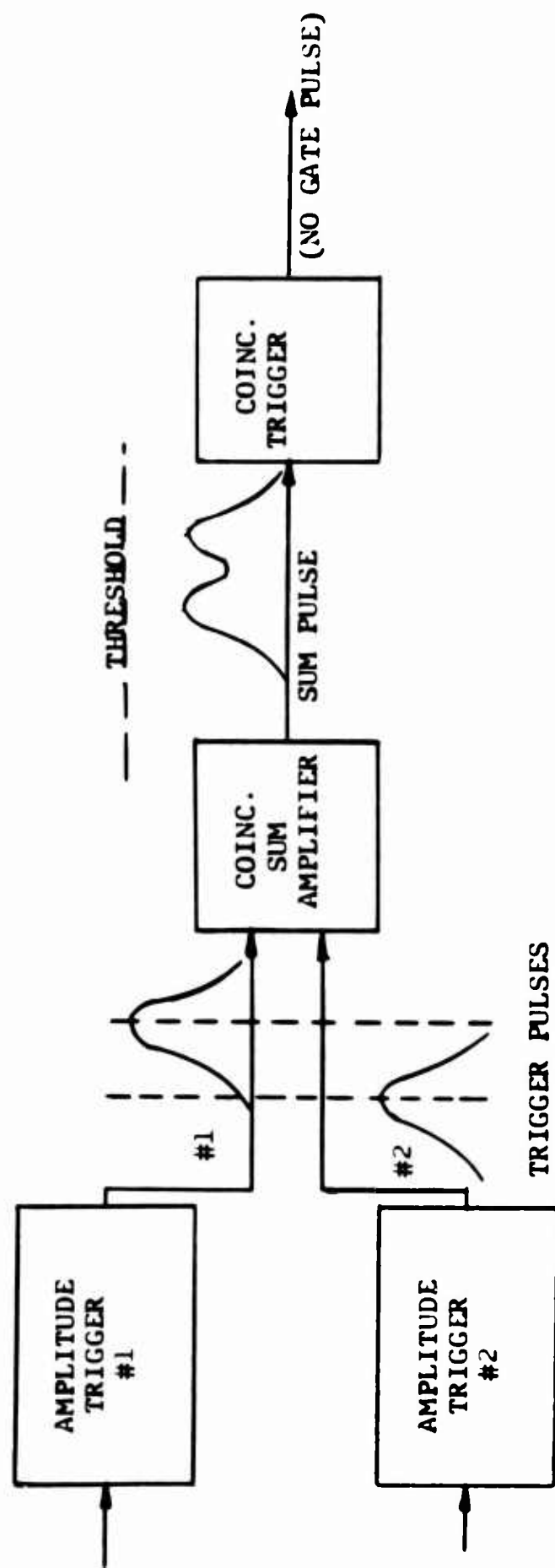Figure 4.11 Coincidence System (Input trigger pulses in coincidence).

65

Figure 4.12 Coincidence System (Input trigger pulses not in coincidence).

4.4.10 Coincidence Trigger

This circuit is shown in Figure 4.13. Transistors Q501 and Q502 provide the emitter-coupled trigger element. Transistors Q503 and Q504 provide the positive polarity coincidence-trigger pulse, and transistors Q505, Q506, and Q507 provide the negative output. The variable capacitor, C502, provides a pulse-width adjustment from 2 μs to 5 μs. The potentiometer, R524, provides amplitude adjustment from 5 to 15 V. Operation of the trigger circuit will not be discussed because it is identical to that of the amplitude trigger circuit. The only exception is a fixed threshold level on transistor Q502.

4.4.11 Power Supplies

The power supply schematic is shown in Figure 4.14. There are three basic power supplies for the system: the +45-volt and +25-volt, and a detector-bias supply which varies from 0 to 100 V. The +45 and +25-volt supplies are full-wave rectifiers, with RC filters and a difference amplifier that compares a Zener reference with an output sample from a voltage divider. The voltage divider is variable and allows small adjustments of the power voltage around the nominal value. The Zener reference is bypassed by capacitors to reduce the Zener noise. The detector bias supply uses a shunt Zener regulator because the maximum current required is 1 mA. The supply voltage is controlled by the potentiometer across the Zener.

4.4.12 Wiring Diagrams

Wiring diagrams for the control cabinet, preamplifier cabinet, power cabinet, and the detector cables are shown in Figures 4.15, 4.16, and 4.17, respectively. The printed circuit card holders are numbered P_1, P_2, through P_x. This numbering system corresponds to the circuit card numbers 1331-1, 1331-2, through 1331-x. For example, the receptacle P_1 on the preamplifier wiring diagram is used with the charge preamplifier 1331-1A.

4.5 Physical Layout of the System

The system consists of the following cable-connected units containing the elements as indicated below:

1. Hermetically sealed solid-state detector and its connector.

2. Preamplifier unit.
   a. Charge-sum amplifier
   b. Coincidence amplifier No. 1
   c. Coincidence amplifier No. 2
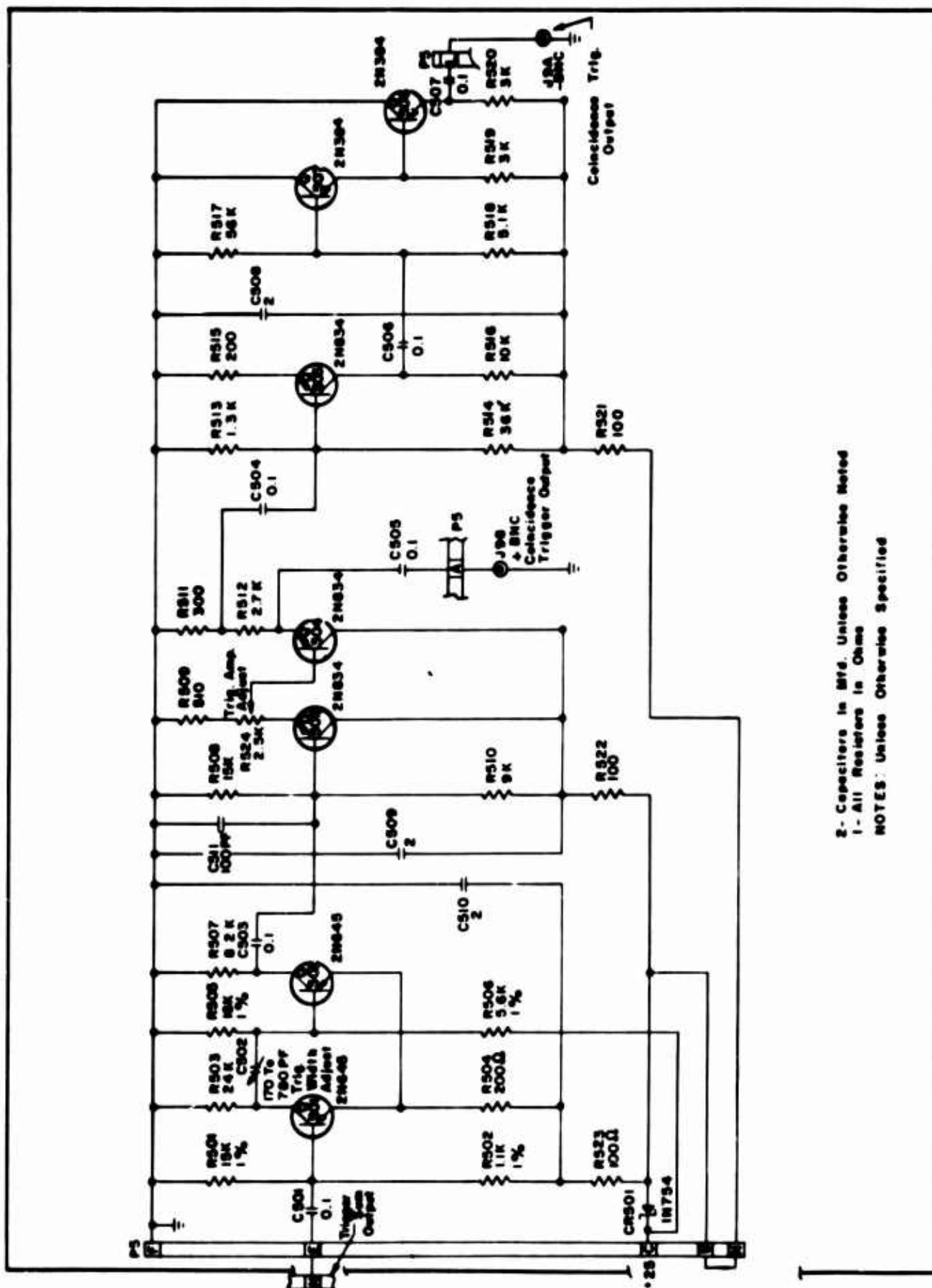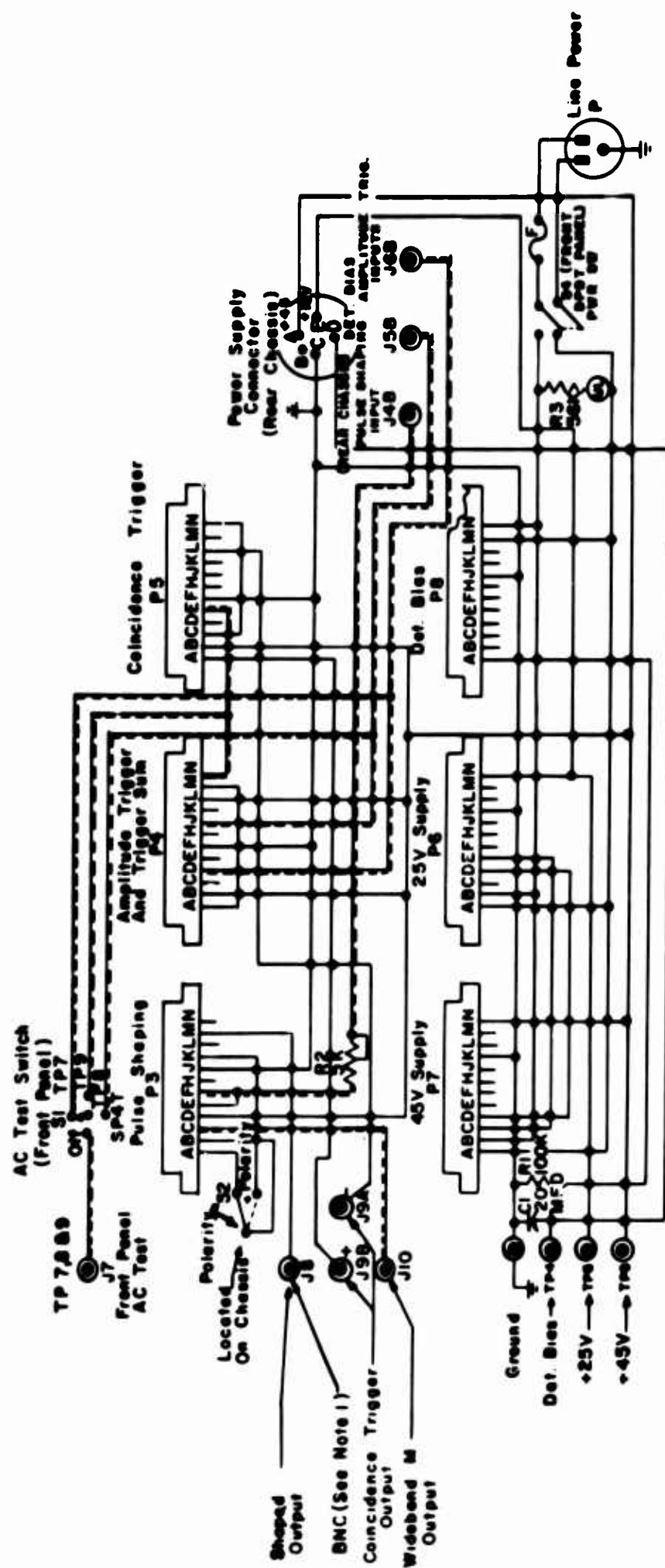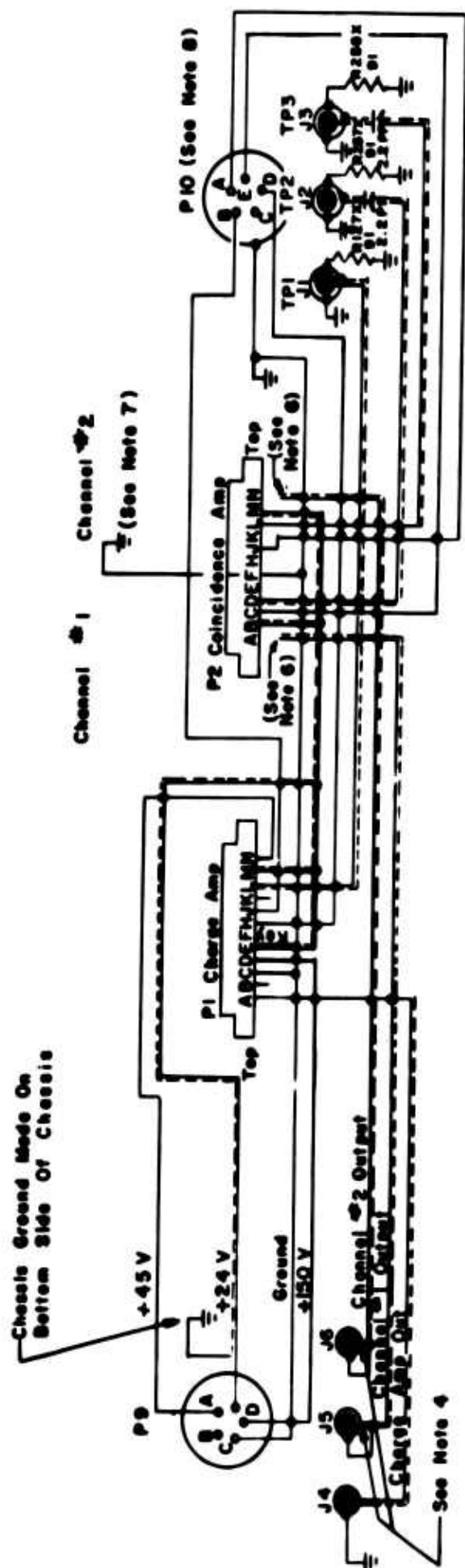
Figure 4.13 Coincidence trigger.

68

Figure 4.14 Power supply.

69

Figure 4.15 Wiring diagram for control cabinet.

70

Figure 4.16 Wiring diagram for preamplifier cabinet.

71
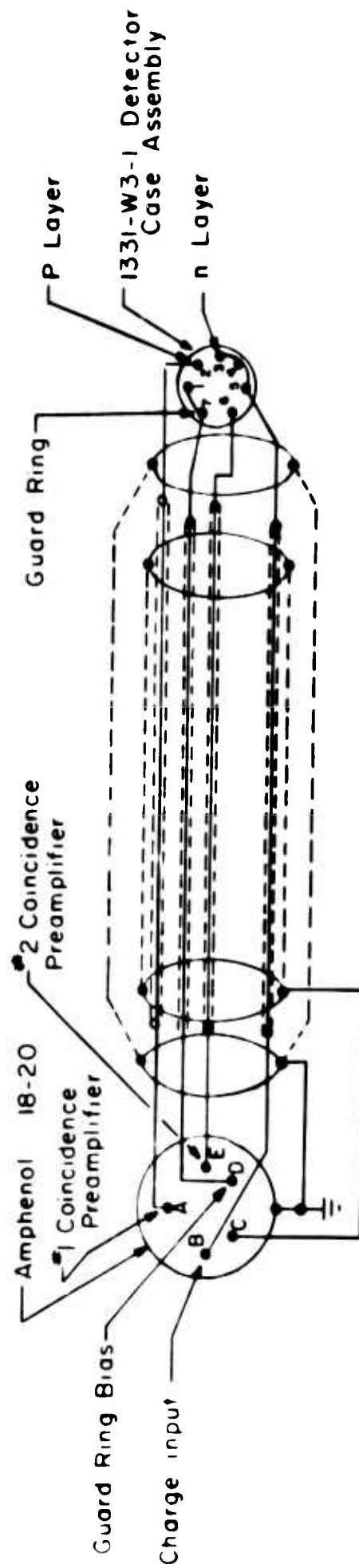
Figure 4.17 Wiring diagram for detector input cable.

72

3. Control unit.

   a. Charge-sum gain and shaping
   b. Amplitude triggers No. 1 and No. 2
   c. Coincidence-sum amplifier
   d. Coincidence trigger
   e. +45V dc supply
   f. +25V dc supply
   g. 0 - 100V dc supply

The control unit, which could be remotely connected from the detector and preamplifiers, provided the following outputs and provision for testing and adjusting the system:

4.5.1 System Outputs

   a. A (+) polarity-shaped output proportional to the sum charge of the two solid-state detectors.
   b. A (-) polarity-wideband output proportional to the sum charge of the two solid-state detectors.
   c. A (+) polarity-coincidence trigger which gates the multichannel analyzer when coincidence events occur in the two solid-state detectors.

4.5.2 System Test Points

   a. Coincidence amplifier No. 1 and No. 2 outputs (TP7) and (TP8).
   b. Coincidence-sum output (TP9).
   c. Detector bias voltage (TP4).
   d. 25-volt B+ voltage (TP5).
   e. 45-volt B+ voltage (TP6).

4.5.3 System Adjustments

   a. Amplitude-trigger No. 1 sensitivity.
   b. Amplitude-trigger No. 2 sensitivity.
   c. Coincidence-time adjust.
   d. Coincidence-trigger amplitude.
   e. Coincidence-trigger pulse width.
   f. Charge-sum sensitivity V/MeV.
   g. Charge-sum polarity.

4.5.4 Test Inputs

The preamplifier unit contained test input points TP1, TP2, and TP3, where a simulated charge could be injected into the system with a fast-rise, exponential-decay, pulse generator.

4.6 System Calibration and Checkout - General

System checkout and initial calibration is made with a mercury relay-pulse generator to simulate nuclear-pulse inputs.

The final system calibration uses a nuclear source and multichannel pulse-height analyzer.

For the initial checkout and calibration, the procedure is as follows:

1. Attach the system by connecting cables.

2. Power supply - Check power supply outputs. Adjust to +25 and +45. (The system operates properly when these values are within ± 10 percent of their design values.)

3. Bias supply - Adjust detector bias supply to operating voltage (50 to 100V, depending on the individual detector).

4. Charge amplifier - Connect a mercury-relay pulse generator to the charge-amplifier test point. A negative pulse of approximately 40 mV into a 91-ohm terminated cable gives an output pulse from the sum amplifier roughly equivalent to a detected nuclear particle of energy of 2 MeV.

5. Preamplifier gain adjustment - Connect the pulse generator to the two coincidence preamplifier test points and set the pulse at +40 mV. This approximates a 2-MeV signal. Connect the oscilloscope to the BNC test point on the control cabinet. Set the test selector switch to amplifier No. 1 position, and adjust the amplifier gain until a signal of 0.4 V is observed. Adjust the other coincidence preamplifier gain in the same way. (The purpose of this gain setting was to provide a threshold of 0.4V for the amplitude trigger).

6. Amplitude-trigger adjustment - Observe the trigger output on the oscilloscope connected to the BNC test point with the test selectro turned to the trigger sum position. Set both trigger adjustments to off, i.e., extreme counterclockwise position. Turn up first trigger adjustment until a triggered condition appears on the scope. Increase second trigger adjustment until a wave form of twice this amplitude is produced. (The output wave form is that of a differentiated square wave, and the amplitude is controlled by the gain setting of the trigger-sum amplifier).

7. Coincidence time adjustment - Make adjustment by using a predetermined length of coaxial cable on one preamplifier for a delay line. (The delay is approximately 1 5 nanoseconds per foot of R558/CU cable.) Connect the oscilloscope to the coincidence output, and increase the pulse generator to approximately 60 mV to remove the half-trigger condition. Turn the coincidence time adjustment to maximum to obtain a trigger setting for the oscilloscope, then turn the time adjustment down until the half trigger condition is observed. This setting corresponds to the delay time of the input cable.

5. EXPERIMENTAL EVALUATION OF NEUTRON CONVERTERS COMBINED WITH P-N JUNCTION DETECTORS

5.1 Coated Detectors

Several detectors, combined with the neutron-sensitive materials discussed in Section 2, were exposed to various neutron sources to determine the characteristics of their response. The nature of the energy distributions and neutron detection efficiencies were observed as functions of coating material, detector dead-layer thickness, and discriminator settings. The results are compared to those found from the theoretical expressions developed in Section 3.

5.1.1 Apparatus

The thermal neutron flux used for the observations discussed in the following paragraphs was produced by $\approx$ 1-curie, polonium-beryllium, neutron source placed in the center of a cylindrical paraffin cask. A specially designed detector holder, which extends into the maximum flux region, was inserted into a well in the cask. While the neutron flux was not calibrated, the detector assembly could be accurately positioned in the well so that valid comparisons could be made between successive exposures.

The detector holder was designed to allow easy interchange of detectors and also of the small discs onto which the neutron charged-particle converter material was deposited. The detector disc assembly was enclosed in a container which could be evacuated during the observations to prevent charged-particle energy loss in traversing the gap between the surfaces of the converter and detector During operation the detector and converter material surfaces were held parallel with a gap distance of approximately 1 mm. This arrangement permitted detectors and radiators to be interchanged for comparison without significantly changing the characteristics from those of a detector on which the radiator material was coated directly to the surface.

Pulses from the detectors were amplified by a low-noise level, charge-sensitive amplifier and displayed on a multichannel analyzer. The amplifier noise was less than the equivalent of 10 keV FWHM, while the complete system including the detectors had a noise level of 22 keV FWHM.

5.1.2 Experimental Procedures

The observations were made with three detectors, each with a different dead layer and a different radiator on each of the three detectors. The radiators used were Li^6, B^{10} and U^{235}. Higher-energy alpha particles, 4.76 MeV from U^{234} and 6.05 MeV and 8.78 MeV from Pb^{212}, were used for calibration of the amplifier and multichannel analyzer system and for detector dead-layer determinations.

The first step in the evaluation procedure was the determination of dead-layer thicknesses of the three detectors. These

values were used to calculate neutron counting efficiencies, which were then compared to the experimentally observed values. A comparison between the theoretical and experimental results gave an indication of the validity of the theoretical method.

5.1.3 Determination of Dead-Layer Thickness

Dead-layer thicknesses for the detectors were determined by four independent measurements, the results of which are tabulated in Table 5.1a. In the first determination the distribution of alpha particles from the B^{10} (n, α) Li^7 reactions in a thick B^{10} radiator was observed. The extrapolated upper energy of the distributions $\overline{E}$ was observed, and the dead layers were calculated from the equation:

$$d = K\overline{E}_0^{\gamma} - K\overline{E}^{\gamma}, \tag{5.1}$$

where the meaning and values of the terms are given in an earlier section (Section 3.1). An earlier system calibration based on the observed Pb^{212} alpha-particle energy distribution was assumed.

The alpha-particle energy distribution above 0.68 MeV emitted from the thick B^{10} radiator is shown in Figure 5.2 as observed by two of the detectors. The energy distributions in Figure 5.1 were calculated for comparison by Equation (3.12). The calculated curve corresponding to $d = 0$ was normalized to the experimental data in Figure 5.2, where it is shown as a broken curve. The qualitative agreement between the calculated and observed distributions is quite good.

A second measurement of dead layer was made by a similar procedure with the 4.76 MeV alpha particles emitted from U^{234} contained in a thick uranium radiator. The neutron source was not used, since the disintegrations producing the alpha particles were spontaneous. This source was chosen because the higher energy alpha particles permit better observation of the thicker dead layers than that which can be made with the relatively low-energy alpha particles from the B^{10} reaction.

A third determination of dead layer was made by observing the 6.04-MeV alpha peak from a thin Pb^{212} source placed a few centimeters from the detector. In this configuration the observed peak has a FWHM of less than 30 keV. A shift ΔE MeV in the observed peak energy results from a detector dead layer, d, given by

$$d = \frac{\Delta E}{dE/dx}, \tag{5.2}$$

where d is in microns and dE/dx is in MeV/micron. The value dE/dx is found from slowing-down data.

The final method of determining dead-layer thickness depends on the relative positions of the upper edges of the alpha-particle peak and the triton peak from the reaction $Li^6(n, \alpha)T$, as discussed earlier in (Section 3.5). The distributions shown in Figure 5.4 were obtained from a thin film of Li^6 exposed to thermal neutrons.

TABLE 5.1a DETECTOR DEAD-LAYER THICKNESS DETERMINATION

Detector Serial Number	$B^{10}(n,\alpha)Li^{7}$ $E_o=1.47$ MeV		U^{234} $E_o=4.76$ MeV		Pb^{212} $E_o=6.04$ MeV		Average d (Microns)
	Endpoint $\underline{E}$ MeV	d(Microns)	Endpoint $\underline{E}$ MeV	d(Microns)	Peak Energy $\underline{E}$	d(Microns)	
6L102	1.426±0.025	0.16±0.1	4.760	-	6.036±0.012	0.03±0.1	0.13
7L103	1.000±0.033	1.59±0.1	4.538	1.35±0.25	5.860±0.012	1.40±0.2	1.39
9L104	0.620±0.041	2.66±0.1	4.378	2.40±0.25	5.728±0.012	2.42±0.3	2.45

$Li^{6}(n,\alpha)T$
$E_{o\alpha}=2.05$ MeV $E_{oT}=2.73$ MeV

Detector Serial Number	Endpoint Channel $\overline{A}_\alpha$ MeV	Endpoint Channel $\overline{A}_t$ MeV	Ratio $\dfrac{\overline{A}_t}{\overline{A}_\alpha}$	d(Microns)	Average d (Microns)
6L102	167±1	224±1	1.34±0.01	0.11±0.03	0.13
7L103	139±2	219±1	1.58±0.02	1.22±0.08	1.39
9L104	110±2	216±1	1.96±0.04	2.38±0.08	2.45

77

TABLE 5.1b COUNTING-EFFICIENCY COMPARISON				
Detector Serial Number	Dead-Layer Microns	$B^{10}(n,\alpha)Li^7$ N (calculated) counts/cm^2 sec	$\underline{E}=0.682$ MeV N (measured) counts/cm^2	D=2.50 Microns n events/cm^3 sec
6L102	0.13	.562 n	5.49×10^4	9.75×10^4
7L103	1.39	.121 n	0.974×10^4	8.07×10^4
9L104	2.45	-	-	-

Detector Serial Number	Dead-Layer Microns	U^{234} N (calculated) counts/cm^2 sec	$\underline{E}=2.0$ MeV N (measured) counts/cm^2	D=14.6 Microns n events/cm^3 sec
6L102	0.13	.358 n	2.37×10^5	6.62×10^5
7L103	1.39	.299 n	1.96×10^5	6.57×10^5
9L104	2.45	.253 n	1.71×10^5	6.77×10^5

Figure 5.1 Calculated spectra for $B^{10}(n,\alpha)Li^7$ alpha particles from B^{10} infinite-thickness coating on detectors with various dead layers
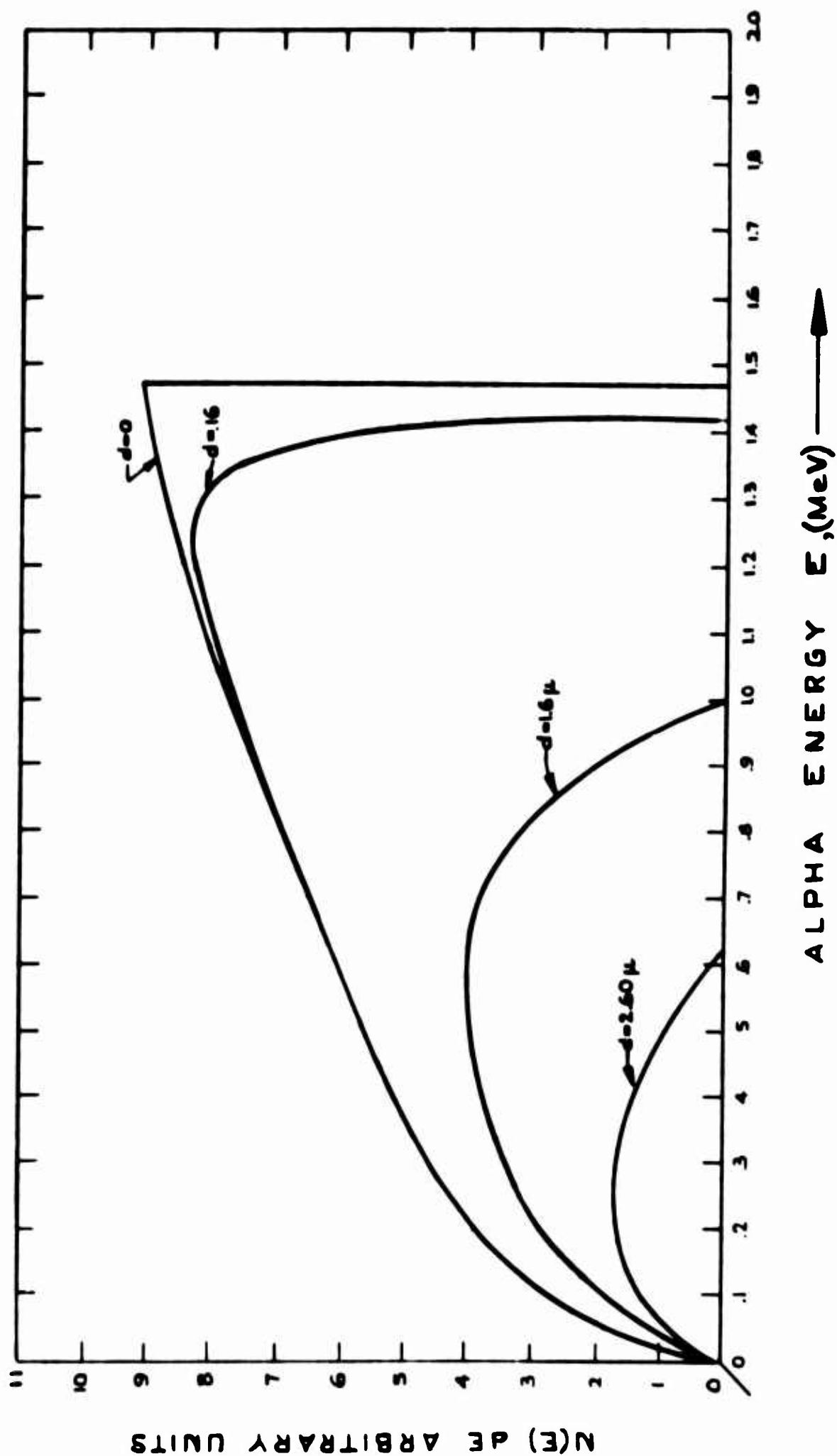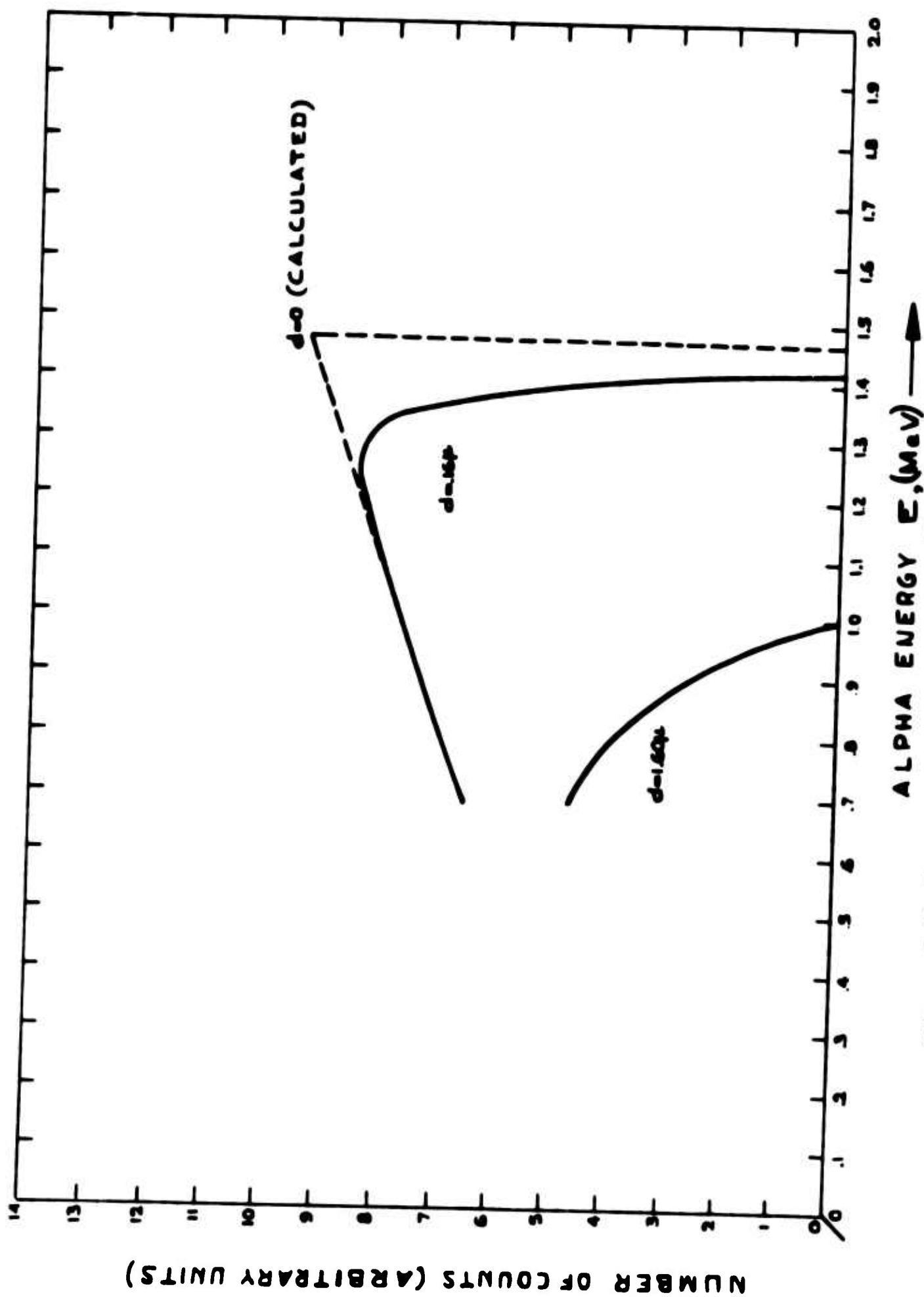
Figure 5.2 Experimental spectra for $B^{10}(n,\alpha)Li^7$ alpha particles from B^{10} infinite thickness coating on detectors with various dead layers.
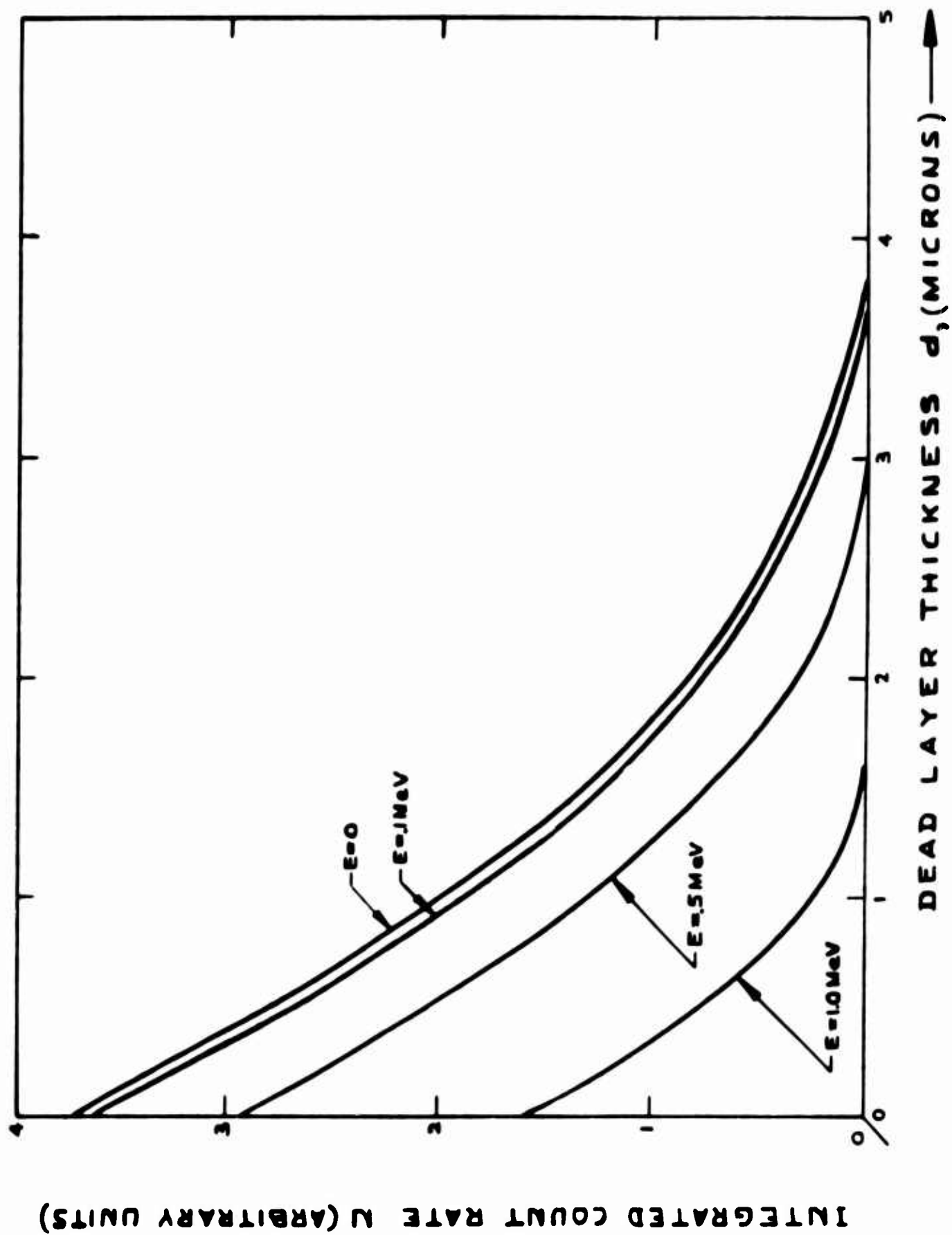
Figure 5.3 Calculated counting efficiency versus dead layer
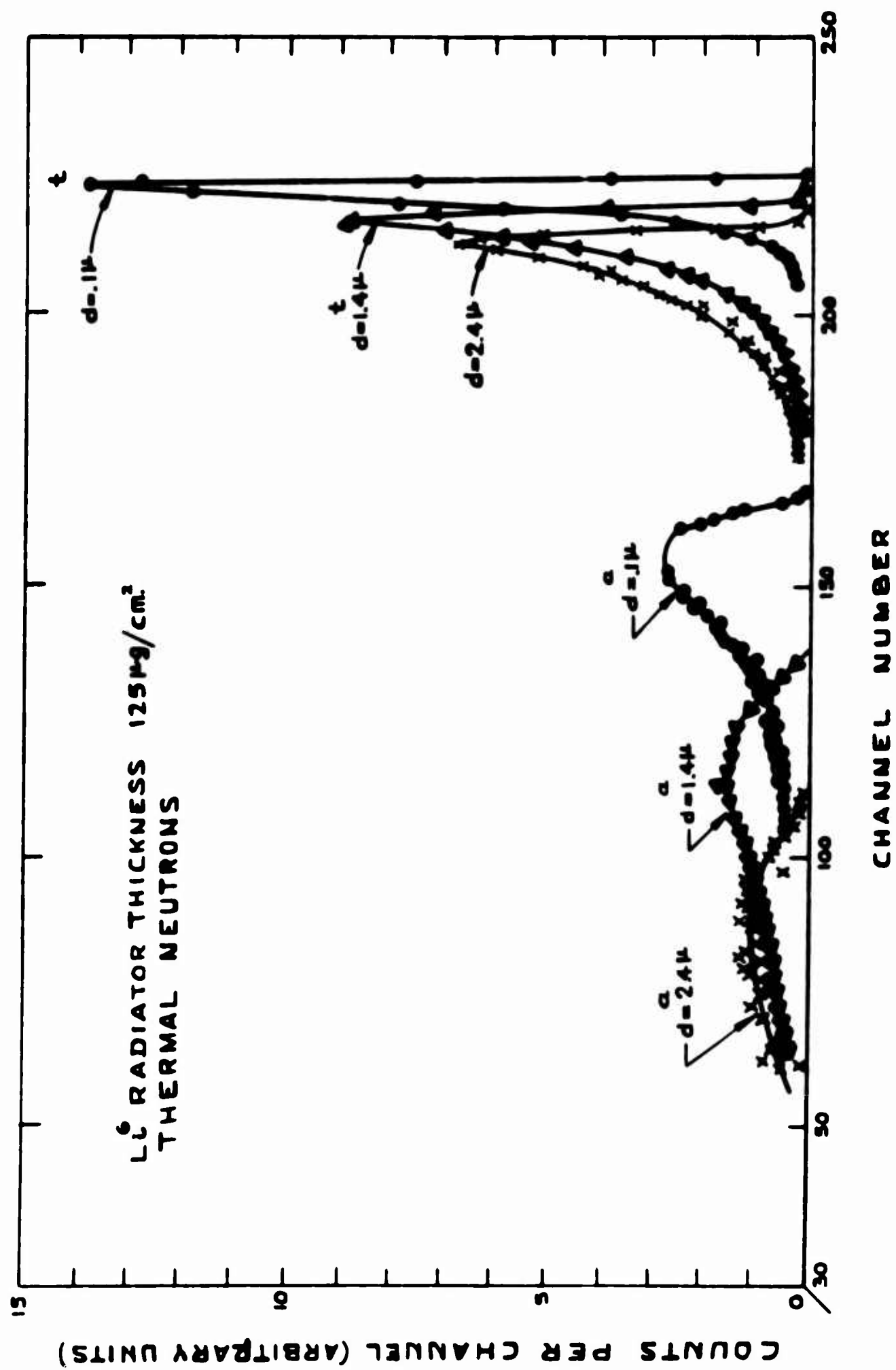with discriminator level as a parameter.

81

Figure 5.4 Observed alpha and triton spectra from $Li^6(n,\alpha)t$ reaction

The ratio of upper edges of the two peaks are calculated and the value of dead-layer thickness is read from the calculated curve of Figure 3.5. This method does not depend on the system calibration. However, there is some uncertainty in the position of the upper edge of the alpha energy distributions for thicker dead-layer detectors.

The results of the dead-layer thickness determinations are shown in Table 5.1a. The results are in general agreement to within the accuracy of measurement. The value of 0.03 μ for the thin dead-layer thickness, as determined by the 6.04 MeV source, is not significant, since the peak shift in this case is less than the uncertainty in the system calibration.

5.1.4 Counting Efficiency

A comparison, using the thick B^{10} radiator, was made between the experimental and calculated counting rates, to determine the validity of the theoretical approach. Alpha-particle energy distributions were observed by the two detectors having the lesser dead-layer thickness (Figure 5.2). The total number of counts observed for a fixed time and with energies above the discriminator setting of $\underline{E}$ = 0.682 MeV were determined by measuring the area of the distribution curve with a planimeter. These values, adjusted to a detector area of 1 cm^2, are shown in Table 5.1b under N (measured). A calculated value for integrated counting rate per unit area was determined from Equation (3.16). As a convenience for the calculation, a quantity D (=equivalent discriminator depth) was defined as the maximum distance from which an alpha particle produced with energy E_0 could reach the detector with residual energy $\underline{E}$. This is found from Equation (3.3b) to be

$$D = K (E_0^\gamma - \underline{E}^\gamma). \qquad (5.3)$$

From this expression, the integrated counting rate per unit area from a thick radiator is found from Equation (3.16) to be

$$N = \frac{n}{4} \frac{(D-d)^2}{D}, \qquad (5.4)$$

where n is the alpha-particle production rate per unit volume in the radiator material and d is the dead-layer thickness. Integrated counting rates for a thick B^{10} radiator have been calculated by (5.4); these are shown in Figure 5.3. It is significant that a thick dead layer drastically reduces the counting efficiency of a B^{10} coated detector.

The average dead-layer thickness as determined from the previous Section 5.1.3 was used in Equation (5.4) to find the values of N(calculated), shown in Table 5.1b. These were compared to the experimental values to determine n, which should be independent of the particular detector used. The agreement between the two values of n is only fair, due to the relatively large value of the discriminator setting and the serious error introduced by the uncertainty in the difference (D -d).

83

The experiment was repeated with the 4.76 MeV alpha particles emitted from a thick uranium radiator. The agreement in values of n in this case was good. Although this observation was made independent of the neutron source, the energy distribution of alpha particles has the same form as that produced from a thick B^{10} radiator. The observations effectively substantiate the theoretical results given in Equation (3.16).

5.1.5 Uranium Coatings

A U^{235} fission spectrum was observed in a thermal flux by use of a U^{235}-plated nickel foil in proximity to a semiconductor detector. The foil and detector were operated in an evacuated tube so as to eliminate straggling due to air. Results were compared to the distribution of fission fragment energies as observed by other methods[4,5]. The loss in energy was adequately accounted for by the 1-micron detector window and the 1 mg/cm^2 thickness of the U^{235}. The response to thermal neutrons of detectors having thick coatings of U^{235}, i.e., a few milligrams per square centimeter, applied by solution evaporation was observed. Straggling due to the thick radiator surface and detector window resulted in a broad distribution in which the characteristic double peak was practically obscured. However, this poor resolution did not depreciate the usefulness of the coated detector as a neutron detector. On the other hand, little or no advantage in sensitivity is gained by increasing the amount of uranium on the surface to greater than approximately 1 mg/cm^2, since this results only in the production of more low-energy pulses below the discriminator level.

Observations of a U^{238}-coated detector were made by noting occasional high energy pulses on an oscilloscope with the detector in close proximity to the bare polonium-beryllium source. Obtaining good statistics with this arrangement was not practical, due to the relatively weak source and low cross section of U^{238}. However, fission pulses were observed, which indicated that the detector was detecting fast-neutron induced fissions. The energy of these fission fragment pulses was well above that recorded for the pulses from the (n,p) in silicon.

5.2 Li^6 Spectrometer

The first step in the experimental evaluation of the Li^6 spectrometer system was the measurement of the individual detector dead layers, the noise level, and linearity of the system. The qualitative response of the system to thermal neutrons was observed and used as a basis for adjustment of the system parameters. Detailed observations of the effects of system parameter settings were made from thermal neutrons as a source. Finally, the spectrometer was used to observe the neutron spectrum produced by the D (d,n) He^3 reaction in an accelerator. One of the very early Li^6-sandwich detectors was operated in the core of a low-power, fast, experimental reactor; the results are included in this section.

5.2.1 Preliminary Evaluation

Prior to assembly of a Li^6-detector sandwich (Figure 2.1), the individual detectors were selected and matched for similarity in noise levels and dead layer thicknesses. After assembly, the detectors were rechecked for noise with the Solid State Radiations, Inc. production evaluation equipment. The final detector evaluation was made with the detector connected to the Li^6 spectrometer system. The Li^6-sandwich assembly is designed to fit a standard 7-pin tube socket with base connections, as shown in Figure 5.5. Special tube base adapters were made, as shown in Figure 5.5, which would permit observation of the individual detector characteristics while operating with the spectrometer system. One detector terminal was connected directly to the B+ supply so that its signals would not contribute to the sum; however, the base connection was unchanged to permit normal operation of both of the coincidence amplifiers.

The operation of the system was studied first by observing the response of individual detectors. Several observations were made to determine the energy calibration, noise contribution, and effective dead layer of each detector. The response of an individual detector, exposed to thermal neutrons from a polonium-beryllium source surrounded by paraffin, is shown in Figures 5.6a and 5.6b. In this arrangement the coincidence circuit was in operation even though one-half the detector assembly was not contributing to the sum signal. Figure 5.6b is the result obtained with the coincidence discriminator set at a very low level so that noise pulses are recorded. The alpha-particle and triton peaks are shown clearly. The sharp peak shown at a higher energy is from a pulse-generator test input used to determine the noise and linearity of the system. The detector noise level independent of the system was between 18 and 20 keV FWHM at 200 V applied bias. The system noise as indicated by the spread in energy of the pulse-generator peak is approximately 36 keV FWHM. By contrast, the triton-peak resolution is observed to be 63 keV FWHM. The spread in the alpha-particle peak is much greater, due to the smaller range of alpha particles. Figure 5.6a shows essentially the same type of spectrum except that the coincidence discriminator is set at 1.5 MeV. This results in a reduction of the low-energy noise.

The observed single-detector spectra (Figures 5.6a and 5.6b) are used to determine dead-layer thicknesses by the ratio method as discussed in a previous section (Section 5.1.3). Typical values for the Li^6-sandwich detector are between 0.7 μ and 1.5 μ. Energy losses due to these dead layers are around 0.25 MeV for alpha particles and 0.03 MeV for tritons. Detectors selected for any Li^6-sandwich assembly were matched so that energy losses due to detector dead layers were the same for similar charged particles, within the system resolution.

5.2.2 Calibration and Adjustment

The Li^6-spectrometer system is provided with a pulse-generator test input, which allows superimposing a pulse-generator signal onto the system without otherwise disturbing its normal operation.
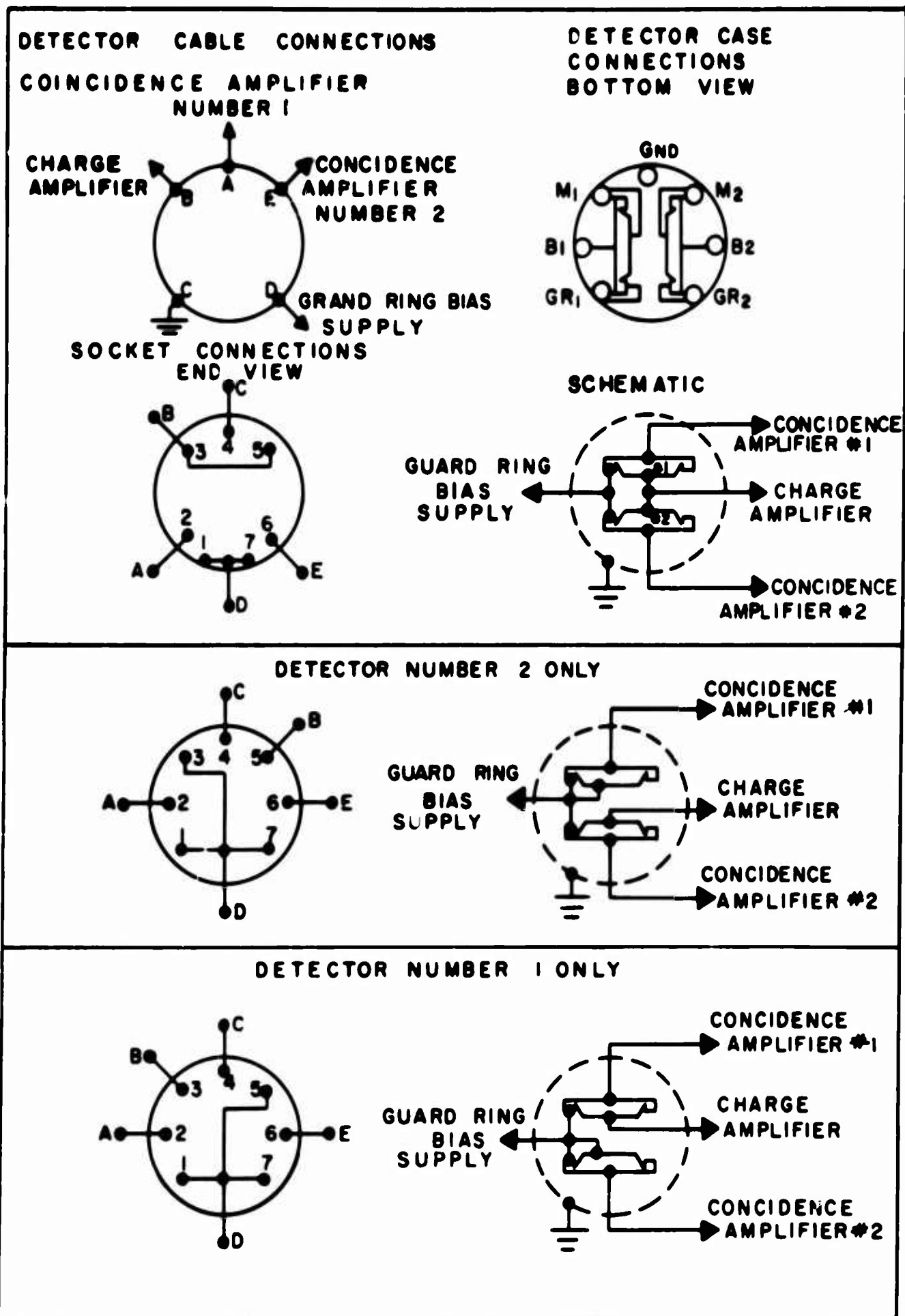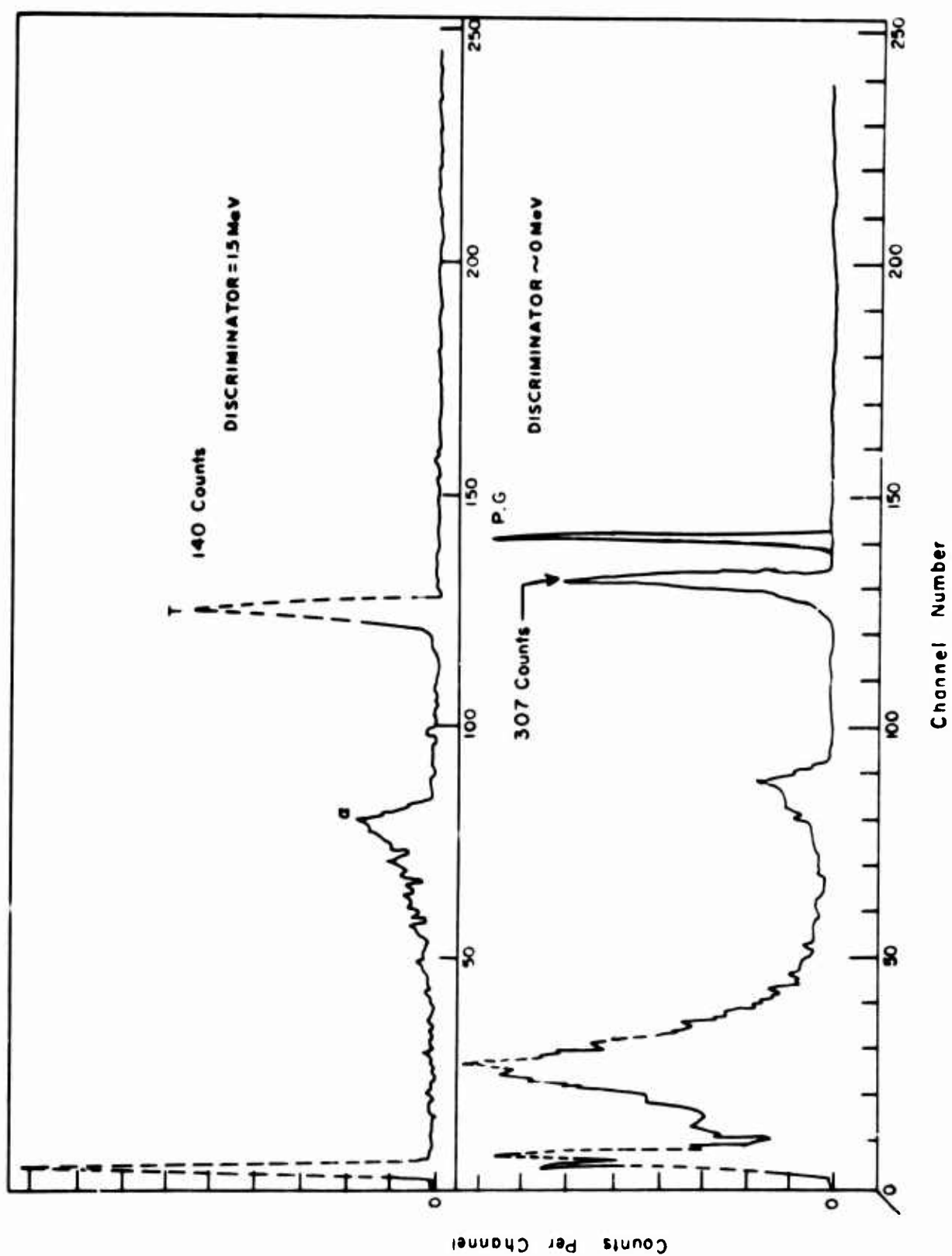
Figure 5.5 Special detector socket connections.

Figure 5.6a Single detector output through sum amplifier without coincidence.
Figure 5.6b Single detector output through sum amplifier without coincidence.

87

As a standard operating procedure, the linearity of the system was checked separately for each detector and for the sum amplifier. This was accomplished by plotting a pulse-generator input versus the amplifier output measured on an analyzer. Observed linearity of the system was within 3 percent.

The output of each coincidence amplifier was observed (Figure 5.7) as a basis for setting the individual gains and coincidence-discriminator levels. The upper edges of the alpha-particle and triton peaks were found by extrapolation, and the energy losses of the two particles were determined. A test pulse generator was calibrated by use of the true energy of the alpha and triton as measured in Section 5.2.1. By use of the pulse generator, it was possible to equalize the gains of both coincidence amplifiers and to set the discriminator level until feedback was visible.

When the coincidence-amplifier discriminator levels were set, it was necessary to set the gating-discriminator output, i.e., the time-resolution control. The purpose of this control is to allow for adjustment of the gating discriminator in terms of the time separation between any two signals. Two pulses of a given pulse height will cause a gating signal only if they occur within this resolving-time setting.

The pulse height of the coincidence-discriminator sum from the "test" output was measured on an oscilloscope, with the coincidence time-separation control adjusted so that the coincidence-discriminator output just ceased firing. The pulse height was recorded. The coincidence time resolution at any shorter time separation was the width of the coincidence-discriminator sum pulse measured at the recorded pulse height.

5.2.3 Spectrometer Response as a Function of System Parameters

Preliminary observations of the over-all system operation were made by observance of the thermal-neutron sum spectrum as produced by a polonium-beryllium source surrounded by paraffin. A thermal sum spectrum, as shown in Figure 5.8a, was observed in which the individual events produced by alpha particles and tritons were effectively suppressed by the coincidence circuit. The discriminator settings were low enough to allow some contribution from background. Figure 5.8b illustrates a similar observation of thermal neutrons by use of a higher coincidence-discriminator setting; this higher setting resulted in the suppression of the low-energy pulses. Beyond these preliminary observations, a detailed study of the spectrometer, using the polonium-beryllium source, was impractical due to the low intensity neutron flux and consequently the very long counting times required for a single observation.

Neutrons from the D+d reaction, produced by the Nuclear Defense Laboratory 750-kV Cockroft-Walton Accelerator, were used for a more detailed study of the spectrometer. The estimated neutron yield was 10^8 n/sec. The detector was placed in close proximity to the deuterium target, and was surrounded by paraffin. With this arrange-

Figure 5.7 Single detector output-coincidence amplifier.
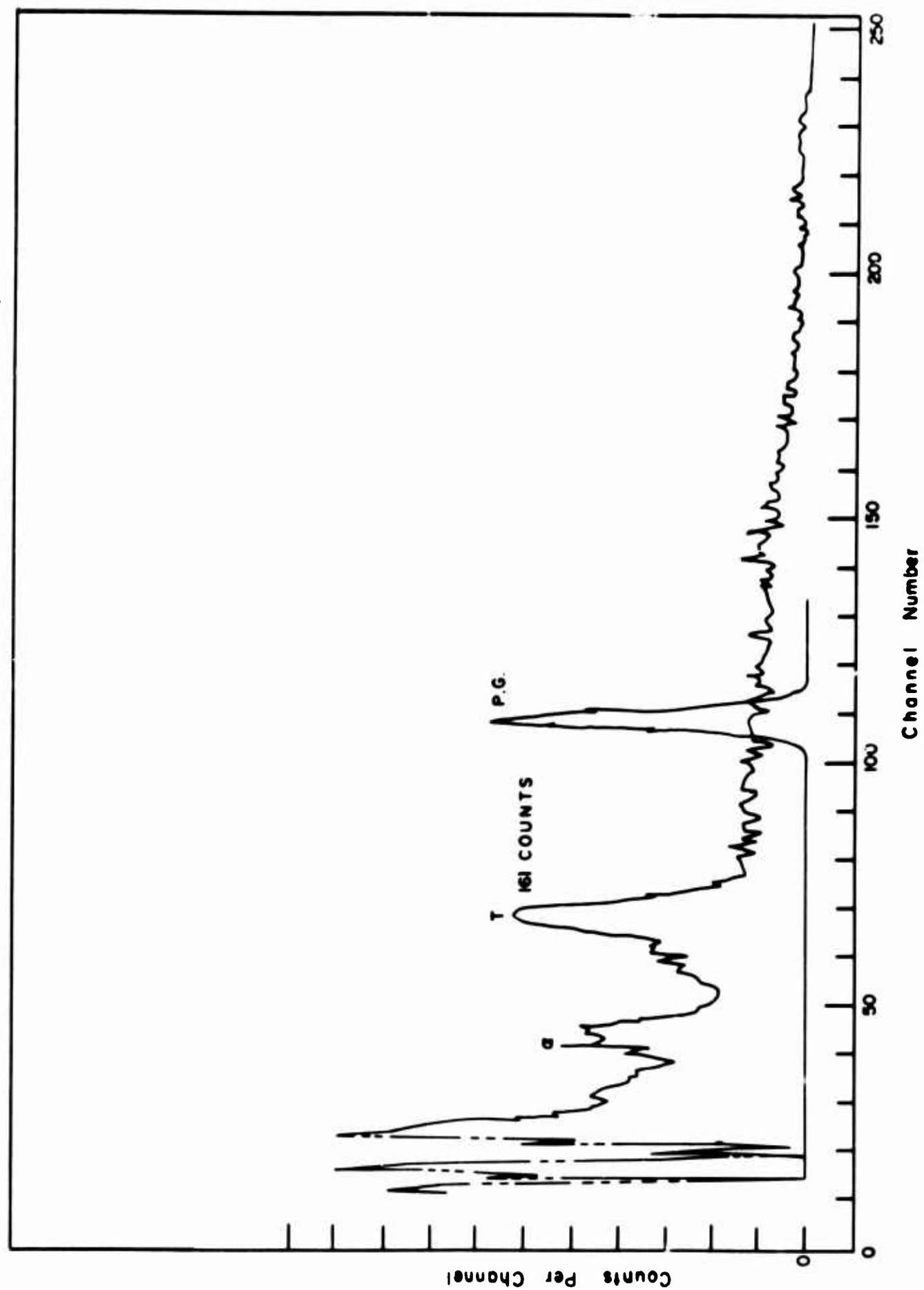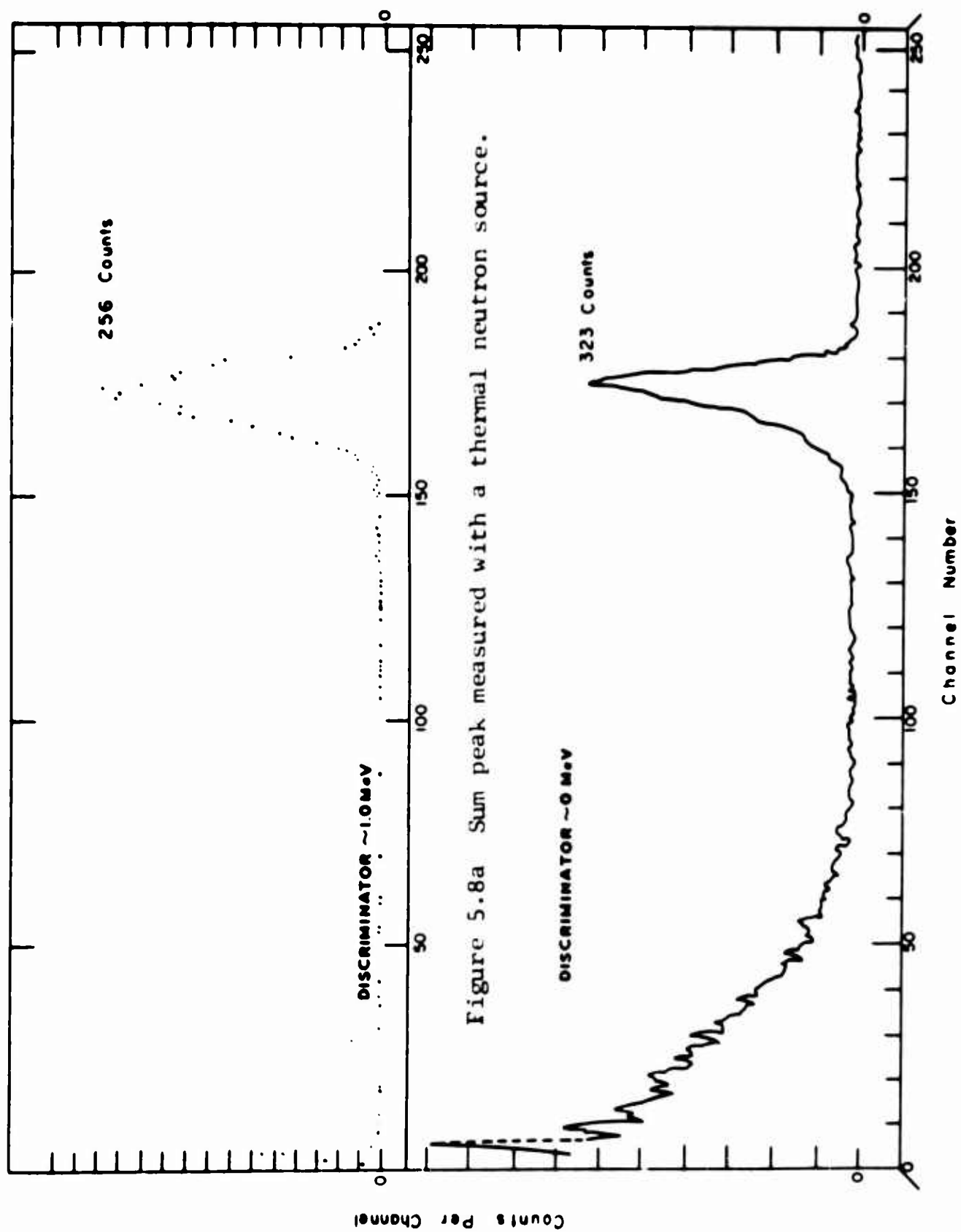
256 Counts

DISCRIMINATOR ~1.0MeV

Figure 5.8a Sum peak measured with a thermal neutron source.

323 Counts

DISCRIMINATOR ~0 MeV

Channel Number

Counts Per Channel

Figure 5.8b Sum peak measured by use of thermal neutrons.

ment an observation of the thermal sum spectrum could be made in one or two minutes. It was thereby possible to observe the spectrometer response over a wide range of adjustable parameters in a relatively short time.

Thermal sum peaks observed as a function of the combination of discriminator settings of the two channels are shown in Figure 5.9. The numbers appearing in the figures beside each sum peak are the respective discriminator settings, where 40 corresponds to an energy just slightly below the maximum alpha-particle energy. The first observed peak (20-20, upper-right figure of Figure 5.9) using equal discriminator settings of 20 has a FWHM of 70 keV and an extrapolated upper energy of 4.60 MeV. As expected, the lower discriminator settings of 10-10 yielded a somewhat broader peak of 130 keV FWHM and an increased total number of counts for the same time interval. However, the upper extrapolated energy appeared to be changed to 4.52 MeV, a significant reduction from the previous observation. This shift was confirmed by the observation 40-35 (bottom left distribution of Figure 5.9), in which the total number of counts was sharply reduced, but the upper edge of the distribution showed a maximum energy greater than 4.7 MeV. Other observations using unequal discriminator settings indicated both a peak broadening and distortion which, in extreme cases, amounted to an actual double peak, as indicated in cases 40-10, 10-40, and 10-32. As both discriminators approached the maximum values corresponding to the condition in which only the highest-energy alpha particles could be observed, the sum peak was shifted toward a higher energy channel. This response appeared to be somewhat anomalous since reducing the discriminator setting to admit lower-energy pulses apparently cut off part of the higher-energy pulses. One would expect the reduction of the discriminator setting to result in a broadening of the peak without any associated shift in the upper edge.

To study this shift in more detail, the triton peak from a single detector was observed with the coincidence requirement as before. A number of single triton peaks are shown in Figure 5.10 as a function of discriminator settings. Again, with the increase in the discriminator setting, the peak showed a shift toward the upper energy and, in addition, a sharp loss of counts. Again, this would indicate that the discriminator was acting as a window rather than simply as a cutoff for the lower-energy pulses.

A possible explanation of this behavior was based on the operation of the coincidence circuit. Two pulses produced by the same nuclear event and in true coincidence, but having different amplitudes, will reach a particular discriminator level at slightly different times. Such an event will not be recorded if the coincidence time is set to a value less than this time difference.

The alpha and triton pulses produced in the spectrometer have some spread in amplitude. Changing the individual discriminator settings while keeping the coincidence time resolution
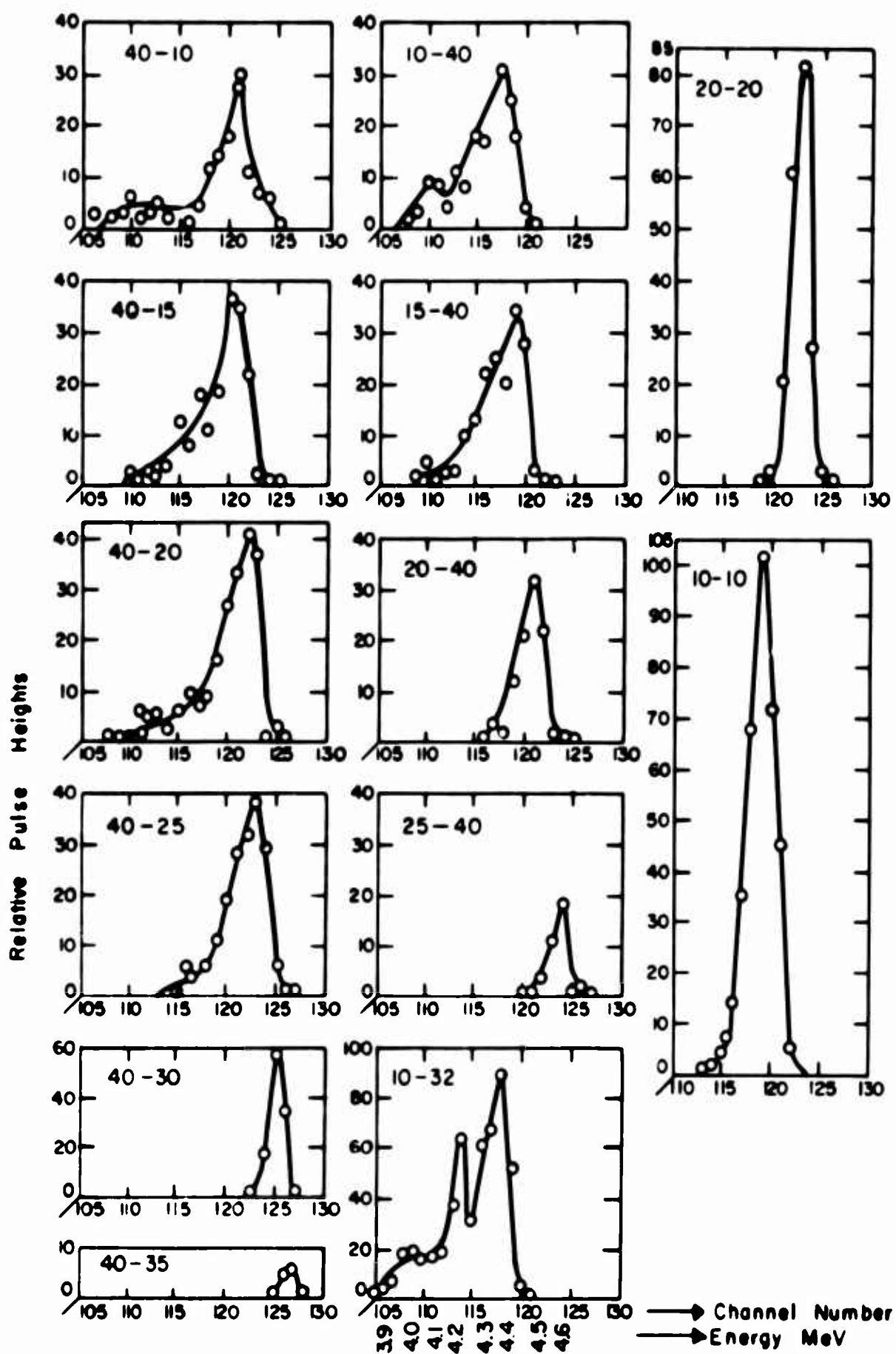
Figure 5.9 Li^6-spectrometer, thermal-neutron sum spectra
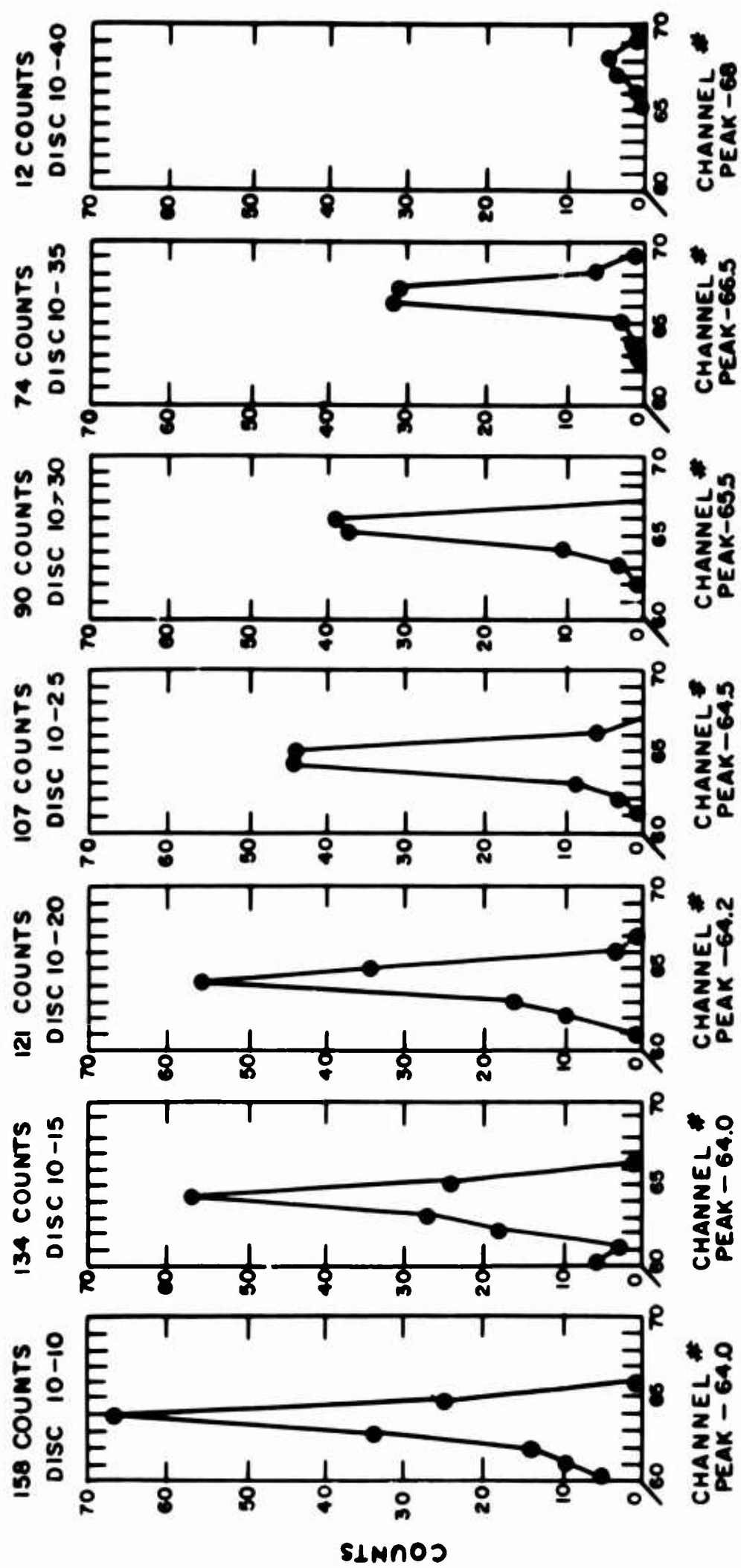taken at various combinations of discriminator
settings.

Figure 5.10 Thermal neutron triton peak at various discriminator settings.

constant may add or subtract sum pulses from either the upper or lower edge of the distribution; this would depend on the relative settings of the two discriminators. To illustrate this effect, assume a situation in which discriminator No. 1 is set well above the maximum of the alpha pulse height distribution, and discriminator No. 2 is set just below the maximum of the alpha pulse height distribution. The coincidence time is now set so that the maximum triton pulse and the maximum alpha pulse will reach their respective discriminator settings just within this time, and so that the sum pulse will be recorded. If the discriminator No. 1 level is reduced, the same maximum triton pulse will reach the new level in less time, while the original time will still be required for the maximum alpha pulse to reach the No. 2 discriminator level. The difference in time will now be greater than the coincidence resolving time, and the sum pulse will be rejected. The net result of this change in discriminator setting is therefore a loss in the upper edge of the sum pulse distribution. The dependence of the upper edge of the sum pulse distribution on the discriminator settings may be reduced by increasing the coincidence resolving time. This, of course, will also allow some undesired, accidental coincidence pulses to get through. On the basis of this explanation, it appears that with this particular discriminator circuit a slow resolving time is necessary in order not to distort the sum peak nor cut out part of the real counts.

5.2.4   Fast Neutron Observations

Observations of the neutrons from a D+d reaction produced by the 750-KV accelerator were made by placing the sandwich detector in close proximity to the deuterium target. In the first observation a small amount of paraffin was placed in proximity to the detector to show the position of the thermal sum peak (Figure 5.11). A second run was made with the paraffin removed. Figure 5.11 shows the raw data as observed with some paraffin in proximity to the detector. The broad distribution above the thermal peak is due to the fast neutrons. Note that the effects of single pulses below the thermal sum peak are quite trivial down to the noise level of the system, where a sharp rise is indicated.

The high-energy distribution was studied in more detail by removing the paraffin. The amplifier gain was reduced to obtain more counts per channel in the high-energy region. The results in Figure 5.12 are the raw data as observed, and the same data normalized for the energy variation in the Li^6 cross section. The observed peak is quite broad and, due to the preliminary nature of the run, the spectrometer resolution is uncertain. However, considering the nature of the D+d source, this distribution is not unreasonable. The deuterium target is a self-replenishing thick target. Neutrons may be produced with a maximum energy in a forward direction approaching 4 MeV. At the same time, neutrons produced by reactions deeper in the target would have lower energies due to the loss in the deuterium energy in penetrating to the reaction depth. The counts well below 2.5 MeV are probably due to some neutron scattering from structure material in the vicinity of the target.
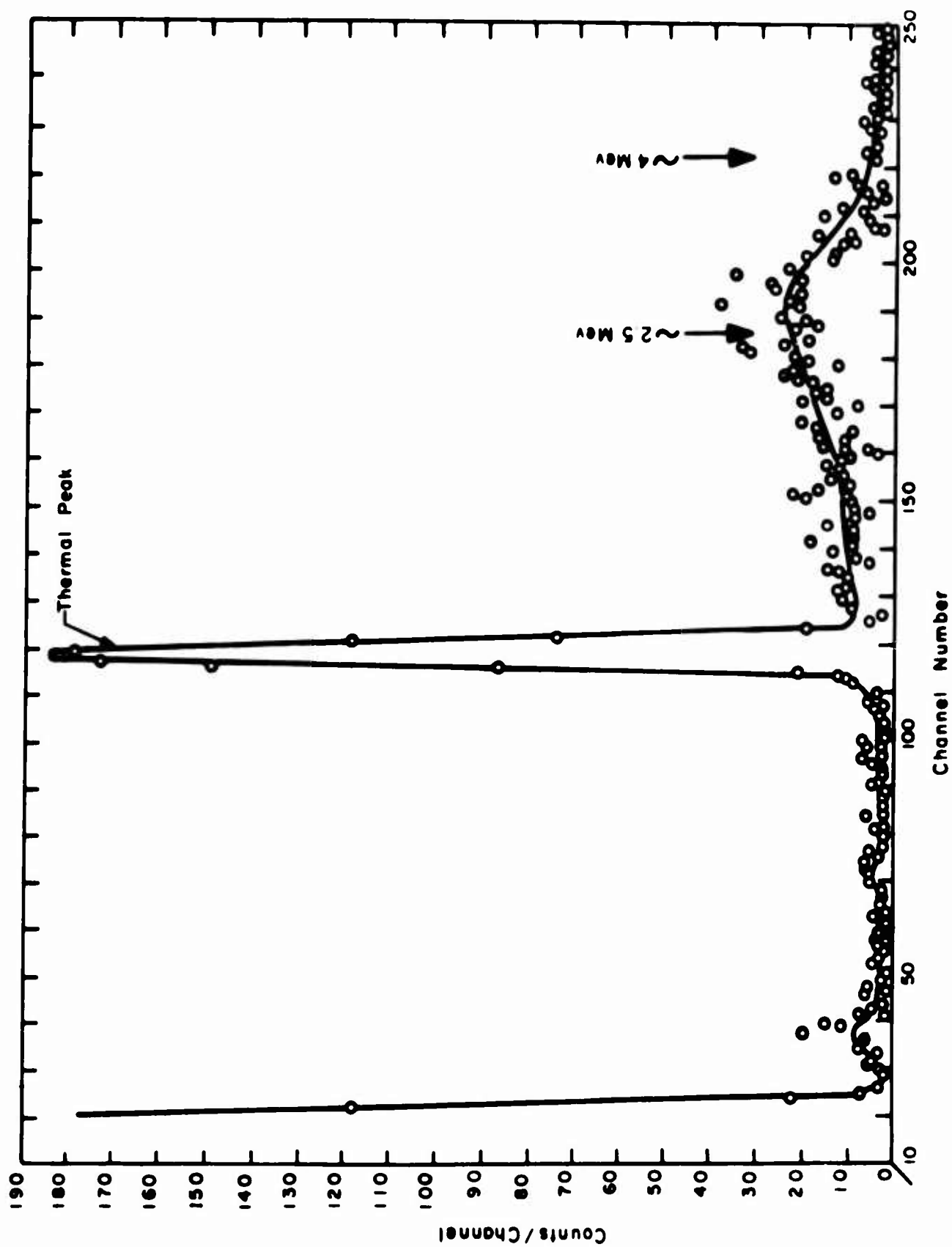
Figure 5.11   Neutron spectrum from D+d reaction (with moderator near detector to show thermal peak).
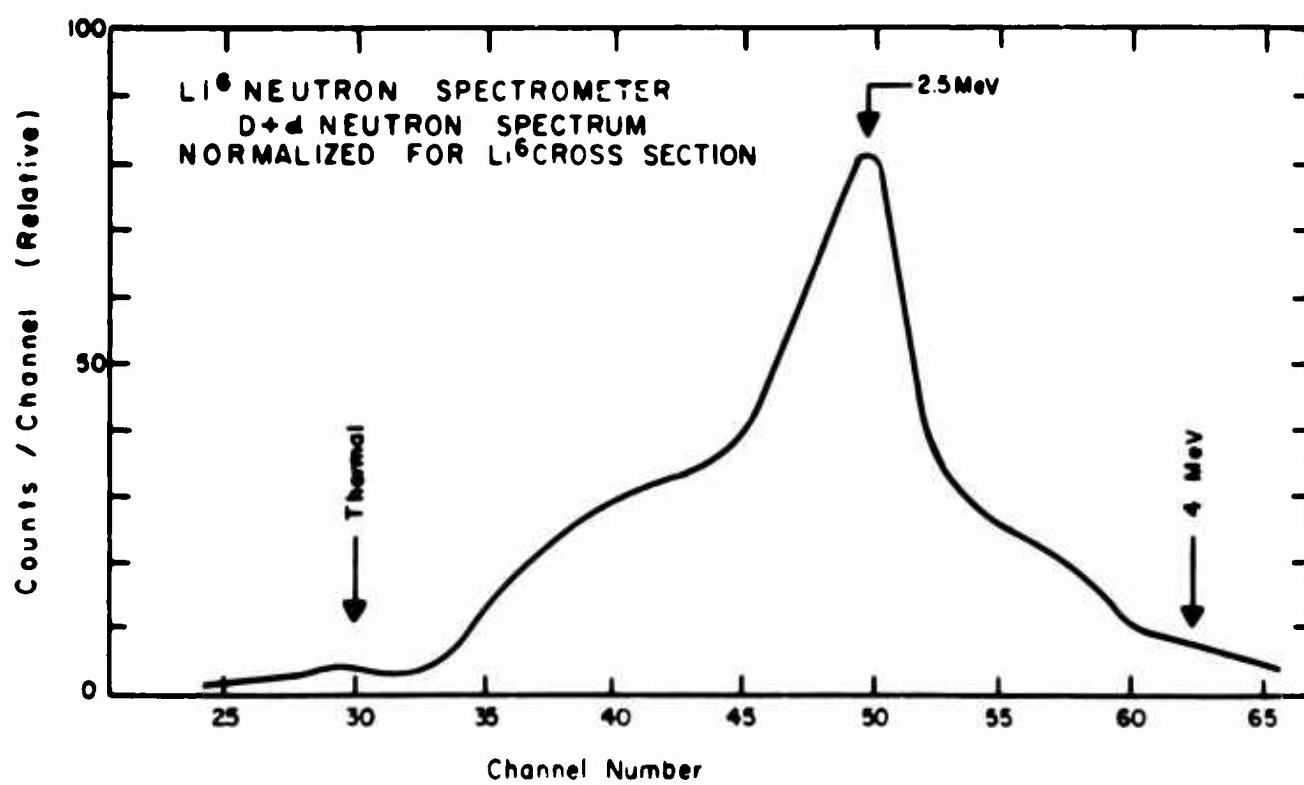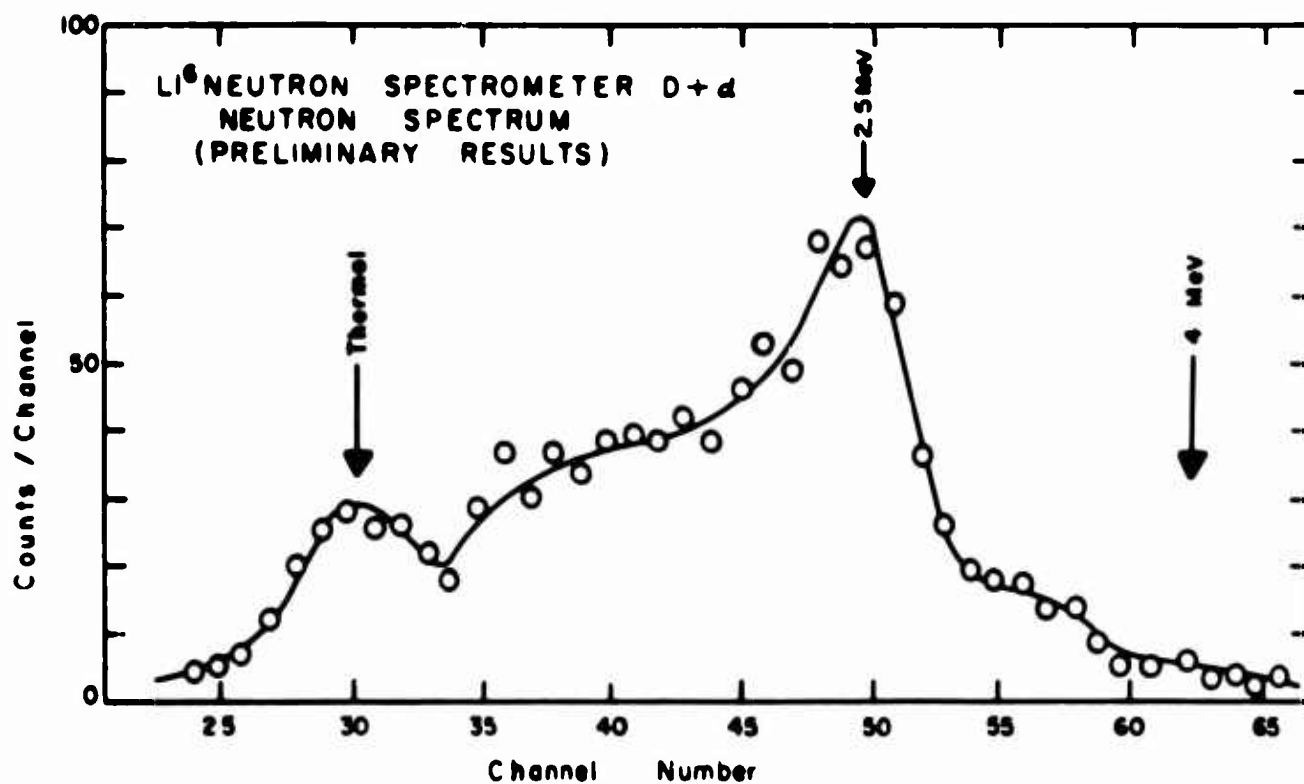
Figure 5.12   D+d neutron spectrum with Li^6 spectrometer.

96

An earlier effort was made to observe 14-MeV neu-
trons of the $T(d,n)He^4$ reaction from a small Cockcroft-Walton accel-
erator. At the time this observation was attempted, there were
a number of uncertainties in spectrometer adjustments and in the over-
all calibration of equipment. A large distribution of pulses was
observed that could be attributed to the $Si^{28}(n,p)Al^{28}$ and other high-
energy reactions in silicon; however, because of the high background
and because of uncertainties in system adjustments, sum pulses caused
by the 14-MeV neutrons were not definitely resolved.

5.2.5 Origin of Spurious Pulses

In addition to the $Li^6(n,\alpha)T$ reaction on which the
operation of the Li^6 spectrometer depends, there are a number of other
high-energy neutron reactions which can seriously interfere with its
effective operation. The ultimate utility of the Li^6-neutron spec-
trometer will depend on understanding and, as nearly as possible,
suppressing the spurious pulses resulting from these reactions. The
most serious problems are due to the high-energy neutron reactions
in silicon, as discussed in a previous section (Section 2.2). In
addition, the $Li^6(n,nd)He^4$ reactions[11] will produce true coincidence
pulses which must be considered in interpreting data from the Li^6
spectrometer. The cross section for the reactions of interest are
shown in Figure 5.13.

Alpha particles or protons produced in one of the
detectors may simply cause pulses in the same detector or may also
enter the other detector, thereby producing pulses in both detectors
in true coincidence. As a consequence, a variety of spurious events
may contribute to the observed sum spectrum, even with good coinci-
dence discrimination. The $Si^{28}(n,p)Al^{28}$ and $Si^{28}(n,\alpha)Mg^{25}$ reactions
form the most serious contribution to the spurious pulses, due to
both high cross-section values and the large amount of silicon in the
detector assembly, as compared with the quantity of lithium.

The $Si^{28}(n,p)Al^{28}$ reaction will have no effect at
incident neutron energies smaller than 3.86 MeV. However, above this
threshold, counts will be added into low-energy channels at rates
that increase with energy. The protons are emitted at all angles
with energies that range from zero up to $(E_n - 3.86)$ MeV. These can
cause true coincidences when a proton penetrates both detectors, or
chance coincidences when pulses in the individual detectors occur
within the coincidence resolving time, τ. The chance coincidence
counting rate, n_c, depends on the product of the individual count
rates in each detector, n_1 and n_2, and the resolution time of the
coincidence circuit, τ.

Since n_1 and n_2 are proportional to the neutron
flux φ, the chance coincidence rate will be proportional to $\varphi^2\tau$. The
Li^6 events occur at a rate proportional to φ, so that the ratio of
these spurious pulses to the desired signal pulses is proportional to
$\varphi\tau$.
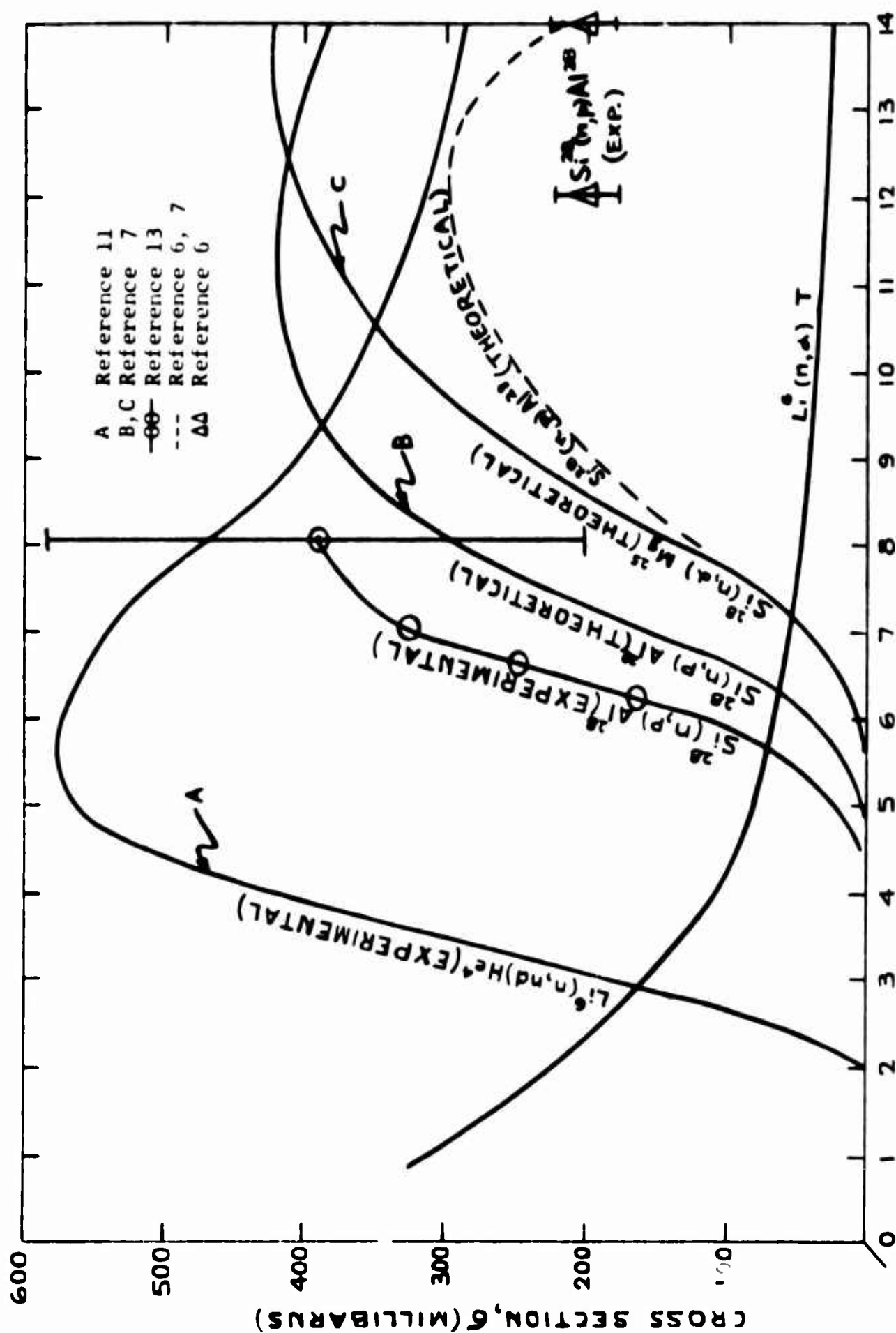
Figure 5.13 Cross sections of materials in the Li⁶ detector assembly.

Effective suppression of these chance coincidence pulses will therefore require a very fast coincidence system and an incident neutron flux as low as practical.

In the event that a chance coincidence occurs between protons of maximum energy from the reaction $Si^{28}(n,p)Al^{28}$, the observed sum will be $E_C = 2(E_n - 3.86)$ MeV. This may be compared with the summed energy of the alpha particle and triton from the Li^6 reactions, i.e., $E_S = E_n + Q = E_n + 4.8$ MeV. The maximum energy of the coincident $Si^{28}(n,p)Al^{28}$ protons increases with energy until at 12.8 MeV, $E_C = E_S$, i.e., the two sums are equal. However, at lower energy, e.g., $E_n = 7$ MeV, the maximum possible proton energy is approximately equal to the minimum alpha-particle energy from the Li^6 reaction. Discriminator settings of slightly over 3 MeV would effectively eliminate the chance coincidences at this value of E_n without interfering with the Li^6-reaction sum peak. This discriminator setting, however, would not be totally effective at higher incident neutron energies.

The second method by which the $Si^{28}(n,p)Al^{28}$ reaction causes spurious pulses is by the direct emission of a proton from one detector into the other. Pulses of this origin will be in true coincidence and cannot be eliminated by simply lowering the coincidence resolving time.

With the discriminator set to a value just greater than one-half the maximum proton energy, coincidence will be prevented; protons of energy E_{max} losing more than half their energy in one detector will not have sufficient energy to trigger the other channel. If the maximum energy of the proton is taken to be

$$E_{max} = E_n - 3.86 = 2\underline{E} , \qquad (5.5)$$

where $\underline{E}$ = discriminator energy setting of each channel, and

$E_\alpha = (3/7)(E_n + 4.8)$ = average alpha-particle energy from the $Li^6(n,\alpha)T$ reaction, then the ratio of average alpha-particle energy to discriminator energy at 14-MeV is

$$\frac{E_\alpha}{\underline{E}} = \frac{(3/7)(14 + 4.8)}{(14 - 3.86)/2} = 1.6 . \qquad (5.6)$$

According to this result, coincidences caused by a single proton traversing both detectors can be virtually eliminated by proper use of the discriminator setting. The factor 1.6 gives considerable allowance for spreading of the alpha-particle peak caused by the initial neutron energy and effects of dead layer. Setting the discriminators as indicated above will effectively eliminate the true coincidence pulses produced by the $Si^{28}(n,\alpha)Al^{28}$ reaction. At the same time, this will discriminate against some of the true alpha-particle coincidences and thereby cut down the efficiency of the device. In addition, a high discriminator setting will preclude observation of neutrons of much lower energy in the presence of fast neutrons.

The contribution of spurious alpha-particle pulses from the $Si^{28}(n,\alpha)Mg^{25}$ reaction becomes significant for neutron energies above $E_n = 7$ MeV, as shown in Figure 5.13. The same comments, which were made in the previous paragraphs about protons from the (n,p) reaction in silicon, are applicable here except that the (n,α) reactions should be less troublesome, due to the shorter range of alpha particles. A smaller fraction of the total silicon will act as an alpha-particle radiator and the chance of a single alpha particle producing pulses in both detectors will be small compared to that for protons.

From the foregoing discussion it is concluded that the most significant source of spurious pulses is from chance coincidences between protons and other charged particles. These may be somewhat suppressed by means of a fast coincidence system and, in some cases, rather high discriminator settings. A lower flux of neutrons will effectively reduce the relative number of chance coincidences and effectively remove higher-energy pulses resulting from pile-up.

An additional high-energy reaction, which is troublesome to the operation of the Li^6 spectrometer, is the $Li^6(n,nd)He^4$ reaction[11], or more properly $Li^6 + n \longrightarrow Li^{6*} + n'$, $Li^{6*} \longrightarrow d + \alpha$. The Q value for this reaction is -1.48 MeV and its cross-section value becomes significant for incident neutron energies above 3 MeV. The two particles from this reaction will give true coincidence pulses with total energies ranging from zero up to $(E_n - 1.48)$ MeV. The maximum alpha-particle energy will be 1/3 of this value. For 14-MeV neutron incidence, only 5 percent of the alpha particles will have energies between 3 MeV and 4.2 MeV, the maximum possible alpha energy from this reaction. The low-energy sum pulses from this source can be eliminated by the discriminators, as was discussed in a previous paragraph. The contribution of spurious pulses from this source are unimportant when compared with those originating in silicon, because of the relative quantities of silicon and lithium in the detector assembly.

5.2.6 Reactor Core Measurements**

Observations of the neutron spectrum of an epithermal nuclear reactor were made at Atomics International, with the Advanced Epithermal Thorium Reactor (AETR) critical assembly. This assembly consisted of an unmoderated central core test region containing U^{233} surrounded by a polyethylene moderated thermal driver region. These observations were made with one of the very early prototype sandwich detectors and an electronic system made up of various miscellaneous parts. As a result, the observations were very preliminary and qualitative in nature.

**We are indebted to Drs. D. Strominger and S. G. Carpenter of Atomics International for permission to use this data.

The pulse height distribution shown in Figure 5.14 has the same form for the high-energy neutron distribution as the semi-empirical U^{233} fission spectrum[6]. The low energy peak is due to some neutron slowing down in the immediate vicinity of the detector sandwich. Figure 5.15 shows a similar observation made in a slightly revised core of the AETR assembly. The observation made in the thermal driver region shows only a broad, low-energy peak. By contrast, the spectrum in the central core also shows the pulse distribution for the higher energy neutrons which falls off in roughly a logarithmic way, as expected from the U^{233} fission spectrum.

6. CONCLUSIONS

Effective techniques for the application of B^{10}, Li^6, U^{235} and U^{238} have been developed for the fabrication of neutron-sensitive detectors. These detectors fall into two classes: simple counting devices and neutron spectrometers.

The B^{10} coated detectors have the highest sensitivity to thermal neutrons. A thick layer of B^{10}, approximately 96 percent enriched, provided an effective thermal neutron detector when applied to the surface of a p-n junction and when operated with an appropriate discriminator threshold to eliminate noise and low-energy pulse contributions. It was shown that to observe an adequate fraction of pulse heights above the noise level of the system and thereby to obtain high neutron-detection efficiency, say ≈ 1 percent, detectors with thin dead layers ($\lesssim 0.5$ μ) are essential. Although detectors with thinner dead layers (0.1 μ) can be fabricated, their reliability at present is generally poor. Selection of dead-layer thicknesses between 0.5 and 1.0 μ represents a compromise between maximum efficiency and reliability. To extend the usefulness of simple coated detectors, fission threshold coatings may be used to provide crude energy information. Since the energy release in fission reactions is much higher than that associated with fast neutron reactions in silicon, the latter may be easily discriminated against when counting fission products. Uncoated detectors are useful for fast neutron detection above 5-6 MeV by virtue of the $Si^{28}(n,p)Al^{28}$ and $Si^{28}(n,\alpha)Mg^{25}$ reactions in the base silicon. The maximum incident neutron energy may be determined from the high energy cut-off of the proton or alpha-particle distribution corresponding to these reactions. The experimental response of the coated detectors operated in the simple counting mode is in good agreement with the theoretically predicted response based on Gobelli's empirical expression[9] for the charged-particle, range-energy relationship.

In addition to the high neutron sensitivity possible with these detectors, high counting rates are possible because of the thin depletion regions required to completely absorb the energy of the heavy charged particles emitted in these reactions. These high counting rates result from the short transit distance and high electron-hole mobilities available in silicon, permitting collecting times less than 10 ns. The present limitation on these counting rates (≈ 100 Mc/s) is imposed by the associated electronic equipment.
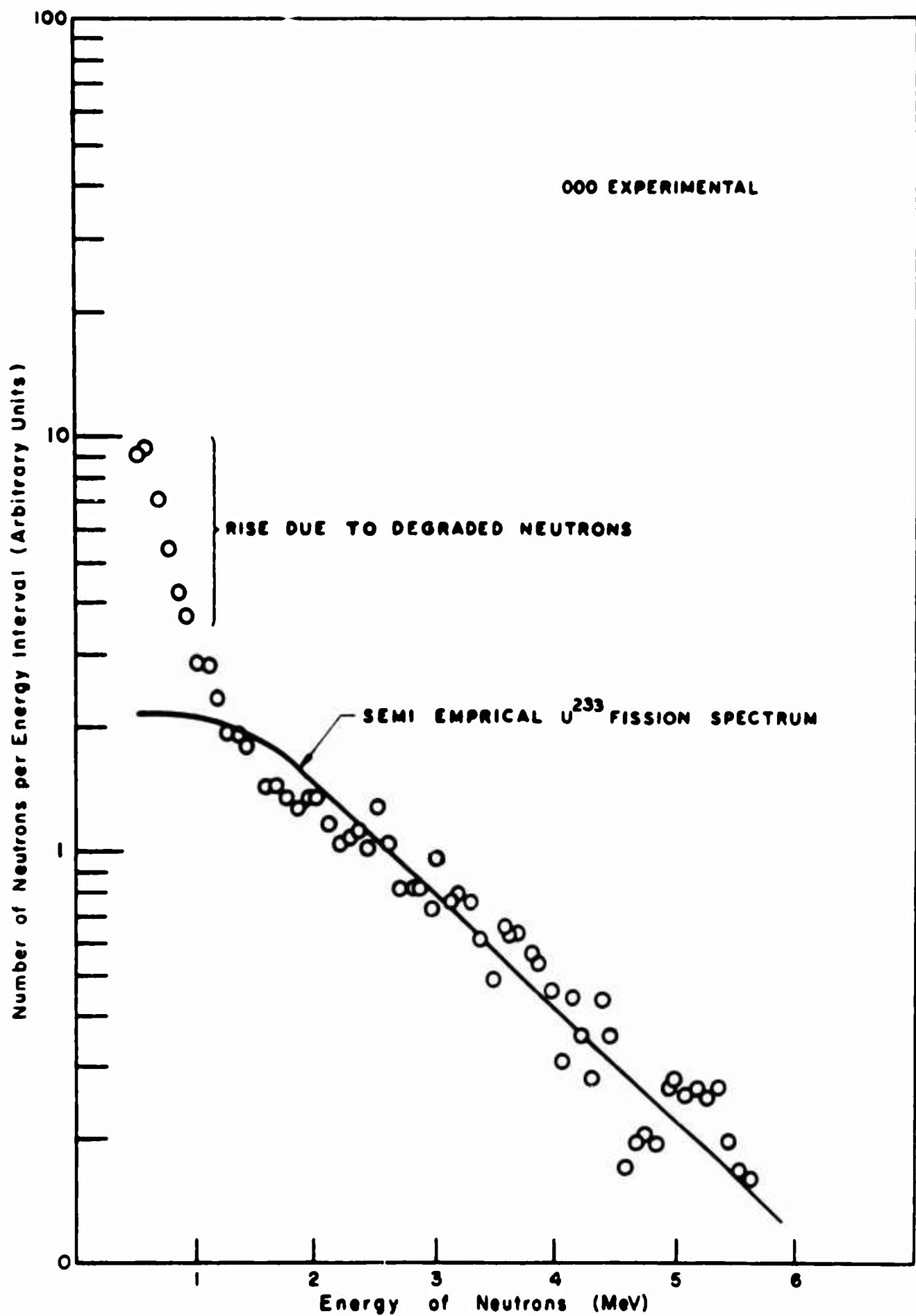
101

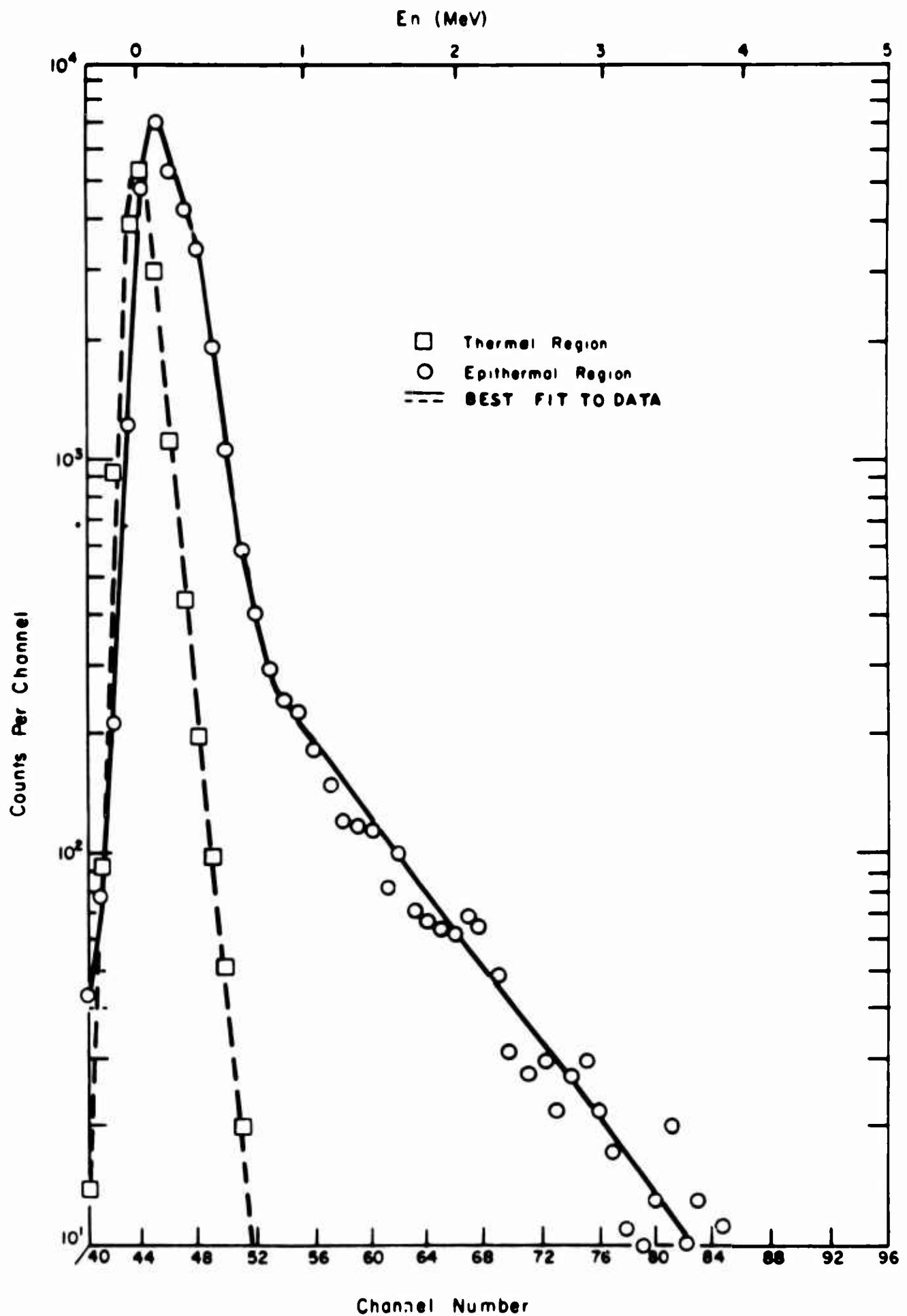Figure 5.14   Neutron Spectrum of U^{233} fission source.

Figure 5.15   Neutron spectrum in low-power reactor.

In the class of detectors useful for neutron spectroscopy, the Li^6-sandwich detector shows the most promise. Preliminary operation of the Li^6 spectrometer indicates that in its present form useful differential neutron spetral data may be recorded for neutron energies up to 6 MeV above which fast neutron reactions in silicon produce a high background and interfere with normal operations. The optimum operating characteristics are critically dependent on the use of matched detectors, coincidence timing adjustments, and fast amplifier delays.

The difficulties encountered in the attempts to observe 14-MeV neutron spectra have led to the suggestions listed below for improvement of spectrometer performance. To suppress the high background of low-energy pulses from the fast neutron reactions in the base silicon, a high-speed coincidence circuit would prove useful in reducing the accidental coincidence arising from high singles count rates. The only means of suppressing real coincidences, due to long range particles (protons) which originate in one detector and penetrate the second, is to select the discriminator setting high enough to avoid counting these events. Such events may arise from either the $Li^6(n,nd)He^4$ or the $Si^{28}(n,p)Al^{28}$ reactions. It would be well worthwhile to pursue a theoretical program for determination of optimum discriminator settings to minimize the contribution from these competing reactions.

Further improvement of the spectrometer performance may be obtained by changes in the sandwich configuration. First, the use of Li^6 metal to replace the present Li^6F radiator will increase the detector sensitivity by approximately a factor of 4, without loss in resolution; second, a significant improvement in both sensitivity and resolution may be realized by use of detectors with thinner dead layers, provided their reliability is not impaired. If detectors of larger area (say X 2 to X 3) were incorporated, a corresponding increase in sensitivity would be realized without impairment of resolution, provided the surface leakage current did not increase the input noise level significantly.

It is anticipated that the use of thin window silicon or germanium detectors at liquid nitrogen temperature would significantly decrease the leakage current noise. The high background counting level produced by neutron-induced reactions in the base germanium is expected to be about 0.25 times the level observed for silicon because of the lower cross section for $Ge^A(n,p)Ga^A$ and $Ge^A(n,\alpha)Zn^{A-3}$ reactions.

REFERENCES

1. S. S. Friedland and F. P. Ziemba, "The Semiconductor Detector," in L.C.L. Yuan and C. S. Wu, Editors, "Nuclear Physics," Vol. 5, Part A, Academic Press, New York, 281 (1961).

2. J. M. Taylor, "Semiconductor Particle Detectors," Butterworths, Inc., Washington (1963).

3. T. A. Love and R. B. Murray, IEEE Trans. Nucl. Sci., NS-8, 91 (1961).

4. C. Kittel, "Introduction to Solid State Physics," 2nd ed, John Wiley & Sons, Inc., New York, 288 (1959).

5. J. Heidmann and H. A. Bethe, Phys. Rev., 84, 275 (1951). See Also K. J. Le Couteur "The Statistical Model" in P. M. Endt and M. Demeur, Editors, Nuclear Reactions, Vol. 1, North-Holland Publishing Co., Amsterdam, 318 ff (1959).

6. J. M. F. Jeronymo, G. S. Mani, J. Olkowsky, A. Sadeghi and C. F. Williamson, Nuclear Phys. 47, 157 (1963); F. L. Hassler and R. A. Peck, Jr., Phys. Rev. 125, 1011 (1962).

7. G. S. Mani and M. A. Melkanoff, Proc. Int. Conf. on Direct Interactions, Padua (1962); A. Agodi and G. Schiffer, Nuclear Phys. 50, 337 (1964); R. E. Bullock and R. G. Moore, Jr., Phys. Rev., 119, 721 (1960).

8. G. Dearnaley, A. T. G. Ferguson, and G. C. Morrison, IEEE Trans. Nucl. Sci., NS-9, 174 (1963).

9. Gobelli, Phys. Rev., 103, 275 (1956).

10. 1960 Nuclear Data Tables, Part 3, J. B. Marion editor, National Academy of Science, National Research Council, Washington, D. C. (1960).

11. L. Rosen & L. Stewart, Phys. Rev., 126, 1150 (1962).

12. Joyce and Clark, "Transistor Circuit Analysis, Addison-Wesley Publishing Co., Cambridge, 257 (1962).

105

APPENDIX A

INPUT CIRCUIT ANALYSIS

The equivalent input circuit is shown below:
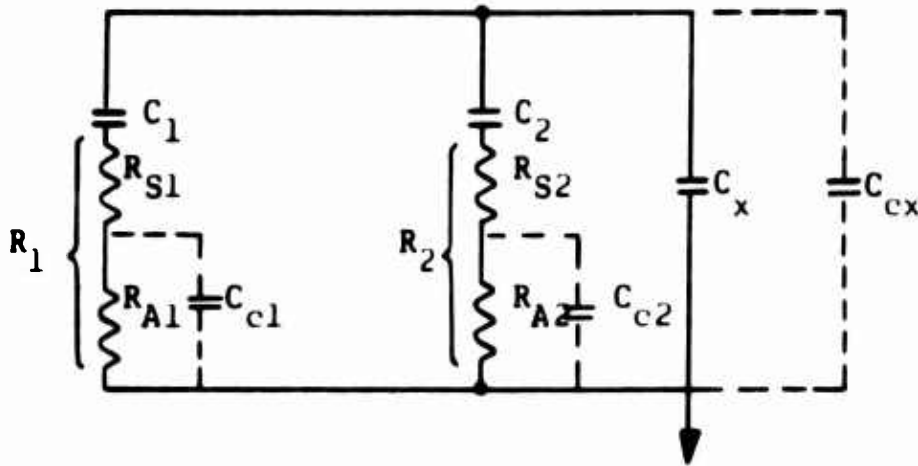
The detectors are represented by their respective capacitances C_1 and C_2, and the series resistances R_{S1} and R_{S2}. The charge amplifier input impedance is represented by C_x, with its cable capacitance C_{cx}.

In the following analysis, currents and charge that contribute to the various amplifier inputs will be calculated, when a charge Q_o is deposited on the first detector, i.e., C_1 at time t = o. Because of the symmetry of the circuit, the contribution at any circuit element of a simultaneous charge deposited on C_2 may be found by direct superposition.

Since R_{A1} and R_{A2} are small, i.e., approximately 50 ohms, the cable capacitance C_{c1} and C_{c2} may be ignored in the analysis. The cable capacitance C_{cx} will also be ignored since $C_{cx} \ll C_x$.

The initial condition of no currents flowing in a circuit with zero charge on all capacitors is assumed, except a charge Q_o deposited on C_1 at time t = 0, the quantities of interest are found by the conventional applications of Kirchoff's law. The results are listed below,

Where $\quad \Sigma C = C_1 + C_2 + C_x \quad \alpha_1 = \dfrac{\Sigma C}{R_1 C_1 (C_2 + C_x)} \quad \beta_1 = \dfrac{C_2 + C_x}{R_2 C_2 C_x}$ $\qquad$ (A.1)

Charge on C_1:

$$q_1(t) = Q_o \left[\frac{C_2}{\Sigma C} + \frac{C_2 + C_x}{\Sigma C} e^{-\alpha_1 t} \right]$$ $\qquad$ (A.2)

Charge on C_2:

$$q_2(t) = Q_0 \frac{C_2}{\Sigma C} \left[1 - \left(\frac{\beta_1 e^{-\alpha_1 t} - \alpha_1 e^{-\beta_1 t}}{\beta_1 - \alpha_1} \right) \right] \qquad (A.3)$$

Charge on C_x:

$$q_x(t) = Q_0 \frac{C_x}{\Sigma C} \left[\left(1 - \frac{(C_2 + C_x)}{C_x} e^{-\alpha_1 t} \right) + \left(\frac{C_2}{C_x} \right) \left(\frac{\beta_1 e^{-\alpha_1 t} - \alpha_1 e^{-\beta_1 t}}{\beta_1 - \alpha_1} \right) \right] \qquad (A.4)$$

Current through R_{A1}:

$$i_1(t) = \frac{Q_0}{R_1 C_1} e^{-\alpha_1 t} = \frac{\alpha_1 Q_0 (C_2 + C_x)}{\Sigma C} e^{-\alpha_1 t} \qquad (A.5)$$

Current through R_{A2}:

$$i_2(t) = \frac{Q_0}{R_1 C_1 R_2 C_x} \left(\frac{e^{-\beta_1 t} - e^{-\alpha_1 t}}{\alpha_1 - \beta_1} \right) \qquad (A.6)$$

If two charges Q_1 and Q_2 are deposited on detectors 1 and 2 simultaneously, the quantities of interest may be found immediately from the above equations by superposition. By use of the terms

$$\alpha_2 = \frac{C}{R_2 C_2 (C_1 + C_x)} \quad \text{and} \quad \beta_2 = \frac{C_1 + C_x}{R_1 C_1 C_x} \;, \qquad (A.7)$$

one obtains

$$q_x(t) = (Q_1 + Q_2) \frac{C_x}{\Sigma C} - (Q_1 e^{-\alpha_1 t} + Q_2 e^{-\alpha_2 t}) \qquad (A.8)$$

$$+ \text{ (small transient terms) },$$

$$i_1(t) = \frac{Q_1}{R_1 C_1} e^{-\alpha_1 t} - \frac{Q_2}{R_2 C_2 R_1 C_x} \left(\frac{e^{-\beta_2 t} - e^{-\alpha_2 t}}{\alpha_2 - \beta_2} \right) , \qquad (A.9)$$

$$i_2(t) = \frac{Q_2}{R_2 C_2} e^{-\alpha_2 t} - \frac{Q_1}{R_1 C_1 R_2 C_x} \left(\frac{e^{-\beta_1 t} - e^{-\alpha_1 t}}{\alpha_1 - \beta_1} \right) . \qquad (A.10)$$

Equation (A.8) shows that the total charge deposited on C_x, after a time which is long compared to the time constants $R_1 C_1$ and $R_2 C_2$, is

proportional to the sum of the two input charges Q_1 and Q_2. The fractional loss is

$$1 - \frac{C_x}{C} = \frac{C_1 + C_2}{C_1 + C_2 + C_x} \quad . \tag{A.11}$$

This is small, since $C_x >> C_1$ and C_2. Equations (A.9) and (A.10) show the currents i_1 and i_2 as seen by the coincidence amplifier to be proportional to the respective charge inputs, minus loading terms proportional to the charge in the adjacent input circuits. A comparison between the contributions of the two terms may be made by considering Equation (A.9). If the inverse time constants β_2 and α_2 are approximately equal, one can let $\alpha_2 = \beta_2 + a$, where a is small. The loading term in (A.9) becomes

$$\frac{Q_2}{R_2 C_2 R_1 C_x} e^{-\beta_2 t} \left(t - \frac{at^2}{2} + \cdots \right) \tag{A.12}$$

$$\cong \frac{Q_2}{R_2 C_2 R_1 C_x} \, t e^{-\beta_2 t} \quad .$$

This expression is zero at $t = 0$, and rises to a maximum of $\approx \frac{Q_2}{R_1 C_x} e^{-1}$ at $t = \frac{1}{\beta}$, as compared to the first term $\approx \frac{Q_2}{R_1 C_1} e^{-1}$ at the same time. Since $C_x >> C_1$, the loading term will be less than the proportional term by a factor $\approx \frac{C_1}{C_x}$ that may typically be $\frac{1}{100}$.

APPENDIX B

CHARGE LOOP CIRCUIT ANALYSIS

The charge amplifier consists of a high gain amplifier with capacitance feedback such that the output is proportional to the input charge.

The open loop gain of the amplifier is calculated by referring to the following equivalent circuit:
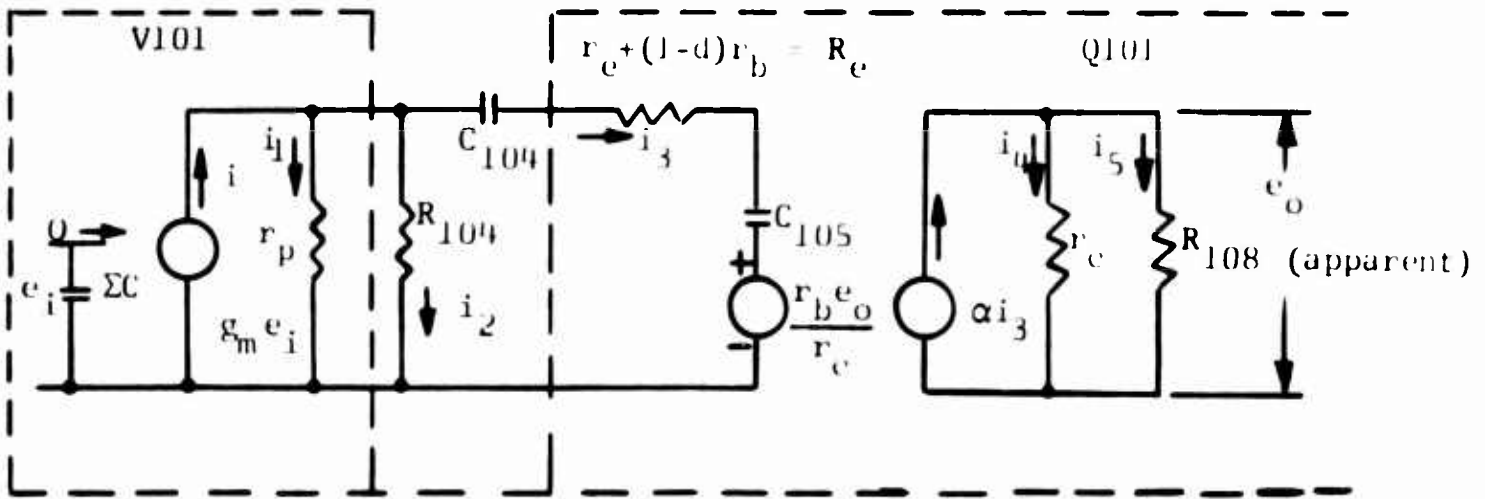
Since $r_c \gg r_b$, the output feedback generator $\frac{r_b}{r_c} e_o$ will be neglected. From the equivalent circuit, one has the following relationships:

$$e_1 = \frac{Q}{\Sigma C} \qquad (B.1)$$

$$i = g_m e_i \qquad (B.2)$$

$$R_1 = \frac{r_p R_{104}}{r_p + R_{104}} \qquad (B.3)$$

$$i_3 = i \frac{R_1}{R_1 + (R_e + \frac{1}{j\omega C_{104}} + \frac{1}{j\omega C_{105}})} \qquad (B.4)$$

$$e_o = \alpha i_3 \frac{(r_c)(R_{108})}{R_{108} + r_c} \qquad (B.5)$$

The open loop gain, A, is found by combining Equations (B.2), (B.4), and (B.5) to obtain

$$A = \frac{e_o}{e_i} = \alpha g_m R_{108} \left(\frac{r_c}{r_c + R_{108}} \right) \qquad (B.6)$$

$$x \; \frac{R_1 \, (C_{104}C_{105}) \, j\omega}{(R_1 + R_e) \, (C_{104}C_{105}) \left[j\omega + \frac{C_{104} + C_{105}}{(R_1 + R_e) \, (C_{104}C_{105})} \right]}$$

$$= \alpha \, g_m R_{108} \left[\frac{r_c}{r_c + R_{108}} \right] \left[\frac{R_1}{R_1 + R_e} \right] \left[\frac{1}{1 - \frac{j\beta}{\omega}} \right] ,$$

where $\beta = \dfrac{C_{104} + C_{105}}{(C_{104}) \, (C_{105}) \, (R_1 + R_e)}$, $\qquad (B.6a)$

and $R_1 \gg R_c$.

$$\therefore \; \frac{e_o}{e_i} \, (\text{mid-band}) = \alpha \, g_m \left[R_{108}(\text{apparent}) \right] \frac{r_c}{r_c + R_{108}(\text{apparent})}$$
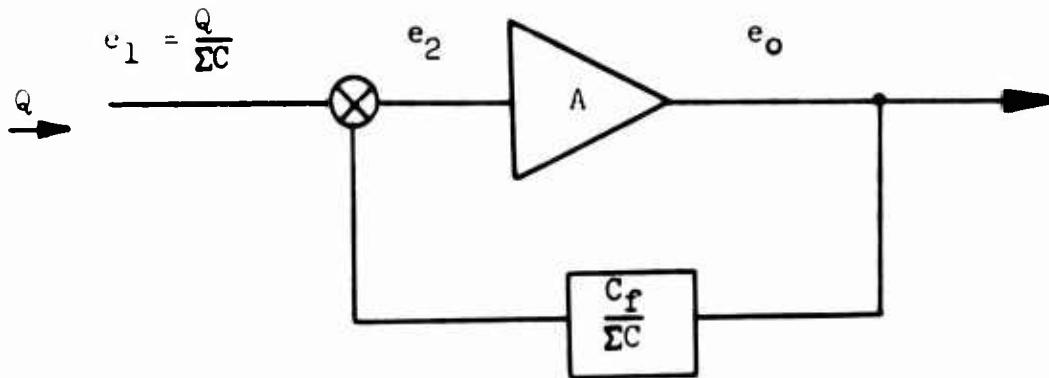
$$= 1330 \text{ for } \alpha = .95, \quad G_m = 5000 \; \mu\text{mhos}, \qquad (B.6b)$$

$$r_c = 10^6 \text{ ohms}, \quad R_{108} = 390K.$$

The dc stability of Q_{101} and Q_{102} is assured by stability factors of less than

$$2 \; \left(S = 1 + \frac{R_{base}}{R_{emitter}} \right) .$$

The closed loop gain of the charge loop may be approximated as shown below:

where A = Open loop gain,

C_f = Feedback capacitance (C_{108}),

ΣC = Total cold input capacitance seen by the input grid.

At the summing point one has

$$e_2 = e_i - e_o \frac{C_f}{\Sigma C} = e_i - e_2 A \frac{C_f}{\Sigma C} \quad , \tag{B.7}$$

from which

$$e_2 = \frac{e_i}{1 + \frac{AC}{\Sigma C} f} \tag{B.8}$$

and

$$e_o = Ae_2 = \frac{e_i}{\frac{1}{A} + \frac{C_f}{\Sigma C}} = \frac{Q}{\frac{\Sigma C}{A} = C_f} = \frac{Q}{C_f} \quad , \tag{B.9}$$

where $A \gg \dfrac{\Sigma C}{C_f}$.

The closed loop gain is

$$\frac{e_o}{e_i} = \frac{\Sigma C}{\frac{\Sigma C}{A} + C_f} = \frac{\Sigma C}{C_f} \quad , \tag{B.10}$$

where $A \gg \dfrac{\Sigma C}{C_f}$.

Equations (B.10) and (B.11) show that for high open loop gain, the voltage gain of the charge loop amplifier is proportional to the input capacitance ΣC. However, the output voltage is proportional to the charge deposited on the input but independent of the input capacitance.

APPENDIX C

THE COINCIDENCE PREAMPLIFIER

The coincidence preamplifier is made up of a common base input stage, four common emitter gain stages, and an emitter follower output stage for impedance matching. These stages are considered separately in the following analysis.

The equivalent circuit for the common base section is shown below. The parallel resistance r_c is the collector resistance and the R_L and C_L are the parallel load impedances. In the present case $r_c^L \gg R_L$, $\frac{1}{j\omega C_L}$.
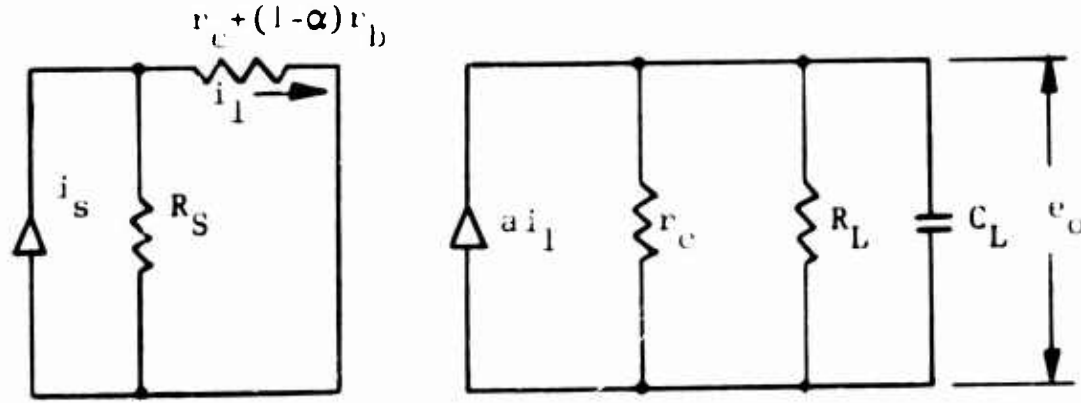
The input current from Equation (A.5) is

$$i_1 = \frac{Q_0}{\alpha} e^{-\alpha t} , \tag{C.1}$$

where $a = \frac{1}{C_d R_d}$ is the inverse time constant of the detector and amplifier input resistance. The current transferred to the collector in the common base arrangement is

$$a i_1 = a \frac{Q_0}{\alpha} e^{-\alpha t} , \tag{C.2}$$

From which the output voltage is found to be

$$e_0 = \frac{Q_0}{C_L} \left(\frac{R_L C_L}{R_L C_L - R_d C_D} \right) \left(e^{-t/R_L C_L} - e^{-t/R_d C_d} \right) . \tag{C.3}$$

The two exponentials in this expression correspond to the input time constant and the time constant of the common base load. The amplifier rise and delay time is ultimately limited by these terms.

The expression for voltage gain for a common emitter stage is given below, if it is assumed the input signal is not affected by either a series resistance or shunting capacitance, $\underline{i.e.}$,

$$\frac{1}{C'\omega} \gg Z + Z_1 \gg R_S.$$

$$\frac{e_o}{e_1} = \cfrac{R_L}{r_e + R_e(1 + 1/\beta)\left[\cfrac{R_e C'_{be} r'_{be} S}{r_e + R_e(1 + 1/\beta)}\right] + 1} \tag{C.4}$$

and

$$\frac{e_o}{e_i} \text{ (mid-band)} = \frac{R_L}{r_e + R_e(1 + 1/\beta)} , \tag{C.4a}$$

and

$$\omega_{3db} = \omega_\alpha \frac{r_e + R_e(1 + 1/\beta)}{R_e \beta} \tag{C.4b}$$

By use of values R_S = 1.2 K, β = 100, ω_α = 125 Mc, r_e = 50 ohms, R_e = 75 ohms, R_L = 1.2 K, the gain is found to be 9.4 and the 3 db frequency is f3db $\approx$ 2 Mc.

The four common emitters in cascode produce a 3db gain of approximately 2000. With a common base input of 0.2 mV/MeV, the amplifier output is 0.4 V/MeV. The experimentally determined gain is in agreement with this value. By adjusting the emitter resistor in the final gain stage, this over-all gain may be reduced by a factor of 4.

A complete discussion of this type of circuit is given in Reference 12.

113

DOCUMENT CONTROL DATA - R&D

(Security classification of title, body of abstract and indexing annotation must be entered when the overall report is classified)

1. ORIGINATING ACTIVITY (Corporate author)	2a. REPORT SECURITY CLASSIFICATION
US Army Nuclear Defense Laboratory Edgewood Arsenal, Maryland	UNCLASSIFIED
	2b. GROUP

3. REPORT TITLE

NEUTRON DETECTION AND SPECTROSCOPY WITH SEMICONDUCTOR DETECTORS

4. DESCRIPTIVE NOTES *(Type of report and inclusive dates)*
Final Report - Prepared by Solid State Radiations, Inc., for
US Army Nuclear Defense Laboratory

5. AUTHOR(S) *(Last name, first name, initial)*

Zatzick, M. R.
Zimmerman, E. L.

6. REPORT DATE	7a. TOTAL NO. OF PAGES	7b. NO. OF REFS
April 1965 (Date of Revision)	121	12

8a. CONTRACT OR GRANT NO.	9a. ORIGINATOR'S REPORT NUMBER(S)
DA18-108-405-Cml-1012	NDL-TR-54
b. PROJECT NO.	
c.	9b. OTHER REPORT NO(S) (Any other numbers that may be assigned this report) None
d.	

10. AVAILABILITY/LIMITATION NOTICES

Qualified requesters may obtain copies of this report from Defense Documentation Center, Cameron Station Alexandria, Virginia 22314

11. SUPPLEMENTARY NOTES	12. SPONSORING MILITARY ACTIVITY
	Defense Atomic Support Agency

13. ABSTRACT

Results are presented of a study of methods for utilizing diffused junction, semiconductor detectors in neutron detection and spectroscopy. The study resulted in the development of various neutron-sensitive coated detectors and the Li^6 epithermal neutron spectrometer system, which consists of a Li^6-sandwich detector and a complete, integrated electronic system. The techniques investigated for applying neutron-sensitive materials to detector surfaces included solution evaporation, vacuum evaporation, and electrodeposition. Solution evaporation is preferable when a thick coating of B^{10} or U^{235} is desired for maximum sensitivity. Vacuum exaporation is preferable when very thin uniform films of Li^6 and Li^6F are required on the detector surface. A thermal neutron source was used to observe the response of each coating material deposited on the detectors as a function of dead layer and radiator thickness. Theoretical relationships depending on range-energy relationships were derived; these results adequately predict the response of coated detectors as a function of converter material thickness, detector dead layer, and discriminator settings. The detector developed under this program for the epithermal neutron spectrometer system consists of a layer of Li^6F sandwiched between two silicon detectors in a hermetically sealed package.

DD FORM 1 JAN 64 **1473**